TECHNISCHE UNIVERSITÄT WIEN

Diplomarbeit

Numerical Analysis of Fluid Flow and Heat Transfer Characteristics of Ejectors and Vortex Tubes

ausgeführt zum Zwecke der Erlangung des akademischen Grades eines Diplom-Ingenieurs (Dipl.-Ing oder DI) eingereicht an der TU Wien, Fakultät für Maschinenwesen und Betriebswissenschaften, von

Constantin ZENZ

Matr.Nr.: 01227264

Neukräftengasse 29, 1130 Wien

unter der Leitung von

Privatdoz. Dipl.-Ing. Dr.techn. Christoph Reichl
Institut für Strömungmechanik und Wärmeübertragung, E322

und

Dipl.-Ing. Dr.techn. Mirza Popovac
Austrian Institute of Technology GmbH

Wien, Mai 2020

Ich nehme zur Kentniss, dass ich zur Drucklegung dieser Arbeit nur mit Bewilligung der Prüfungskommision berechtigt bin.

Eidesstattliche Erklärung

Ich erkläre an Eides statt, dass die vorliegende Arbeit nach den anerkannten Grundsätzen für wissenschaftliche Abhandlungen von mir selbstständig erstellt wurde. Alle verwendeten Hilfsmittel, insbesondere die zugrunde gelegte Literatur, sind in dieser Arbeit genannt und aufgelistet. Die aus den Quellen wörtlich entnommenen Stellen, sind als solche kenntlich gemacht.
Das Thema dieser Arbeit wurde von mir bisher weder im In- noch Ausland einer Beurteilerin/einem Beurteiler zur Begutachtung in irgendeiner Form als Prüfungsarbeit vorgelegt. Diese Arbeit stimmt mit der von den Begutachterinnen/Begutachtern beurteilten Arbeit überein.

....
Stadt und Datum   Unterschrift

Acknowledgements

First and foremost I would like to thank Dr. Christoph Reichl and Dr. Mirza Popovac, for giving me the opportunity to work on this interesting, highly relevant and challenging topic. They helped me with all sorts of problems and questions that arose and always found the time to provide much appreciated guidance and advice throughout my time at AIT.

Furthermore, I want to thank Dr. Klemens Marx and Dr. Michael Lauermann for their support within the VWE project and many interesting as well as fun discussions.

I want to thank Dr. Thomas Loimer for generously sharing with me his knowledge on supersonic two-phase flows. Also, I would like to thank Dr. Reinhard Willinger for an interesting discussion on diffuser design and analogies between ejectors and turbomachinery.

I would like to thank all my wonderful colleagues at AIT for making my time there a great experience. I especially want to say thank you to all the fellow master thesis students, interns and PhD students for all the interesting discussions and lots of fun.

Finally, I want to thank my parents for always supporting me and providing me the possibility to pursue these studies. Also, I want to thank my family and friends for all their support throughout my studies.

Lastly I want to thank Lena for always being there for me.

Contents

Abstract

Decarbonization of industrial processes is a great obstacle yet to overcome. One step towards a sustainable and low-emission future can be achieved by using heat pumps to provide heat for industrial processes. As heat pumps for such high temperature applications feature a large difference in condenser and evaporator pressure, the losses due to irreversible dissipation within the expansion process are high. To make high-temperature heat pumps more efficient and therefore interesting for industrial applications, two alternative expansion devices to replace the conventional throttle valve are investigated: the vortex tube and the ejector. Both devices are investigated numerically within this work to gain better understanding of the underlying fluid flow phenomena, their applicability to heat pump cycles and to give an outlook on possible cycle efficiency improvements.

For the vortex tube, it is found that in order to make use of its capability of separating a fluid into a high- and low-temperature stream, which is only working when operated with a gas, a fundamentally different heat pump design is necessary. From systematic simulations, using different geometries, refrigerants and operating conditions, it is concluded that a very high pressure lift is necessary in the heat pump cycle in order to significantly improve the cycle's coefficient of performance. One promising case is found, where the coefficient of performance is improved by 19% over a standard heat pump.

To efficiently simulate the flow field inside an ejector, the two-phase flow is modeled as being in a homogeneous equilibrium state. Based on this assumption, a model is developed and integrated in a commercial Computational Fluid Dynamics code to allow for fast computations without the need for experimental-based fine-tuning as opposed to a full multiphase model. The model is then used to simulate an ejector which is working within a high temperature heat pump operated with butane. The main flow features are analysed and phenomena occurring at unfavourable operating points, obtained through an unsuitable geometry, are identified.

Kurzfassung

Auf dem Weg in eine nachhaltige und emissionsarme Zukunft stellt besonders die Dekarbonisierung der Industrie eine besondere Herausforderung dar. Ein großer Beitrag zur Reduktion von Treibhausgasemissionen und zu mehr Ressourcenschonung kann durch den Einsatz von Hochtemperatur-Wärmepumpen zur Wärmebereitstellung für Industrieprozesse erzielt werden. Die dabei üblicherweise auftretenden hohen Temperaturdifferenzen zwischen Wärmequelle und -senke führen zu großen Druckdifferenzen zwischen Verdampfer und Kondensator und in Folge zu großen Drosselverlusten im Expansionsprozess, der herkömmlicherweise in einem isenthalpen Drosselventil stattfindet. Um ein gewisses Maß an Energie aus dem Expansionsprozess zurückzugewinnen werden in dieser Arbeit zwei alternative Entspannungsvorrichtungen im Hinblick auf eine potentielle Effizienzsteigerung von Wärmepumpen numerisch untersucht: das Wirbelrohr und der Ejektor.

Im Bezug auf das Wirbelrohr wird hier festgestellt, dass der in Wirbelrohren angestrebte Effekt der Temperaturseparation nur für vollständig gasförmige Fluide nutzbar ist und daher ein grundlegend abweichender Wärmepumpenkreislauf notwendig ist. Der Effekt ist bei den hier untersuchten Kältemitteln deutlich geringer als zum Beispiel bei Luft. Verschiedene Kältemittel, Geometrien und Betriebsbedingungen werden untersucht, mit dem Ergebnis, dass eine hohe Druckdifferenz notwendig ist, um die Effizienz der Wärmepumpe gegenüber einer Standardwärmepumpe zu erhöhen. Ein vielversprechender Anwendungsfall, in dem der Einsatz eines Wirbelrohrs die Leistungszahl um 19% erhöht, wird vorgestellt.

Um die Strömungsvorgänge in einem Zweiphasen- Ejektor effizient und ohne die Notwendigkeit der Verfügbarkeit detaillierter experimenteller Daten zu simulieren, wird die Strömung als homogen und im mechanischen und thermodynamischen Gleichgewicht befindlich modelliert. Mithilfe dieses Modells wird ein Ejektor simuliert, der mit Butan in einer Hochtemperaturwärmepumpe betrieben wird. Die Ergebnisse von Simulation und Experiment werden gegenübergestellt. Überdies werden Strömungsphänomene untersucht, die bei unerwünschten Betriebspunkten, beispielsweise durch eine für die herrschenden Bedingungen ungeeignete Ejektorgeometrie, auftreten können. Das hier entwickelte Modell kann früh im Entwicklungsprozess verwendet werden, um eine geometrische Vorauslegung durchzuführen.

List of Figures

v

List of Tables

Nomenclature

Latin symbols	
A	surface area
Br	Brinkmann number
c	speed of sound
c_p	specific heat capacity at constant pressure
c_v	specific heat capacity at constant volume
d	diameter
D	diameter
E	total energy
F	force
g	gravitational acceleration
h	height; specific enthalpy
H	enthalpy
l	length
L	length
$\dot{m}$	mass flow rate
M	molar mass
Ma	Mach number
k	turbulent kinetic energy
p	pressure
P^k	production of turbulent kinetic energy
Pe	Péclet number
q	conductive heat flux
Q	heat
r	radius
R	gas constant; radius
Re	Reynolds number
s	strain rate
S	source term in a transport equation; surface
t	time
T	temperature; time
u, v, w	velocity vector components in Cartesian coordinates
v	velocity
V	volume
w	weighting factor; width
x, y, z	direction vector components in Cartesian coordinates

Greek symbols	
α	heat transfer coefficient; under-relaxation factor; volume fraction
δ	boundary layer thickness
δ_{ij}	Kronecker delta
η	entrainment ratio
ε	dissipation
γ	cold fraction

Γ	diffusion coefficient
κ	heat capacity ratio; von Kárman constant
λ	eigenvalue; thermal conductivity
μ	dynamic viscosity
ν	kinematic viscosity
Π_S	suction pressure ratio
Π_T	temperature ratio
ρ	density
σ	Prandtl number
τ	stress
Φ	viscous dissipation
χ	vapor quality (vapor mass fraction)
ω	specific dissipation

Subscripts

c	cell; cold
eff	effective
f	face
h	hot
i, j, k	indices of tensor notation denoting Cartesian coordinate directions
in	inlet
int	intermediate
nb	neighbour
o	outlet
$prim$	primary
sec	secondary
s	static
t	total; turbulent
∞	free stream

Abbreviations

CAM	constant area mixing
cf.	conferatur (compare)
CFD	computational fluid dynamics
CFL	Courant number
COP	coefficient of performance
CPM	constant pressure mixing
CS	control surface
CV	control volume
DNS	direct numerical simulation
e.g.	example given
Eq.	equation
HEM	homogeneous equilibrium model
i.e.	id est (that is)
RANS	Reynolds averaged Navier-Stokes
UDF	user-defined function (Ansys Fluent terminology)

UDS	user-defined scalar (Ansys Fluent terminology)

Diacritical signs	
$\dot{x}$	derivative of x with respect to time
$\widetilde{x}$	Favre average of x
$\overline{x}$	Reynolds average of x
x'	fluctuating component of x with respect to Reynolds-averaging
x''	fluctuating component of x with respect to Favre-averaging
$\vec{x}$	x is a vector
$\underline{X}$	X is a matrix

1 Introduction

Decarbonization of industrial processes is one of the main obstacles yet to overcome on the way towards a sustainable, low-emission future. It is an important step on the way to reach goals such as that of the Paris Agreement to limit global warming to 2°C above pre-industrial levels within this century[1] or the EU 2030 goals, which aim at increasing energy efficiency by 32.5% by 2030[2]. In Austria, the goods producing industry accounts for 29.9% of energy consumption[3]. More than 80% of demand for heat in the industrial sector regards process heat at more than 100°C[4]. According to Hartl et al.[5], industrial heat pumps for high temperature applications play a central role in a sustainable energy future. Especially heat pumps for applications at up to 155°C are relevant for industrial processes such as steam generation, where previously not used waste heat can be reused[5]. Steam generation accounts for 28.9% of usable energy in industrial applications in Austria. The highest demand for energy for steam generation is found in the paper industry, accounting for 74.9% of usable energy. At the moment, this energy is mostly provided by natural gas and, to a small extent, biogenous fuel[6]. Using high temperature heat pumps as means of heat source for industrial steam generation can, in combination with an increasing share of electric energy from renewable sources in the grid, act as a major step in the process of decarbonizing the industry. In Germany, the demand for heat at up to 140°C is estimated to be around 611 PJ[4]. Currently, efficient heat pumps are available for domestic heating application, where they are nowadays considered a standard solution[4]. The development of efficient high temperature heat pumps is however still an ongoing research topic of great importance. High temperature applications come with a high condenser pressure and thus great losses in the expansion process which usually takes place in an isenthalpic throttle valve. A schematic heat pump cycle can be seen in Figure 1.1. From state **1** to **2**, the evaporated or superheated refrigerant is lifted to a higher pressure level inside a compressor. From state **2** to **3**, heat is transferred to the consumer, e.g. to provide heat for steam generation. At state **3**, the refrigerant is partly or fully condensed or subcooled. From state **3** to **4**, the refrigerant is expanded to the lower pressure level in an isenthalpic throttle valve. From state **4** to **1**, the refrigerant is evaporated via heat transfer from a heat source, e.g. waste heat from industrial processes.

To improve the overall coefficient of performance (COP) of such heat pump cycles, two alternative components for the expansion process (**3** to **4**) are investigated, with the aim of recuperating some of that expansion energy: the vortex tube and the ejector. A vortex tube is capable of separating a high-pressure fluid into a hot and a cold stream, where the cold and hot streams' temperatures lie below and above the inlet temperature, respectively. Those streams can then be used, e.g. for further superheating or subcooling of the refrigerant, thus improving the cycle's efficiency by using the kinetic energy of the high-pressure fluid for establishing a temperature gradient. An ejector is capable of using the kinetic energy of a high-pressure fluid to lift the pressure level of a low pressure fluid by entraining it, thus lifting the lower pressure level inside the heat pump and decreasing compressor work.

Both vortex tubes and ejectors have been investigated extensively and used in a variety of industrial applications, but knowledge of their use in heat pump applications, when being operated with working fluids and within ranges of pressure and temperature that are typical for heat pump applications, is very limited. In order to evaluate the potential of the integration of a vortex tube or ejector in a heat pump, the fluid flow and heat transfer processes occurring inside the devices are modeled and simulated by the means of computational fluid dynamics (CFD). In this way, influences of different geometries, working fluids and operating conditions can be analyzed at a very early stage
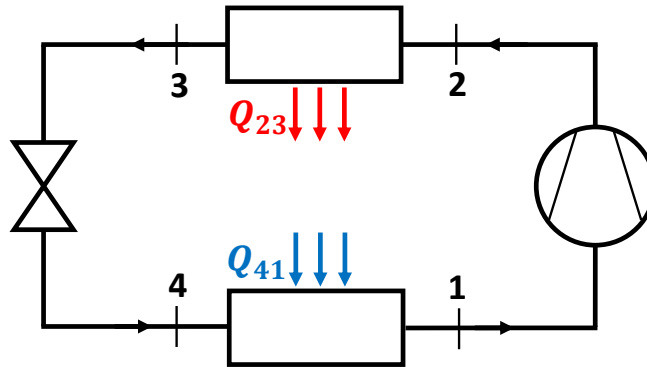
Figure 1.1: Schematic layout of a conventional heat pump cycle

in the development process, without the need for expensive experimental setups. The thus obtained simulation results can then be used to model an entire heat pump in a one-dimensional (when also modeling transient effects) or zero-dimensional (for a steady state) analysis to investigate potential COP improvements. The purpose of this methodology is to provide a cheap and quick (compared to experimental investigations) way of identifying promising heat pump configurations that can then be evaluated in more detail through experimental work. Another advantage of numerical investigations is that all flow quantities can be obtained - presumed that the numerical investigation is accurate and features all necessary physical phenomena - at any desired location in the apparatus, whereas experimental investigations are in practice often very difficult. Considering the inner diameters of typical vortex tubes and ejectors often measure only a few millimeters, it is almost impossible to measure quantities such as dynamic pressure or velocity without interfering with the flow itself.

Concerning the structure of this work, in chapter 2, the mathematical models used to describe the underlying physical processes of the fluid flow inside vortex tubes and ejectors are presented. Case-specific models relevant only for either the vortex tube or the ejector are introduced in the respective chapters. Chapter 3 provides a brief overview of the numerical schemes used to solve the equations discussed in chapter 2. After this general introduction to CFD, chapters 4 and 5 focus on the modeling and analysis of the vortex tube and the ejector, respectively. Each chapter gives first an overview of the respective device and specific mathematical models, numerical schemes and solution strategies are elaborated. Then, the results of the CFD simulations are presented and discussed. Both chapter 4 and 5 close with a chapter-specific conclusion. In chapter 6, an overall conclusion of the investigations presented in this work is provided.

2 Mathematical Modeling

In this chapter, a general overview of the typical mathematical models used to simulate fluid mechanics problems is provided. Problem-specific topics that are only applicable for either the flow physics inside a vortex tube or an ejector are discussed in the respective chapters 4.2 and 5.2. This chapter is based on references [7–13], if not mentioned otherwise.

When indices (e.g. i) are used, these denote Cartesian coordinate directions and imply tensor notation with Einstein summation convention. This means that terms in which one index occurs twice - e.g. the index i in Eq. (2.1) - are summed over this index.

2.1 Conservation Equations

The underlying fluid mechanics are described by the continuity equation and the Navier-Stokes equation, which represent the physical meaning of conservation of mass and momentum, respectively. The continuity equation reads

$$\frac{\partial \rho}{\partial t} + \frac{\partial (\rho v_i)}{\partial x_i} = S_m \tag{2.1}$$

The source term S_m denotes any mass added. When there is no mass source present, $S_m = 0$. Therefore Eq. (2.1) simplifies to

$$\frac{\partial \rho}{\partial t} + \frac{\partial (\rho v_i)}{\partial x_i} = 0 \tag{2.2}$$

The momentum equation, i.e. the Navier-Stokes equation, reads

$$\frac{\partial (\rho v_i)}{\partial t} + \frac{\partial (\rho v_i v_j)}{\partial x_j} = -\frac{\partial p}{\partial x_i} + \frac{\partial \tau_{ij}}{\partial x_j} + \rho g_i + F_i \tag{2.3}$$

where F_i denotes any external body forces other than gravity. As there are no significant body forces occurring, this term is omitted. Also, as gravitational influence is believed to play a minor role and it is not obvious in which orientation the vortex tube or ejector would be operated, the gravity term is omitted, yielding

$$\frac{\partial (\rho v_i)}{\partial t} + \frac{\partial (\rho v_i v_j)}{\partial x_j} = -\frac{\partial p}{\partial x_i} + \frac{\partial \tau_{ij}}{\partial x_j} \tag{2.4}$$

The viscous stress tensor τ_{ij} reads

$$\tau_{ij} = \mu \left(\frac{\partial v_i}{\partial x_j} + \frac{\partial v_j}{\partial x_i} \right) - \frac{2}{3} \mu \frac{\partial v_k}{\partial x_k} \delta_{ij} \tag{2.5}$$

where δ_{ij} is the Kronecker delta, defined as

$$\delta_{ij} = \begin{cases} 1 & \text{if} \quad i = j \\ 0 & \text{if} \quad i \neq j \end{cases} \tag{2.6}$$

As changes in temperature and the transport of energy are of interest, an equation for the conservation of energy, E, is added to the set of underlying equations. The energy equation, formulated as an equation for conservation of total energy, E, defined as

$$E = h - \frac{p}{\rho} + \frac{v^2}{2} \tag{2.7}$$

3

reads

$$\frac{\partial(\rho E)}{\partial t} + \frac{\partial(v_j(\rho E + p))}{\partial x_j} = \frac{\partial}{\partial x_j}\left(\tau_{ij}v_i + \lambda\frac{\partial T}{\partial x_j}\right) + S_h \tag{2.8}$$

where S_h denotes any sources of heat. The second term on the left-hand side represents convective heat transfer, the left and right term in the bracket on the right-hand side denote viscous dissipation and conductive heat transfer, respectively. Viscous dissipation is often neglected as its effect is insignificant in many cases, but has to be evaluated separately for each problem. In Eq. (2.8), Fourier's law is used to model the conductive heat flux q_i as

$$q_i = -\lambda\frac{\partial T}{\partial x_i} \tag{2.9}$$

In the above equations, T denotes the static temperature. Analogous to pressure, the total (or stagnation) temperature, T_t, is the sum of static and dynamic temperature, and therefore the temperature which is obtained if a fluid is decelerated to zero velocity. Therefore

$$T_t = T + \frac{v^2}{2c_p} \tag{2.10}$$

where c_p is the specific heat capacity at constant pressure.

The above set of 5 equations, consisting of the continuity equation, Eq. (2.2), the three-dimensional Navier-Stokes equation, Eq. (2.4) and the energy equation, Eq. (2.8), fully describes the physics of a single-phase flow problem. In the case of incompressible flow, the equations can be further simplified, while in the case of a compressible flow problem, a way to compute the non-constant density of the fluid must be introduced, e.g. through the ideal gas law. In theory, a solution for this set of equations could be obtained numerically, but in practice solving these equations using direct numerical simulation (DNS) is computationally not affordable as it requires very fine spatial and temporal resolution. This is due to the chaotic behaviour of these strongly coupled, nonlinear, partial differential equations known as turbulence. The vast majority of flows encountered in every day life and engineering problems is turbulent. Although no strict definition of turbulence exists, some characteristics of turbulent flows can be identified[9]:

- Turbulent flows are irregular and chaotic, but they are not stochastic as they are deterministically described by the Navier-Stokes equations.

- Turbulent flows feature a variety of so-called eddy sizes, distributed from the largest geometric features of the flow down to the smallest sizes where kinetic energy is dissipated into heat.

- Diffusivity increases in turbulent flows compared to laminar ones, increasing momentum exchange.

- Turbulence occurs at high Reynolds numbers, e.g. the transition to turbulence in a pipe flow occurs at Re $\approx$ 2300.

- Turbulent flow is always three-dimensional.

- Kinetic energy is transferred from the mean flow to the smallest turbulent structures (eddies), where it is dissipated into heat. This process is called the cascade process. Therefore, a turbulent flow must be provided with energy to stay turbulent.

4

For most engineering purposes only the mean values of a turbulent flow are of interest, and turbulent fluctuations that occur at stationary conditions (e.g. the operating point of a machine) do not need to be resolved. This allows for the solution of turbulent flow problems with reasonable investment in computing power through so-called turbulence modeling.

2.2 Turbulence Modeling

As a stationary (or quasi-stationary) solution is assumed to exist, only the mean values of the flow field are of interest and the equations are time-averaged, making solving this set of equations (continuity, Navier-Stokes and energy equation) computationally affordable. This process is first shown for the simplification of an incompressible flow, with the equations and averaging method being adapted in a later step to account for compressibility. The idea of turbulence modeling is shown by the example of the well-established k-ε turbulence model. Other, problem-specific turbulence models are presented in the respective chapters.

The instantaneous variables of Eqs. (2.2), (2.4) and (2.8) are usually split into a mean and a fluctuating part using Reynolds decomposition:

$$\phi = \overline{\phi} + \phi' \tag{2.11}$$

where

$$\overline{\phi} = \frac{1}{2T} \int_{-T}^{T} \phi dt \tag{2.12}$$

After decomposing all time-dependent variables according to Eq. (2.11), the equations are time averaged according to Eq. (2.12). By definition

$$\overline{\overline{\phi}} = \overline{\phi} \tag{2.13}$$

$$\overline{\phi'} = 0 \tag{2.14}$$

and thus also

$$\overline{\overline{\psi}\phi'} = 0 \tag{2.15}$$

The only terms including fluctuations that turn out to be non-zero after time-averaging the equations are fluctuation correlation terms of the form

$$\overline{\phi'\psi'} \neq 0 \tag{2.16}$$

Using these identities and the fact that for incompressible flow ρ can be moved out of the partial derivatives and assuming a constant viscosity, μ, the well-known Reynolds Averaged Navier-Stokes (RANS) equations are obtained.

First, the continuity equation is simplified. The unsteady term (the derivative with respect to time) is omitted as steady flow is assumed. Then, the density is moved outside the spatial derivative as incompressible flow is assumed. By that, Eq. (2.2) takes the following form

$$\frac{\partial v_i}{\partial x_i} = 0 \tag{2.17}$$

Using the same simplifications (steady problem, incompressibility) and Eq. (2.17), the Navier-Stokes equations simplify to

$$\rho \frac{\partial v_i v_j}{\partial x_j} = -\frac{\partial p}{\partial x_i} + \mu \frac{\partial^2 v_i}{\partial x_j \partial x_j} \tag{2.18}$$

5

where the partial derivative of the viscous stress tensor reduces to a single term, as using Eq. (2.17) it turns out that

$$\mu \frac{\partial}{\partial x_j}\left(\frac{\partial v_j}{\partial x_i}\right) = \mu \frac{\partial}{\partial x_i}\left(\frac{\partial v_j}{\partial x_j}\right) = 0 \tag{2.19}$$

$$\frac{2}{3}\mu \frac{\partial v_k}{\partial x_k}\delta_{ij} = 0 \tag{2.20}$$

It shall be noted that Eq. (2.19) only holds for a constant viscosity. For constant density and non-constant viscosity, only Eq. (2.20) holds. Decomposing each variable using Eq. (2.11) and time-averaging Eqs. (2.17) and (2.18) yields

$$\frac{\partial \overline{(\overline{v}_i + v'_i)}}{\partial x_i} = 0 \tag{2.21}$$

$$\rho \frac{\partial \overline{(\overline{v}_i + v'_i)(\overline{v}_j + v'_j)}}{\partial x_j} = -\frac{\partial \overline{(\overline{p} + p')}}{\partial x_i} + \mu \frac{\partial^2 \overline{(\overline{v}_i + v'_i)}}{\partial x_j \partial x_j} \tag{2.22}$$

Using the above listed rules for time averaging, Eqs. (2.13)-(2.16), the RANS equations are obtained.

$$\frac{\partial \overline{v}_i}{\partial x_i} = 0 \tag{2.23}$$

$$\rho \frac{\partial \overline{v}_i \overline{v}_j}{\partial x_j} = -\frac{\partial \overline{p}}{\partial x_i} + \frac{\partial}{\partial x_j}\left(\mu \frac{\partial \overline{v}_i}{\partial x_j} - \rho \overline{v'_i v'_j}\right) \tag{2.24}$$

Eq. (2.24) now contains a new term, $-\rho \overline{v'_i v'_j}$, called the Reynolds stress tensor, that is containing the correlations of the velocity fluctuations. This is a symmetric tensor, therefore containing six independent variables that are generally unknown. Therefore, by performing Reynolds decomposition and time-averaging, six unknowns are added to the set of equations, yielding ten unknowns (i.e. pressure, three velocity components and six Reynolds stress components) but only four equations (i.e. the continuity equation and three components of the Navier-Stokes equation). This is called the closure problem, as the equations need to be closed in order to be solvable. It is of course possible to derive a transport equation for $\overline{v'_i v'_j}$ itself, but when deriving it, new triple correlation terms of the form $\overline{v'_i v'_j v'_k}$ turn up that introduce even more unknowns. Therefore, at some point a model has to be introduced, which is called turbulence modeling. The most common and straightforward approach is to introduce a so-called eddy viscosity or turbulent viscosity, μ_t, via the Boussinesq assumption. Now, a non-constant viscosity is assumed, as it will be clear that when introducing a turbulent viscosity, the assumption of a constant viscosity does not hold anymore. The Boussinesq assumption reads

$$\frac{\partial}{\partial x_j}\left[\mu\left(\frac{\partial \overline{v}_i}{\partial x_j} + \frac{\partial \overline{v}_j}{\partial x_i}\right) - \rho \overline{v'_i v'_j}\right] = \frac{\partial}{\partial x_j}\left[(\mu + \mu_t)\left(\frac{\partial \overline{v}_i}{\partial x_j} + \frac{\partial \overline{v}_j}{\partial x_i}\right)\right] \tag{2.25}$$

This leads to

$$\rho \overline{v'_i v'_j} = -\mu_t \left(\frac{\partial \overline{v}_i}{\partial x_j} + \frac{\partial \overline{v}_j}{\partial x_i}\right) \tag{2.26}$$

Because of the continuity equation, Eq. (2.26) turns to zero when performing a contraction, i.e. setting indices $i = j$. This is unphysical, as a contraction of $\overline{v'_i v'_j}$ should give twice the turbulent

6

kinetic energy, k, which is defined as

$$k = \frac{1}{2}\overline{v_i' v_i'} \tag{2.27}$$

Therefore Eq. (2.26) is slightly modified to

$$\rho\overline{v_i' v_j'} = -\mu_t \left(\frac{\partial \overline{v}_i}{\partial x_j} + \frac{\partial \overline{v}_j}{\partial x_i} \right) + \frac{2}{3}\delta_{ij}\rho k \tag{2.28}$$

The last term of Eq. (2.28) is now grouped with the pressure and the Navier-Stokes equation, using the Boussinesq assumption, finally reads

$$\rho\frac{\partial \overline{v}_i \overline{v}_j}{\partial x_j} = -\frac{\partial(\overline{p} + 2\rho k/3)}{\partial x_i} + \frac{\partial}{\partial x_j}\left[(\mu + \mu_t)\left(\frac{\partial \overline{v}_i}{\partial x_j} + \frac{\partial \overline{v}_j}{\partial x_i} \right)\right] \tag{2.29}$$

Like the molecular viscosity, $\mu_t = \rho\nu_t$. As can be seen, the Boussinesq assumption models the Reynolds stresses by assuming a gradient-diffusion mechanism, similar to that of the viscous stresses. This is a radical simplification, as a six-component variable is simply modeled through one (time- and location-dependent) scalar. This means turbulence is assumed to be isotropic, which in reality only holds for the smallest turbulent structures (eddies), where turbulent kinetic energy is dissipated into heat. This newly introduced quantity ν_t is not known and needs to be modeled. The dimension of ν_t, like that of ν, needs to be $[m^2/s]$. A simple way to model ν_t for wall-bounded flows is

$$\nu_t = l_{mix}^2 \left| \frac{\partial \overline{v}_1}{\partial x_2} \right| \tag{2.30}$$

This is called the mixing length model. In Eq. (2.30), x_2 is the wall-normal coordinate, v_1 is the velocity in wall-adjacent direction and l_{mix} is the mixing length, which serves as characteristic length scale. The biggest issue with this model is that l_{mix} is generally unknown. This type of model is called an algebraic model, as one algebraic equation needs to be solved additionally, or a zero equation model, as no additional transport equation needs to be solved. A more elaborate way to model ν_t is to introduce one or more additional transport equations to be solved. Such models are, depending on the number of additional transport equations, called one equation models, two equation models, and so on. The most commonly used two equation model is the k-ε model, where one transport equation for the turbulent kinetic energy, k, and one for its dissipation rate, ε, are solved. The turbulent viscosity is then computed in the following way.

$$\nu_t = C_\mu \frac{k^2}{\varepsilon} \tag{2.31}$$

C_μ is an empirically tuned constant that is set to $C_\mu = 0.09$. By using the definition of the turbulent kinetic energy, $2k = \overline{v_i' v_i'}$, an equation for k can be directly obtained, using the definition of k, either from the Navier-Stokes equations or from the transport equation for $\overline{v_i' v_j'}$, which can itself be derived from the Navier-Stokes equations.

$$\frac{\partial k}{\partial t} + \overline{v}_j \frac{\partial k}{\partial x_j} = \underbrace{-\overline{v_i' v_j'}\frac{\partial \overline{v}_i}{\partial x_j}}_{P^k} \underbrace{- \nu\overline{\frac{\partial v_i'}{\partial x_j}\frac{\partial v_i'}{\partial x_j}}}_{\varepsilon} \underbrace{- \frac{\partial}{\partial x_j}\left[\overline{v_j'\left(\frac{p'}{\rho} + \frac{1}{2}v_i' v_i' \right)}\right]}_{D_t^k} + \underbrace{\nu\frac{\partial^2 k}{\partial x_j \partial x_j}}_{D_\nu^k} \tag{2.32}$$

Eq. (2.32) is the exact k-equation, which is exact in the sense of being as exact as the Navier-Stokes equations themselves, as no simplification has yet been employed. On the right-hand side of Eq. (2.32) the terms are grouped according to their respective physical meanings: production, dissipation, turbulent diffusion and viscous diffusion. Apart from the viscous diffusion term, D_ν^k, all terms include unknown quantities and therefore require modeling. The Reynolds stresses in the production term, P^k, can be modeled with the Boussinesq assumption. The dissipation, ε, will be obtained from its own transport equation, which will be formulated in a later step. The turbulent diffusion term, D_t^k, is modeled assuming a gradient-diffusion mechanism. Hence, the modeled k-equation reads

$$\frac{\partial k}{\partial t} + \overline{v}_j \frac{\partial k}{\partial x_j} = \nu_t \left(\frac{\partial \overline{v}_i}{\partial x_j} + \frac{\partial \overline{v}_j}{\partial x_i} \right) \frac{\partial \overline{v}_i}{\partial x_j} - \varepsilon + \frac{\partial}{\partial x_j} \left[\left(\nu + \frac{\nu_t}{\sigma_k} \right) \frac{\partial k}{\partial x_j} \right] \tag{2.33}$$

σ_k is the turbulent Prandtl number, a model constant usually set to $\sigma_k = 1$. An exact transport equation for ε can be derived analogously to the k equation, and then turned into a modeled equation with the same closures. Another, simpler way to directly obtain the modeled ε equation is to modify the k equation through dimensional analysis. The modeled ε equation reads

$$\frac{\partial \varepsilon}{\partial t} + \overline{v}_j \frac{\partial \varepsilon}{\partial x_j} = \frac{\varepsilon}{k} C_{\varepsilon 1} \nu_t \left(\frac{\partial \overline{v}_i}{\partial x_j} + \frac{\partial \overline{v}_j}{\partial x_i} \right) \frac{\partial \overline{v}_i}{\partial x_j} - C_{\varepsilon 2} \frac{\varepsilon^2}{k} + \frac{\partial}{\partial x_j} \left[\left(\nu + \frac{\nu_t}{\sigma_\varepsilon} \right) \frac{\partial \varepsilon}{\partial x_j} \right] \tag{2.34}$$

where σ_ε is the Prandtl number for the turbulent dissipation rate and is set to $\sigma_\varepsilon = 1.3$. $C_{\varepsilon 1}$ and $C_{\varepsilon 2}$ are empirically tuned model constants set to $C_{\varepsilon 1} = 1.44$ and $C_{\varepsilon 1} = 1.92$. Now, k and ε are obtained by solving their transport equations, Eqs. (2.33) and (2.34). Therefore, together with the Navier-Stokes and continuity equations, a set of six transport equations needs to be solved for six unknowns. The turbulent viscosity, ν_t, is obtained from Eq. (2.31). This turbulence model, consisting of Eqs. (2.33) and (2.34), is called the standard k-ε model.

The Boussinesq assumption, Eq. (2.28), is given again here, introducing a different notation.

$$\rho \overline{v_i' v_j'} = -\mu_t \left(\frac{\partial \overline{v}_i}{\partial x_j} + \frac{\partial \overline{v}_j}{\partial x_i} \right) + \frac{2}{3} \rho \delta_{ij} k = -2\mu_t \overline{s}_{ij} + \frac{2}{3} \rho \delta_{ij} k \tag{2.35}$$

Where s_{ij} is the strain-rate tensor, which is a symmetric tensor defined as

$$s_{ij} = \frac{1}{2} \left(\frac{\partial v_i}{\partial x_j} + \frac{\partial v_j}{\partial x_i} \right) \tag{2.36}$$

It is obvious that the normal components of the Reynolds stress tensor, e.g. $\overline{v_1' v_1'}$, must physically always be non-negative, as they are quadratic. However, Eq. (2.35) also allows for negative values of the Reynolds stress components, as

$$\overline{v_1'^2} = -2\nu_t \frac{\partial \overline{v}_1}{\partial x_1} + \frac{2}{3} k \tag{2.37}$$

can become negative if $\partial \overline{v}_1 / \partial x_1$ is sufficiently large, which is unphysical. The requirement of the normal components of the Reynolds stress tensor being non-negative is a typical so-called realizability constraint[8]. A simple modification of the standard k-ε model that prohibits negative normal Reynolds stresses leads to the realizable k-ε model. As the strain rate tensor, $\overline{s}_{ij}$, is a symmetric tensor it has real eigenvalues and the coordinate system can be rotated in such a way

that the coordinate directions correspond to the principal coordinate directions. Then, the off-diagonal components of the tensor are zero and the diagonal components assume a maximum. Therefore, it is in this coordinate system that the normal components of $\overline{v_i' v_j'}$ are most likely to become negative. Hence, with $\max(\lambda)$ denoting the largest eigenvalue of $\overline{s}_{ij}$, Eq. (2.37) can be rewritten for the case where negative normal stresses are most likely to occur as

$$\overline{v_1'^2} = -2\nu_t \max(\lambda) + \frac{2}{3}k \tag{2.38}$$

which can be used to formulate a limiter for the turbulent viscosity, ν_t, to ensure realizability through[14]

$$\nu_t \leq \frac{k}{3|\max(\lambda)|} \tag{2.39}$$

The realizable k-ε model has been shown to give more accurate predictions of flows involving separation, rotation, axisymmetric jets and streamline curvature than the standard k-ε model[7].

2.3 Compressible Flow

For compressible flow problems, classical Reynolds decomposition is usually replaced by Favre decomposition. This is done because the momentum equations then take a simpler form. Favre decomposition is given by

$$\phi = \widetilde{\phi} + \phi'' \tag{2.40}$$

where $\widetilde{\phi}$ denotes the density-weighted Reynolds average, i.e.

$$\widetilde{\phi} = \frac{\overline{\rho\phi}}{\overline{\rho}} \tag{2.41}$$

Using Reynolds decomposition for p and ρ, and Favre decomposition for all other variables, and then Reynolds averaging the equations, the governing equations of the flow are obtained. The continuity equation reads

$$\frac{\partial(\overline{\rho})}{\partial t} + \frac{\partial(\overline{\rho}\widetilde{v}_i)}{\partial x_i} = 0 \tag{2.42}$$

The momentum equations read

$$\frac{\partial(\overline{\rho}\widetilde{v}_i)}{\partial t} + \frac{\partial(\overline{\rho}\widetilde{v}_i\widetilde{v}_j)}{\partial x_j} = -\frac{\partial\overline{p}}{\partial x_i} + \frac{\partial}{\partial x_j}\left[\mu\left(\frac{\partial\widetilde{v}_i}{\partial x_j} + \frac{\partial\widetilde{v}_j}{\partial x_i}\right) - \frac{2}{3}\mu\frac{\partial\widetilde{v}_k}{\partial x_k}\delta_{ij}\right] - \frac{\partial\left(\overline{\rho v_i'' v_j''}\right)}{\partial x_j} \tag{2.43}$$

The Reynolds stress tensor in Eq. (2.43) can now be modeled through the Boussinesq assumption, analogous to the incompressible version of Eq. (2.43). The Boussinesq assumption for compressible flow reads

$$-\overline{\rho v_i'' v_j''} = \mu_t\left(\frac{\partial\widetilde{v}_i}{\partial x_j} + \frac{\partial\widetilde{v}_j}{\partial x_i}\right) - \frac{2}{3}\delta_{ij}\left(\overline{\rho}k + \mu_t\frac{\partial\widetilde{v}_k}{\partial x_k}\right) \tag{2.44}$$

Using the Boussinesq assumption, Eq. (2.43) takes the following form.

$$\frac{\partial(\overline{\rho}\widetilde{v}_i)}{\partial t} + \frac{\partial(\overline{\rho}\widetilde{v}_i\widetilde{v}_j)}{\partial x_j} = -\frac{\partial(\overline{p} + 2\overline{\rho}k/3)}{\partial x_i} + \frac{\partial}{\partial x_j}\left[(\mu + \mu_t)\left(\frac{\partial\widetilde{v}_i}{\partial x_j} + \frac{\partial\widetilde{v}_j}{\partial x_i} - \frac{2}{3}\delta_{ij}\frac{\partial\widetilde{v}_k}{\partial x_k}\right)\right] \tag{2.45}$$

9

The turbulent viscosity is, like in incompressible flow, calculated as

$$\mu_t = \overline{\rho} C_\mu \frac{k^2}{\varepsilon} \tag{2.46}$$

The modeled k-equation for compressible flow reads

$$\frac{\partial(\overline{\rho}k)}{\partial t} + \frac{\partial(\overline{\rho}\widetilde{v}_j k)}{\partial x_j} = \frac{\partial}{\partial x_j}\left[\left(\mu + \frac{\mu_t}{\sigma_k}\right)\frac{\partial k}{\partial x_j}\right] + P^k - \overline{\rho}\varepsilon + \overline{\rho}\varepsilon_c \tag{2.47}$$

σ_k is the Prandtl number for turbulent kinetic energy, set to $\sigma_k = 1$. The production of turbulent kinetic energy, P^k is modeled as

$$P^k = 2\mu_t \widetilde{s}_{ij}\widetilde{s}_{ij} \tag{2.48}$$

where $\widetilde{s}_{ij}$ is the Favre-averaged strain-rate tensor. To include effects of compressibility on turbulence, a dilatation dissipation term, ε_c, is included in the k-equation. This compressible dissipation, ε_c, is modeled according to [11] and reads

$$\varepsilon_c = \alpha_1 \varepsilon Ma_t^2 \tag{2.49}$$

where the turbulent Mach number, Ma_t, is calculated as

$$Ma_t = \sqrt{\frac{2k}{c^2}} \tag{2.50}$$

with c denoting the speed of sound. Eq. (2.50) is easily derived using the definition $2k = \overline{v_i' v_i'}$. The model constant is set to $\alpha_1 = 1$ (in agreement with DNS results[11]). The turbulent dissipation, ε, is again calculated from the modeled ε-equation, which for compressible flow reads

$$\frac{\partial(\overline{\rho}\varepsilon)}{\partial t} + \frac{\partial(\overline{\rho}\widetilde{v}_j\varepsilon)}{\partial x_j} = \frac{\partial}{\partial x_j}\left[\left(\mu + \frac{\mu_t}{\sigma_\varepsilon}\right)\frac{\partial \varepsilon}{\partial x_j}\right] + \frac{\varepsilon}{k}C_{\varepsilon 1}P^k - \frac{\varepsilon^2}{k}C_{\varepsilon 2}\overline{\rho} \tag{2.51}$$

where σ_ε is the Prandtl number for the turbulent dissipation rate and is set to $\sigma_\varepsilon = 1.3$. $C_{\varepsilon 1}$ and $C_{\varepsilon 2}$ are empirically tuned model constants set to $C_{\varepsilon 1} = 1.44$ and $C_{\varepsilon 1} = 1.92$. The ideal gas law for averaged quantities, i.e.

$$\overline{\rho}R\widetilde{T} = \overline{p} \tag{2.52}$$

can be used to calculate the non-constant density of the fluid. Obviously, also an equation for the conservation of energy is needed. As for the simulation of the vortex tube and the ejector two very different approaches in modeling the conservation of energy are taken, these equations will be presented in the respective chapters.

2.4 Near-Wall Modeling

In most engineering applications, geometric constraints in the form of solid objects are present, which are called walls. At a wall, the velocity of the fluid equals that of the wall, therefore at a stationary wall, the velocity of the fluid is zero. This is commonly called the no-slip condition. In the vicinity of a wall, a boundary layer is formed, where the velocity decreases from the free stream velocity, v_∞, to zero. The boundary layer has a thickness, δ, and is usually divided into an inner region at $0 < y < 0.2\delta$ and an outer region at $0.2\delta < y < \delta$. There are several definitions of δ. One common definition is the requirement that $v(\delta) = 0.99\, v_\infty$.

2.4.1 Wall Variables

Over the inner region of the boundary layer, the total shear stress can be approximated as being constant, with viscous shear being dominant in close vicinity of the wall, and Reynolds stress being dominant further away from the wall, where the sum of viscous and Reynolds stress is constant. The purely viscous shear stress is given by

$$\tau_w = \mu \left. \frac{\partial \overline{v}_x}{\partial y} \right|_{y=0} \tag{2.53}$$

With τ_w being approximately constant, it is possible to derive characteristic constants for normalization of wall variables. The characteristic velocity is given by

$$v_\tau = \sqrt{\frac{\tau_w}{\rho}} \tag{2.54}$$

Using Eq. (2.54) it is possible to define a characteristic length scale of the wall as

$$l_\tau = \frac{\nu}{v_\tau} \tag{2.55}$$

and furthermore, using Eq. (2.55), a dimensionless wall distance y^+ is defined as

$$y^+ = \frac{y}{l_\tau} \tag{2.56}$$

Using this wall distance, the the inner boundary layer is usually divided into three sub-layers, depending on whether viscous stresses or Reynolds stresses make up the majority of the near-wall stresses.

$$\text{inner boundary layer} \begin{cases} \text{viscous sub-layer} & 0 < y^+ < 5 \\ \text{buffer sub-layer} & 5 < y^+ < 30 \\ \text{fully turbulent sub-layer} & 30 < y^+ < 300 - 500 \end{cases}$$

2.4.2 Wall Functions

To overcome the computational costs associated with resolving all physical effects in the vicinity of a wall, where gradients are very high and therefore a fine computational grid is required, it is standard practice to employ so-called wall functions. A wall function models the physical phenomena near a wall through simple algebraic, empirical equations, so that the Navier-Stokes equations only have to be calculated starting at a point further away from the wall. The output of a wall function is information on velocities, temperature and, depending on the used turbulence model, turbulent quantities at the first computational grid point close to the wall.

Integration of Eq. (2.53) leads, under the approximation that $\tau_w = const.$, to

$$\overline{v}_x = \frac{\tau_w y}{\rho \nu} + C \tag{2.57}$$

Applying the no-slip boundary condition at the wall, i.e. $\overline{v}_x|_{y=0} = 0$ leads to $C = 0$, and therefore Eq. (2.57) simplifies, together with Eq. (2.54), to

$$\overline{v}_x = \frac{\tau_w y}{\rho \nu} = \frac{v_\tau^2 y}{\nu} \tag{2.58}$$

11

Using the definition $v^+ = v/v_\tau$ and Eqs. (2.54) and (2.55), Eq. (2.58) simplifies to

$$\overline{v}^+ = y^+ \tag{2.59}$$

Therefore, in the viscous sub-layer, the velocity increases linearly with the wall distance. In the fully turbulent sub-layer, Reynolds stress becomes the dominant part of τ_w, yielding

$$\tau_w = -\rho\overline{v_x'v_y'} \tag{2.60}$$

Using Prandtl's mixing length model, Eq. (2.30), and the assumption that near the wall $\partial v_y/\partial v_x = 0$, leads to

$$\frac{\tau_w}{\rho} = l^2\left(\frac{\partial\overline{v}_x}{\partial y}\right)^2 = \kappa^2 y^2\left(\frac{\partial\overline{v}_x}{\partial y}\right)^2 \tag{2.61}$$

where κ is the von Kárman constant. Using Eq. (2.54) τ_w can be expressed in terms of v_τ to yield

$$v_\tau^2 = \kappa^2 y^2\left(\frac{\partial\overline{v}_x}{\partial y}\right)^2 = const. \tag{2.62}$$

Eq. (2.62) is now integrated to give the logarithmic law of the wall, often called log-law, which, using wall variables, reads

$$\overline{v}^+ = \frac{1}{\kappa}\ln(y^+) + B \tag{2.63}$$

with $B \approx 5$ being a constant. Therefore, in the buffer sub-layer the velocity changes from the linear profile of the viscous sub-layer to the logarithmic profile of the fully turbulent sub-layer. A temperature profile is obtained in the same way and reads

$$\overline{T}^+ = \frac{1}{\kappa_T}\ln(y^+) + B_T \tag{2.64}$$

Wall functions using the log-law as in Eqs. (2.63) and (2.64) are called standard wall functions and give relatively good results for many applications. However, flows with strong pressure gradients, or impinging jets are poorly modeled by the log-law and require more sophisticated wall functions, which will not be discussed here.

3 Numerical Methods

In this chapter, the numerical methods used to solve the governing equations laid out in chapter 2 are explained. Case-specific numerical schemes and aspects that are only relevant for the simulation of either the vortex tube or the ejector are presented in the respective chapters.

The most common solution method applied in computational fluid dynamics is the so-called Finite Volume Method. It is found to be particularly suitable for solving conservation equations as the method is based on the principle of local conservation, and this is the reason for its wide use in fluid mechanics. The Finite Volume Method involves the following steps[10]:

- Spatial discretization of the computational domain into a finite number of volumes, which are called cells.

- Integration of all governing equations over each finite volume to obtain algebraic equations for the unknown variables.

- Linearization of the algebraic equations and iterative solution of the thus obtain set of linear equations.

These steps are outlined below in more detail.

3.1 Meshing

In order to integrate the conservation equations over a finite number of volumes, the geometric domain of the problem needs to be divided into these volumes. This process is called meshing, as a computational mesh or grid is created. The easiest way of realizing such a discretization would be to divide a cube into several, equally sized smaller cubes. However, geometries can have various shapes and therefore, depending on the actual problem, different kind of cells are used to mesh a given domain. Depending on the shape, these are called tetrahedral, hexahedral, pyramidic, prismatic or polyhedral (e.g. dodecahedral) cells. In two dimensions, usually triangles and quadrilateral cells are used, but it is of course possible to use any kind of cell, e.g. hexagons are also commonly used for two-dimensional meshing. Examples of different cell types can be seen in Figure 3.1. Two important measures of cell quality are the *skewness* and the *aspect ratio* of a cell.

The aspect ratio is the ratio between the greatest and smallest edge length, therefore a hexahedral cell with an aspect ratio of two is two times longer than wide. If the nature of a flow is not known, it is good practice to keep the aspect ratio around unity. If, however, the flow is strongly convective and the direction of convective transport is known, it is possible to use a mesh with cells that are elongated in the direction of convective transport. An example for such a situation is the flow along a flat wall. The gradients of velocity will be high in the wall-normal direction, requiring a dense grid in that direction to minimize the error introduced by spatial discretization. In the direction of the flow, however, gradients will be small, leading to the requirement of a less densely spaced grid in that direction.

Skewness denotes the deviation from a cell with equal angles. For a hexahedral cell, the skewness is zero if all corners have angles of $90°$. Often, skewness is replaced by *orthogonal quality*, where (orthogonal quality) $=(1-$skewness$)$. High skewness can lead to very poor numerical behaviour, as a cell can then have two neighbouring faces with close to opposing normal vectors, which introduces high errors in the calculation of face-normal fluxes and can also cause a division by a value that is in the order of magnitude of the computer's rounding error, causing a division by zero error.

13

It is considered best-practice to keep average skewness < 0.33 and maximum skewness < 0.95[7]. Generally, grids can be divided into structured and unstructured gris. A structured grid consists

2D

Triangle   Quadrilateral   Hexagon

3D

Tetrahedron   Hexahedron   Prism
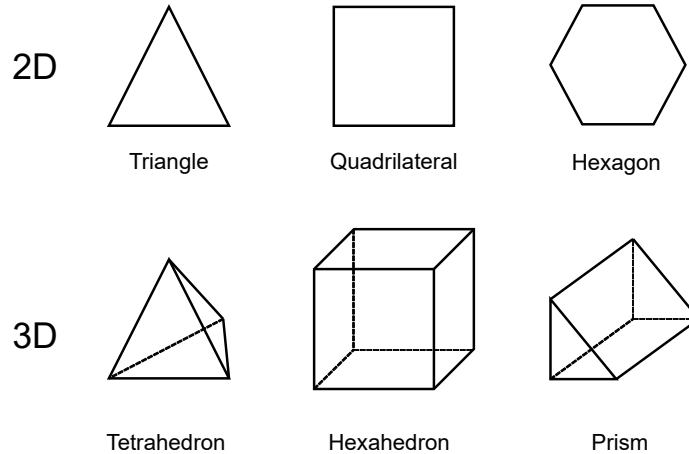
Figure 3.1: Examples of different 2D and 3D cell types

only of quadrilateral (for 2D) or hexahedral (for 3D) cells, which can easily be represented in a two- or three- dimensional array and make finding neighbouring cells computationally easy. Unstructured grids consist of any type (or mix of types) of cells. In general, computations are faster on structured grids[7]. Furthermore, grids can be classified as being conformal or non-conformal. Conformal grids do not have hanging nodes, which are nodes that are located on another cell's face. Therefore, in a conformal grid, each face coincides with exactly one face of another cell, where in a non-conformal grid one cell's face can be made up of a number of other cells' faces. Calculating the flux from one cell to another in a non-conformal grid is introducing an additional error. An example of these two types of grids can be seen in Figure 3.2, where the example of transition from a coarse to a fine grid is given, which is a common issue where one has to decide between using a conformal or a non-conformal grid.

Conformal Mesh   Non-Conformal Mesh
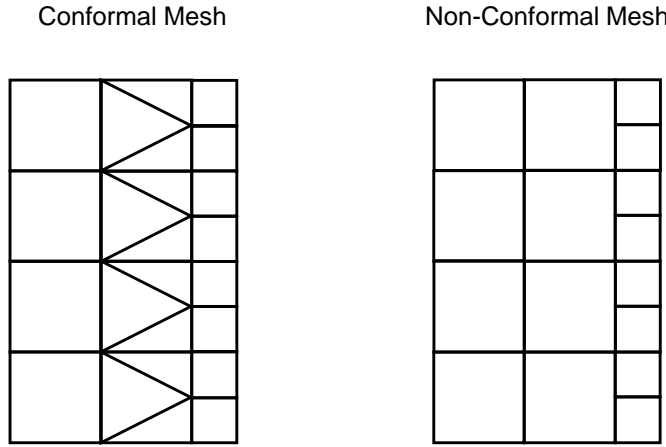
Figure 3.2: Example of a conformal (left) and non-conformal (right) grid in 2D

3.2 Integration and Linearization of the Transport Equations

An arbitrary conservation equation for a scalar (an equation for a vector, e.g. the Navier-Stokes equation, is a set of scalar transport equations for the individual scalar components of the vector) that includes a convection term, a diffusion term and a source term reads

$$\frac{\partial(\rho\phi)}{\partial t} + \frac{\partial(\rho v_j \phi)}{\partial x_j} = \frac{\partial}{\partial x_j}\left(\Gamma\frac{\partial\phi}{\partial x_j}\right) + S_\phi \tag{3.1}$$

Integrating Eq. (3.1) over a control volume (i.e. a cell of the computational grid) yields

$$\int_{CV}\frac{\partial(\rho\phi)}{\partial t}dV + \int_{CV}\frac{\partial(\rho v_j \phi)}{\partial x_j}dV = \int_{CV}\frac{\partial}{\partial x_j}\left(\Gamma\frac{\partial\phi}{\partial x_j}\right)dV + \int_{CV}S_\phi dV \tag{3.2}$$

Using the theorem of Gauss[13] a volume integral can be transformed into an integral over a closed surface enclosing V if the integrand can be expressed as the divergence of a vector field. Therefore

$$\int_V \nabla\cdot\vec{f}dV = \int_S \vec{n}\vec{f}dS \tag{3.3}$$

with $\vec{n}$ being a normal vector pointing outwards the surface S. Applying Eq. (3.3) to the convective term of Eq. (3.2) leads to

$$\int_{CV}\frac{\partial(\rho v_j \phi)}{\partial x_j}dV = \int_{CS}\rho v_j n_j \phi dS_j \tag{3.4}$$

Considering a structured hexahedral grid where CV is a single hexahedral cell (cf. Figure 3.3) having six faces (top, bottom, north, south, west, east) which fully enclose CV and therefore form

15
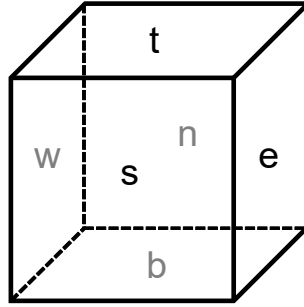
Figure 3.3: Schematic drawing of an arbitrary hexahedral cell

CS, Eq. (3.4) can be evaluated as

$$\int_{CS} \rho v_j n_j \phi dS_j = -\left[(\rho u S \phi)_w - (\rho u S \phi)_e + (\rho v S \phi)_s - (\rho v S \phi)_n + (\rho w S \phi)_t - (\rho w S \phi)_b\right] \tag{3.5}$$

with S being the surface area of the respective face and u,v and w denoting the velocity component normal to the respective face. The density ρ is generally different at the respective faces and therefore not moved outside the brackets. When integrating the diffusion term of Eq. (3.1), the theorem of Gauss can again be used.

$$\int_{CV} \frac{\partial}{\partial x_j}\left(\Gamma\frac{\partial \phi}{\partial x_j}\right)dV = \int_{CS} \Gamma\frac{\partial \phi}{\partial x_j}n_j dS =$$
$$-\left[\left(\frac{\partial \phi}{\partial x}S\Gamma\right)_w - \left(\frac{\partial \phi}{\partial x}S\Gamma\right)_e + \left(\frac{\partial \phi}{\partial y}S\Gamma\right)_s - \left(\frac{\partial \phi}{\partial y}S\Gamma\right)_n + \left(\frac{\partial \phi}{\partial z}S\Gamma\right)_t - \left(\frac{\partial \phi}{\partial z}S\Gamma\right)_b\right] \tag{3.6}$$

The source term of Eq. (3.1) can e.g. be the pressure gradient term of the Navier-Stokes equations. A simple way to solve its volume integral in Eq. (3.2) is to take a cell mean value of S_ϕ and thus move the term outside of the integral.

$$\int_{CV} S_\phi dV \approx \overline{S}_\phi V \tag{3.7}$$

The time derivative in Eq. (3.2) is moved out of the integral to yield

$$\int_{CV} \frac{\partial(\rho\phi)}{\partial t}dV = \frac{\partial(\rho\phi)}{\partial t}V \tag{3.8}$$

16

Together, this gives the discretized form of Eq. (3.2) for an arbitrary computational cell (i.e. the control volume).

$$\frac{\partial(\rho\phi)}{\partial t}V + \sum_f^{n_{faces}} \rho_f v_j \phi_f n_j A_f = \sum_f^{n_{faces}} \Gamma\frac{\partial\phi_f}{\partial x_j}n_j A_f + SV \qquad (3.9)$$

Eq. (3.9) is an algebraic equation except for the yet unknown gradient and face values of ϕ that need to be determined in some way. The methods used to determine these unknown values are presented below. Naturally, the face values and gradients of ϕ will be dependent on its values in the neighbouring cells, and generally this dependence will be nonlinear. Linearization of Eq. (3.9) gives an equation of the form[10]

$$a_c\phi_c = \sum_{nb} a_{nb}\phi_{nb} + b \qquad (3.10)$$

where subscript c denotes the considered cell and subscript nb denotes any neighbouring cells and a_c, a_{nb} and b are the coefficients of the linearized version of Eq. (3.9). Except for cells at boundaries such as walls, inlets or outlets, the number of a cell's neighbours is equal to that of its faces. Formulating Eq. (3.10) for each cell in the computational domain yields a set of algebraic equations that can be solved using a typical solver for systems of linear equations. The most common methods are variants of the family of Gauss-Seidel algorithms[7].

3.2.1 Gradient Calculation

Green-Gauss Method

A common method to calculate gradients is the Green-Gauss method[15], where again the theorem of Gauss is used. The gradient at the center c_0 of a cell, $(\nabla\phi)_0$, is calculated as

$$(\nabla\phi)_0 = \frac{1}{V}\sum_f \overline{\phi}_f \vec{n}_f S_f \qquad (3.11)$$

with S_f being the surface area of each face and $\vec{n}_f$ the respective outward-pointing normal vector of the face. The value of $\overline{\phi}_f$ can either be taken as arithmetic average of the cell values at the neighbouring cells, or as arithmetic average of nodal values on the face of interest.

Least-Squares Method

Another way to calculate the gradient $(\nabla\phi)_0$ is Least-Squares Cell-Based evaluation[15]. The difference between the cell of interest, c_0, and another cell, c_i, along a vector $\Delta\vec{r}_{0i}$ that points from the cell center of c_0 to the cell center of c_i reads

$$(\nabla\phi)_0 \cdot \Delta\vec{r}_{0i} = (\phi_i - \phi_0) \qquad (3.12)$$

where

$$\Delta\vec{r}_{0i} = \vec{r}_i - \vec{r}_0 \qquad (3.13)$$

Eq. (3.12) is a system of equations that can be written in compact form as

$$\underline{J}(\nabla\phi)_0 = \Delta\phi_i \qquad (3.14)$$

17

where $\underline{J}$ is a coefficient matrix being solely dependent on the geometry. The system of equations given in Eq. (3.14) is generally over-determined, as there exist more neighbours c_i to c_0 than coordinate directions and the solution is not necessarily linear. This leads to an optimization problem that, in a least-square sense, is solved by finding the minimum of the following functional

$$F = \sum_{i=1}^{i=N_{NB}} \left(w_i \left[\phi_i - (\phi_0 + \nabla \phi_0 \cdot \vec{r}_{0i}) \right]^2 \right) \tag{3.15}$$

with w_i being a weighting factor. The minimization of F is realized through

$$\frac{\partial F}{\partial \left(\frac{\partial \phi}{\partial x} \right)} = \frac{\partial F}{\partial \left(\frac{\partial \phi}{\partial y} \right)} = \frac{\partial F}{\partial \left(\frac{\partial \phi}{\partial z} \right)} = 0 \tag{3.16}$$

3.2.2 Face Value Calculation

In Eqs. (3.5), (3.6), the value of ϕ at the faces of each control volume must be calculated. There are several ways in which this can be achieved. Consider a cell neighbourhood where cell P is neighboured by cells W and E, with faces w and e separating the respective cells from P, depicted in Figure 3.4. Let the flow be dominated by convection, where the velocity is pointing from W to E.

Figure 3.4: Cell neighbourhood and direction of convective transport
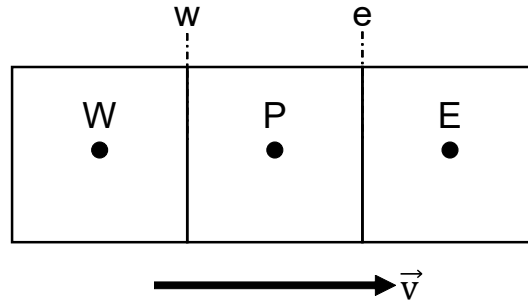
Central Differencing Scheme

Linear interpolation between neighbouring cells (or the mean value of two neighbouring cell values for an equidistant grid) gives a simple way to calculate face values. For the equidistant grid shown in Figure 3.4 this yields

$$\phi_w = \frac{\phi_W + \phi_P}{2} \tag{3.17}$$

$$\phi_e = \frac{\phi_P + \phi_E}{2} \tag{3.18}$$

18

Discretization schemes should, to give physically reasonable results, fulfill two criteria: boundedness and transportiveness[7]. Boundedness requires a scheme to yield only variables that are bounded by (i.e. neither greater nor smaller than) all input values of that scheme. As can be seen easily from Eqs. (3.17) and (3.18), the central differencing scheme is bounded. Transportiveness requires a scheme to take into account the direction of convective transport. The central differencing scheme does not distinguish between directions when calculating face values, which for flows with strong convection can yield unphysical results. A measure of convectiveness is the Péclet number, defined as[7]

$$\text{Pe} = \frac{\text{transport by convection}}{\text{transport by diffusion}} = \frac{\rho v}{\Gamma/\Delta x} \tag{3.19}$$

Another class of discretization schemes fulfils the requirement of transportiveness: the upwind schemes. Upwind schemes calculate face values dependent on upstream cell values only.

First-Order Upwind Scheme

In the first-order upwind scheme, the value of a face is simply the value of the respective upwind cell. Therefore, in the above example

$$\phi_w = \phi_W \tag{3.20}$$

$$\phi_e = \phi_P \tag{3.21}$$

Second-Order Upwind Scheme

A more accurate way of calculating face values is the second-order upwind scheme, where face values depend on two upstream cells. It is assumed that the gradient at both the e and w face is equal. With x being the axial (flow direction) coordinate, the scheme - again for the above case - reads

$$\frac{\phi_e - \phi_P}{x_e - x_P} = \frac{\phi_P - \phi_W}{x_P - x_W} \tag{3.22}$$

$$\phi_e = \frac{(\phi_P - \phi_W)(x_e - x_P)}{x_P - x_W} + \phi_P \tag{3.23}$$

which for an equidistant grid like that in Figure 3.4 yields

$$\phi_e = 1.5\phi_P - 0.5\phi_W \tag{3.24}$$

The order n of a discretization scheme gives information about its accuracy, as the error ζ of a scheme decreases with $\zeta \propto \Delta x^n$. Therefore, the error of the second-order upwind scheme decreases to 1/4 when the grid size Δx is halved. However, the second-order upwind scheme is unbounded, which makes it less stable and requires physically meaningful initial values. To take care of this, it is common practice to initially use first-order discretization schemes to obtain a first solution and then take this result as initialization for a solution employing a higher-order scheme.

Third-Order QUICK Scheme

The QUICK (Quadratic Upstream Interpolation for Convective Kinetics) scheme is a third-order accurate scheme that is transportive but unbounded[7]. It is only applicable when cells are quadrilateral (in 2D) or hexahedral (in 3D)[10] and uses a weighted average of the values calculated with

19

the second-order upwind scheme and central second order interpolation, respectively. Using again the schematic cell neighbourhood depicted in Figure 3.4, the value of ϕ_e at the eastern face is calculated as

$$\phi_e = \theta \left[\frac{d_E}{d_E + d_P} \phi_P + \frac{d_P}{d_E + d_P} \phi_E \right] + (1 - \theta) \left[\frac{d_W + 2d_P}{d_W + d_C} \phi_P - \frac{d_P}{d_W + d_C} \phi_P \right] \quad (3.25)$$

where d is the length of the respective cell. $\theta = 0$ gives a second-order upwind scheme and $\theta = 1$ gives a central second-order interpolation scheme. Typically, $\theta = 1/8$ for the QUICK scheme.

Third-Order MUSCL Scheme

The MUSCL (Monotone Upstream-Centered Schemes for Conservation Laws) is a third-order accurate scheme similar to the QUICK scheme. It blends a second order upwind scheme with a central differencing scheme. The face value is calculated as

$$\phi_f = \theta \phi_{f,CD} + (1 - \theta)\phi_{f,SOU} \quad (3.26)$$

where $\phi_{f,CD}$ and $\phi_{f,SOU}$ are the face values of ϕ obtained with a central differencing scheme and a second-order upwind scheme, respectively. An advantage of the MUSCL scheme over the QUICK scheme is that it is usable on any cell types[7] (whereas QUICK is limited to quadrilateral/hexahedral cells).

3.2.3 Pressure Interpolation

Like outlined above for convectively transported scalars and velocity components, also the value of the pressure at faces is unknown and needs to be calculated. However, as pressure is not a scalar which is transported by convection or diffusion, different interpolation schemes are needed.

Linear Scheme

The linear scheme is the most basic scheme to interpolate the value of pressure at the face between two cells. It is done by simply taking an average of the cell values in the cells adjacent to the face of interest[10]. Therefore, using the example cell neighbourhood of Figure 3.4

$$p_e = \frac{p_P + p_E}{2} \quad (3.27)$$

Second-Order Scheme

The second-order pressure interpolation scheme uses central differencing between the two adjacent cells to calculate the face pressure[10]. Therefore (for the one-dimensional case of Figure 3.4)

$$p_e = \frac{1}{2} \left(p_P + p_E \right) + \frac{1}{2} \left((x_e - x_P) \left. \frac{\partial p}{\partial x} \right|_P + (x_e - x_E) \left. \frac{\partial p}{\partial x} \right|_E \right) \quad (3.28)$$

3.2.4 Temporal Discretization

Temporal discretization is realized by dividing time into finitely small time steps Δt. Then, to calculate the value of a variable at a given time $t + \Delta t$, there exist two very different approaches: explicit and implicit methods.

Explicit Methods

In explicit algorithms, the value of a variable ϕ at a time $t + \Delta t$ is calculated as

$$\phi(t + \Delta t) = \phi(t) + \Delta t \left. \frac{d\phi}{dt} \right|_t \tag{3.29}$$

which is the well-known forward Euler method.

Implicit Methods

In implicit methods, $\phi(t + \Delta t)$ is calculated using its time derivative at $t + \Delta t$, therefore

$$\phi(t + \Delta t) = \phi(t) + \Delta t \left. \frac{d\phi}{dt} \right|_{t+\Delta t} \tag{3.30}$$

which is the well-known backward Euler method. As the value of the derivative at $t + \Delta t$ is not known, the implicit scheme needs to be solved iteratively, which makes it computationally more expensive than the explicit scheme. However, the implicit scheme allows for greater time steps, which can make up for the computational costs of iterating. In terms of accuracy, both formulations, Eq. (3.29) and Eq. (3.30), are first-order accurate, as information from one time step is used to calculate the evolution of ϕ.

An example for a second-order accurate time integration method is the Crank-Nicolson method, which blends the fully explicit and fully implicit method. It reads

$$\phi(t + \Delta t) = \phi(t) + \frac{\Delta t}{2} \left(\left. \frac{d\phi}{dt} \right|_{t+\Delta t} + \left. \frac{d\phi}{dt} \right|_t \right) \tag{3.31}$$

As this method is of second-order accuracy, the error decreases with the square of the time step, but it involves an implicit part and therefore needs to be solved iteratively.

Time Step Size

Fully explicit schemes are very sensitive to the size of Δt, as they are only conditionally bounded, therefore they become unbounded if the time step becomes too large. The largest possible time step is, for a fully explicit algorithm, the shorter of the times it takes for a quantity to be transported through a cell either by convection or diffusion. For an implicit solver, this time step can be larger, as also information at $t + \Delta t$, and therefore at the respective upstream cells is taken into account. These restrictions can be expressed through the Courant-Friedrichs-Lewy condition[7]

$$\Delta t < \text{CFL} \cdot \min \left(\frac{\rho (\Delta x)^2}{\Gamma}, \frac{\Delta x}{v} \right) \tag{3.32}$$

where CFL is the Courant number, with CFL = 1 for an explicit solver and CFL > 1 for a fully implicit solver, with theoretically no upper limit (in terms of numerical stability), but in practice depending strongly on the quality of the initial guess and the order of accuracy of the used scheme. Therefore it is good practice to keep CFL low initially also for implicit algorithms. The two terms on the right-hand side of Eq. (3.32) represent the time it takes for a quantity to be transported through a cell of size Δx by either diffusion (left term) or convection (right term).

3.3 Solving the Equations

3.3.1 Pressure-Based Solver

The method used in this work to iteratively solve the underlying equations (in their algebraic form obtained using the Finite Volume Method, as outlined above) is the so-called pressure-based solver of the commercial CFD code ANSYS FLUENT[10]. Here, instead of solving the continuity equation itself, a pressure equation is solved that is derived from the continuity and momentum equations. Therefore, the pressure obtained from the pressure equation, ensures that the velocity field satisfies the continuity equation. The momentum equations and the pressure equation can be solved either in a coupled or segregated manner.

In the segregated approach the momentum equations are, in each iteration, solved sequentially (i.e. the three components are solved one-by-one) using the pressure value obtained in the previous iteration step. Then, the thus obtained values for velocity are used to calculate a new pressure. After that, all additional scalars, such as turbulence quantities (e.g. k) or energy are calculated. Finally, density and material properties are updated and the next iteration step is started with solving the velocity field through the momentum equations. One of the most commonly used segregated algorithms for coupling the velocity and pressure equations is the SIMPLE (Semi-Implicit Method for Pressure-Linked Equations) algorithm.

In the coupled algorithm, the components of the momentum equations and the pressure equation are solved simultaneously as a system of coupled equations, which generally speeds up computational times compared to the segregated algorithm but requires more memory.

The other main class of solver algorithms are the density-based solvers, which directly solve the continuity equation for density. The density-based solvers are not discussed here as they are not used in this work.

3.3.2 Under-Relaxation of Variables

When iteratively solving the underlying equations, it is often helpful to under-relaxate the solution. This is done by introducing an under-relaxation factor $\alpha \in \,]0, 1]$ so that when calculating the value of a variable ϕ

$$\phi_{n,new} = \alpha\phi_n + (1-\alpha)\phi_{n-1} \tag{3.33}$$

where in Eq. (3.33) $\phi_{n,new}$ is the value of ϕ that is used as result of the nth iteration (instead of ϕ_n), and ϕ_n and ϕ_{n-1} are the values calculated by the solver during the nth and the $(n-1)^{th}$ iteration, respectively. Generally, lowering the value of α can enhance stability, but comes at the cost of additional computational time. It is common practice to keep α low during the first iterations and, to speed up computations, increase the value once a converging behaviour of the equations is achieved. The under-relaxation of variables is also called explicit relaxation.

Another technique of under-relaxation is so-called higher-order term relaxation[10]. As higher-order discretization schemes (e.g. second-order upwind, QUICK, etc.) are usually unbounded and a bad initial guess can, through the nonlinear terms, cause the solution to take unphysical values or totally diverge, these schemes can be regrouped as first order schemes with additional, higher-order terms. Then, higher-order term relaxation factors can be used to choose a lower under-relaxation factor for the higher-order terms of the discretization schemes. This allows the solution to converge faster, by letting the first-order part of the discretization scheme take higher under-relaxation factors at less cost in numerical stability.

22

3.3.3 Under-Relaxation of Equations

When solving a steady-state case, the derivatives with respect to time in all equations are omitted, and CFL as introduced above is not applicable. However, when using ANSYS FLUENT to solve a steady-state case, CFL can be used as an additional under-relaxation parameter[10]. While the above-mentioned under-relaxation factor α is used when updating individual variables, another under-relaxation factor is introduced in the algebraic equations themselves, which are of the form of Eq. (3.10) and are iteratively solved for every cell during each iteration. This under-relaxation takes the form of

$$a_c\phi_{c,new} = \sum_{nb} \alpha a_{nb}\phi_{nb} + \alpha b + (1-\alpha)a_c\phi_{c,old} \tag{3.34}$$

where the value of α in Eq. (3.34) is determined (only in steady-state calculations, when there is no time advancement) by choosing a value of the CFL.

$$\frac{1-\alpha}{\alpha} = \frac{1}{\text{CFL}} \tag{3.35}$$

This relation is plotted in Figure 3.5. This form of relaxation is called implicit relaxation, as not the variable that is solved for is relaxated after the iteration, but the equation to be solved is relaxated itself.
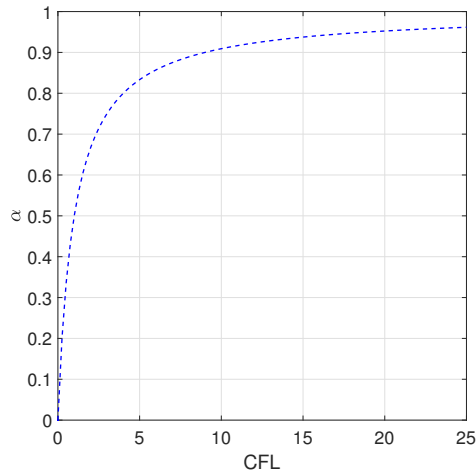
Figure 3.5: Under-relaxation factor α for equations as function of steady-state CFL

3.3.4 Multigrid Method

ANSYS FLUENT, like most other sophisticated CFD codes, uses the multigrid method to accelerate convergence. Within this method, (at least) one additional grid is introduced that is coarser than the original grid. This is done by summing up several cells of the original, finer grid. If e.g. there is a sudden change in pressure, which will physically affect the whole domain almost instantaneously, the

information would have to be transported through the domain cell-by-cell on the fine grid, making the solution process time-consuming. Solving a set of algebraic, linearized equations on both the fine and the newly introduced coarse grid, and exchanging corrections between the two solutions by two processes called restriction (transfer from fine to coarse level) and prolongation (transfer of corrected solution from coarse level back to fine level), accelerates this process as information can be transported through the domain quickly on the coarse level[7, 10].

3.3.5 Measuring Convergence

While iteratively solving the equations, it is important to judge whether a solution has converged, and therefore the solution process can be stopped. A common way to judge convergence is by monitoring of the residuals of the individual equations. The residual is calculated by summing the error of an equation's volume integral for each cell. This value is then scaled by e.g. dividing it by the residual obtained during the first iteration. Therefore, e.g. the residual of the continuity equation can be seen as a local error in mass balance of cells (as opposed to the global error in mass balance of mass entering through the domain's inlets and exiting through the domain's outlets). As the solution of the set of equations is iteratively approached, the residuals decrease. However, if e.g. the starting guess to a problem is very bad, the residuals will turn out to be quite high during the first iterations and thus the scaled residuals will be rather low[7]. Additionally, the level of residuals does not give any information on the physical correctness of the solution. It is therefore common practice to also monitor integral balances such as a global mass and energy balance for the system and variables of interest such as forces, and check for a steady value. Thus, a (steady state) simulation is said to be converged, if all of the following apply.

- Residuals of all equations have dropped by at least three to six (depending on the equation) orders of magnitude compared to the residuals obtained during the first iterations.

- The error of global (over the whole domain) balances of energy and mass is low and steady.

- Quantities of interest, that are the aim of the simulation (e.g. forces on a body in aerodynamic simulations), do not change anymore over the course of iterations.

- The results of the simulation are physically plausible (which for highly complex flows is not always easy to judge). If available, the results should be comparable to experimental data or other numerical studies of similar problems.

- The solution is grid-independent. This means that increasing the cell density does not change the result of the simulation.

4 Vortex Tube

In chapter 4.1, a general overview of vortex tubes, their history, the physical phenomena behind temperature separation and their applications is provided. In chapters 4.2 and 4.3, the mathematical model and numerical methods used within this work to simulate the flow field inside a vortex tube are outlined. Then, simulations using three types of working fluids are performed and presented. Firstly, a vortex tube operated with air is simulated, as air is a commonly used working fluid for vortex tubes, and many experimental and numerical studies of vortex tubes with air are available. This simulation serves as validation of the CFD model and the results are presented in chapter 4.4. As the high pressure fluid leaving the condenser of a heat pump and entering the expansion device is usually a liquid, as a next step, a simulation of a vortex tube operated with a liquid is performed. As studies of vortex tubes with other fluids than gases are rare, water is chosen for this simulation, as for liquid water an experimental investigation was found. The results of this simulation are presented in chapter 4.5. Then, in chapter 4.6, simulations using the synthetic refrigerant R1336MZZ(Z), in a gaseous state, as working fluid are presented. Simulations of liquid or two-phase refrigerants were not performed, as the temperature separation of liquids and two-phase fluids inside a vortex tube was found too low to be relevant for technical applications. In chapter 4.7, the results of a parameter study are presented, where the influence of different geometries and operating conditions on a vortex tube operated with a refrigerant were studied. In chapter 4.8, possible heat pump cycle layouts utilizing vortex tube expansion are discussed. Then, using the results of the CFD simulations to model the vortex tube, a heat pump cycle featuring a vortex tube is simulated on the basis of global balances of energy and mass. The results of this cycle analysis are presented in chapter 4.9.

A summary of the findings on the vortex tube presented in this chapter was accepted for publication in the proceedings of the 13th IEA Heat Pump Conference 2020, Jeju, Korea[16].

4.1 Theoretical Background

A vortex tube, originally invented by Ranque in 1933[17] and substantially refined and investigated by Hilsch in 1946[18], is a device that separates an incoming stream of gas at high pressure into a hot and a cold outflowing low pressure stream, where the hot exit temperature lies above the inlet temperature and the cold exit temperature lies below the inlet temperature. This phenomenon of temperature separation is also called the Ranque-Hilsch effect. Figure 4.1 shows a schematic drawing of a vortex tube. A fluid at high pressure enters the tube tangentially through one or more nozzles. A swirling flow pattern of high angular velocity develops. The fluid separates into a cold stream, leaving the tube close to the center at the side near the inlet and a hot stream, leaving the tube close to the wall on the other side. The fraction of fluid that leaves through the cold exit, called the cold fraction, defined as

$$\gamma = \dot{m}_c / \dot{m}_{in} \tag{4.1}$$

is adjusted by controlling the pressure at the hot exit via a valve. By adjusting the cold fraction, γ, accordingly, Hilsch[18] was able to expand compressed air at 20°C inlet temperature into exiting streams at +200°C and -50°C, respectively. As a vortex tube has a relatively simple geometry, involves no moving parts and requires little maintenance, it serves as a simple device for heating or cooling, given that a pressurized gas is available. According to Ahlborn and Gordon[19], the lower boundary for inlet pressure lies around 1.4 times the outlet pressure, with no fast enough tangential velocities to allow secondary (inner) circulation forming below, and the upper boundary in terms

of inlet pressure is found around 7 times the outlet pressure, as above unfavourable shock waves occur.

Much effort has been put into explaining the physical processes behind the energy separation inside
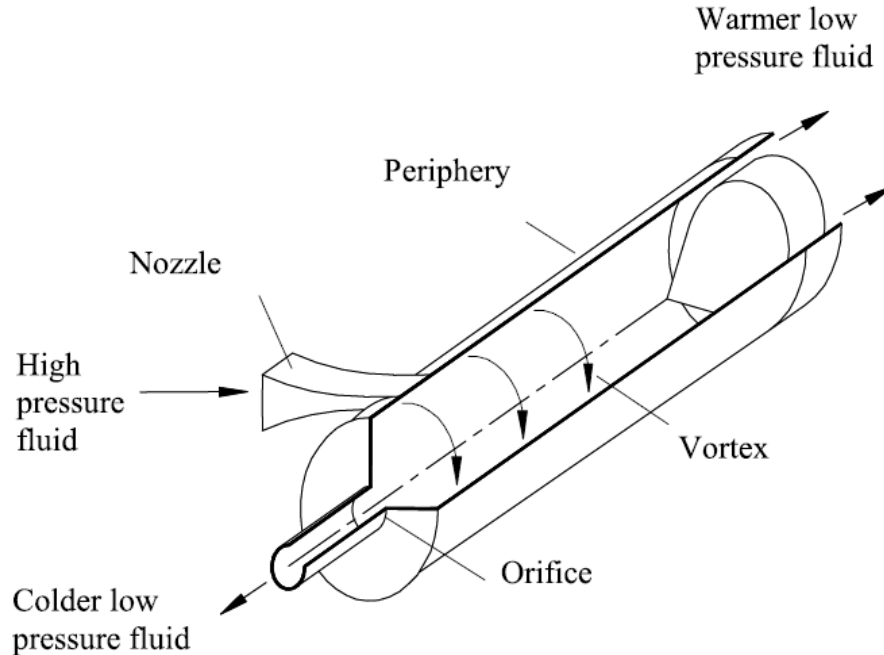

Figure 4.1: Schematic drawing of a vortex tube [20]

a vortex tube, leading to several theories. Hilsch[18] suggested that kinetic energy is transferred via internal friction from the center towards the outer radius of the tube, making shear work the driving mechanism behind the energy separation. Reynolds[21] investigated the mechanisms by conducting an order-of-magnitude analysis of the energy equation, identifying heat and energy fluxes due to three mechanisms: turbulent mixing due to radial pressure and temperature gradients, buoyancy forces and Reynolds shear stresses. All these fluxes point radially outwards. Ahlborn and Gordon[19] drew parallels between a vortex tube and a classical refrigerating cycle. According to them, a vortex tube bears all attributes of a refrigerating cycle, such as temperature separation induced by mechanical work and compression and expansion of a working fluid. They identified the primary loop (close to the wall at the outer radius) as coolant loop, and the inner, recirculating loop as refrigerant loop that is performing heat rejection at the outer radius and energy absorption closer to the center. Based on these observations, a set of analytic formulae for predicting the temperature separation in a vortex tube were developed.

Given a certain geometry and a fixed cold outlet pressure, a vortex tube has four parameters[19]:

- the working fluid

- the inlet temperature T_{in}

26

- the inlet pressure p_{in}

- the hot outlet pressure p_h

Although many investigations have been conducted on changes in temperature, pressure and geometric configurations, the working fluid was mostly air. Studies of the vortex tube with working fluids other than air, especially two-phase fluids or liquids, are rare. Balmer[22] conducted experiments using liquid water as fluid. It was concluded that for inlet pressures of 20 to 50 MPa, a temperature separation of 10 to 20 °C could be obtained, with both the hot and cold exit temperatures lying above the inlet temperature. This indicates that the working fluid does not necessarily need to be compressible in order for a temperature separation to occur. However, the inlet pressure needed to obtain a temperature separation is two orders of magnitude higher than that needed when using a compressible working fluid. Collins and Lovelace[23] investigated the flow of two-phase propane in a vortex tube experimentally and concluded, that for inlet vapor qualities above 80%, a significant temperature separation can be achieved. However, when the inlet vapor quality is lowered below 80%, the temperature separation diminishes rapidly.

4.2 Mathematical Modeling

The flow field inside the vortex tube is classified as steady (as only steady state operating conditions are of interest for this study), three-dimensional, turbulent and compressible, with a single phase present. The continuity equation and Navier-Stokes equation are therefore considered in the form of Eqs. (2.42) and (2.45), but omitting the derivatives with respect to time, as only steady-state simulations are performed. The energy equation is considered in the following form, which is the steady-state, Favre-averaged version of Eq. (2.8).

$$\frac{\partial(\widetilde{v}_j(\overline{\rho}\widetilde{E} + \overline{p}))}{\partial x_j} = \frac{\partial}{x_j}\left(\lambda_{eff}\frac{\partial \widetilde{T}}{\partial x_j}\right) + \Phi \tag{4.2}$$

where $\lambda_{eff} = \lambda + \lambda_t$ is the effective thermal conductivity with λ_t as turbulent thermal conductivity. Furthermore, Φ denotes viscous dissipation, which is given by

$$\Phi = \frac{\partial}{\partial x_j}\left(\widetilde{\tau}_{ij}\widetilde{v}_j\right) \tag{4.3}$$

Often, Φ is neglected as its contribution to Eq. (4.2) is small in many cases. Whether viscous dissipation is of importance can be judged by evaluating the Brinkmann number, Br. For Br approaching or exceeding unity, viscous dissipation usually plays an important role and cannot be neglected[10]. The Brinkmann number is defined as

$$\text{Br} = \frac{\mu v^2}{\lambda \Delta T} \tag{4.4}$$

Using the results of [24] to estimate Br in a typical vortex tube yields

$$\text{Br} \approx \frac{1.8 \cdot 10^{-5}[\text{Pa} \cdot \text{s}] \cdot 180^2[\text{m}^2\text{s}^{-2}]}{2.6 \cdot 10^{-2}[\text{W} \cdot \text{m}^{-1}\text{K}^{-1}] \cdot 26[\text{K}]} = 0.86 \tag{4.5}$$

Therefore, and bearing in mind, that the velocities measured in [24] are on the lower end of the spectrum of velocities found in vortex tubes (due to the relatively low pressure ratio used in that

study), it is concluded that viscous dissipation is important for vortex tube flows and is therefore included in Eq. (4.2).

To model the Reynolds stress tensor that occurs when Reynolds- (or in this case Favre-) decomposing and averaging the equations is modeled employing the Boussinesq assumption, using the standard k-ε model to calculate the turbulent viscosity. Therefore, k and ε are calculated using the steady-state versions of Eqs. (2.47) and (2.51). In general, the standard k-ε model is known for poorly predicting swirling flows and does not have a realizability modification, meaning the normal components of the Reynolds stresses could become negative, which is physically not possible (cf. chapter 2.2). However, the standard k-ε model has been shown to predict the flow inside a vortex tube with sufficient accuracy, e.g. by Skye et al.[25], Dutta et al.[26] and Aljuwayhel et al.[20]. Within this work, the realizable k-ε was also used to simulate the case with air, presented in chapter 4.4. Interestingly, the temperature separation achieved with the realizable k-ε model was lower than that of the standard k-ε model, and also lower than experimental values. Therefore, as the standard k-ε showed better agreement with experimental measurements, it was used for all following simulations. For simulations where a gas is used as fluid, the density of the gas is computed via the ideal gas law, Eq. (2.52). For simulations where the fluid is a liquid, the density is modeled as being constant. In this case, the RANS equations are used instead of the here presented Favre-averaged equations. The molar mass, M, viscosity, μ, and thermal conductivity, λ, of the fluid are modeled as constant. The heat capacity, c_p, is modeled as constant for all fluids except for refrigerants, where c_p is given a linear temperature-dependency. All properties of fluids are obtained from the Reference Fluid Thermodynamic and Transport Properties Database (Refprop) of the National Institute of Standards and Technology (NIST).

The near-wall regions are modeled through scalable wall functions, which are standard wall functions with a correction for too fine near-wall mesh. If $y^+ \leq 11.225$, the solver sets $y^+ = 11.225$, to avoid using the log-law inside the viscous sub-layer[10].

4.3 Numerical Methods

The set of governing equations is solved using the coupled pressure-based solver of the commercial CFD code Ansys Fluent. Gradients are calculated with a cell-based least squares discretization scheme, the pressure equation is solved with a second order scheme, the turbulent transport equations with a second order upwind scheme. For all other transport equations a third-order MUSCL scheme is employed. The MUSCL scheme has been shown to yield superior accuracy over second-order schemes when the underlying flow regime involves rotation or a swirl[7]. Contrary to the similarly accurate QUICK scheme that is limited to the use of purely hexahedral cells, the MUSCL scheme can be used with any kind of mesh. As the mesh used within this study is made up of tetrahedral and prismatic cells (cf. chapter 4.4.2), the MUSCL scheme is chosen. The inlet and outlets are modeled as pressure-inlet and pressure-outlets, i.e. the value of total (for inlets) or static (for outlets) pressure and total temperature is set at the boundaries. All walls are modeled with the no-slip condition, and (except for simulations where heat transfer over the wall is simulated) as adiabatic. If available, results of a previous simulation loop are always used as initial guess. If not available, the hybrid initialization method[10] of Fluent is used, that is solving Laplace's equation to give an initial guess for the velocity field and the pressure field, and patches all other quantities with domain-average constant values. Explicit under-relaxation factors are kept around $0.1 - 0.2$ for all equations during the initial iterations until a converging trend is observed in the residuals of all equations. Then, the under-relaxation factors are increased up to values around $0.5 - 0.7$.

4.4 Flow Patterns in Air

4.4.1 Geometry

First, simulations using air as working fluid are conducted. The geometry and boundary conditions of Skye et al.[25] are used. The geometric specifications given in [25] are listed in Table 4.1. As no information on the geometric specifications of the hot outlet was available, it is assumed that there is some discrepancy between the model of [25] and the one used in this simulation. Geometric variations used in subsequent simulations are modeled based on the geometry given in Table 4.1.

symbol	description	value
L	working length of vortex tube	106 mm
D	tube diameter	11.4 mm
d_c	cold outlet diameter	3.1 mm
A_i	total inlet area	8.2 mm^2
h_i	inlet nozzle height	0.97 mm
w_i	inlet nozzle width	1.41 mm
n_i	number of inlet nozzles	6

Table 4.1: Geometric specifications of the vortex tube used in [25]

4.4.2 Mesh Independence

The geometric domain is discretized with a conformal mesh made up of tetrahedral cells. Near-wall regions are refined using prismatic cells to ensure $30 < y^+ < 300$ at wall nodes. This is needed as the standard k-ε turbulence model with wall functions is applied, where the first grid point needs to be located within the fully turbulent sub-layer, where the log-law of the wall is valid[7]. Figure 4.2 shows a contour plot of y^+-values at the walls. Naturally, as y^+ varies with the velocity, there are regions where $y^+ < 30$. As scalable wall functions are used, the effect of this too fine mesh is minimized. As the mesh consist of tetrahedral cells, the aspect ratio of the cells is near 1 for all cells. The average skewness is kept below 0.5, but maximum skewness values around 0.95 cannot be avoided at the transition from the tangential inlets to the vortex tube. In order to ensure the obtained solution is mesh-independent, simulations at a fixed cold fraction of $\gamma = 0.42$ are performed using meshes of different cell density. As the main quantities of interest are the hot and cold exit temperatures, T_h and T_c, these are used as criterion for judging mesh independence. As can be seen in Figure 4.3, mesh-independence is reached when exceeding approximately 1.5 million cells. Therefore, a mesh consisting of more than 1.5 million cells is used for all simulations. For simulations using a geometry of different size, the cell density is kept above that corresponding to mesh independence.
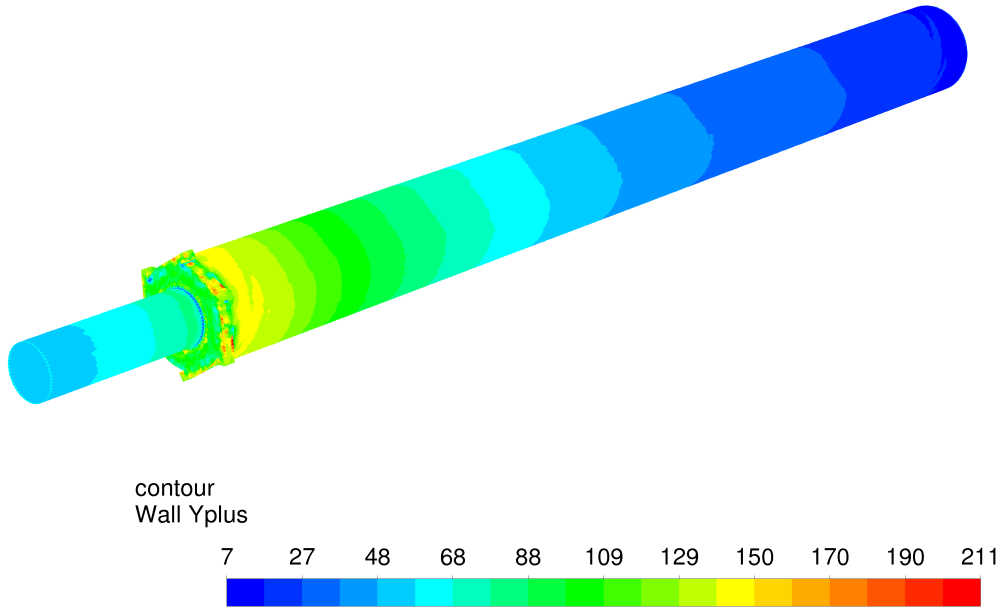
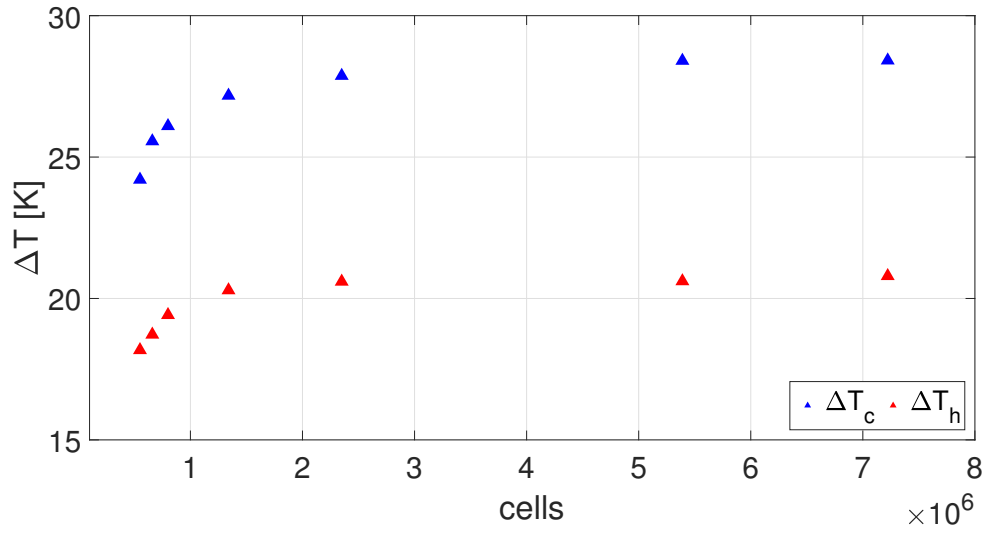Figure 4.2: Contour plot of y^+-values at wall nodes

Figure 4.3: Hot and cold temperature separation at $\gamma = 0.42$ with meshes of different cell count

4.4.3 Results

Figure 4.4 shows the mass-weighted average of total temperature separation, ΔT_h and ΔT_c, at the hot and cold outlet, respectively. Also, the experimental and numerical results of [25] are provided in Figure 4.4. It can be observed that T_h increases and T_c decreases with increasing cold fraction γ, and vice versa. Furthermore, at $\gamma = 0.5$, $\Delta T_h = \Delta T_c$. Also, the total temperature separation $\Delta T = \Delta T_h + \Delta T_c$ increases with increasing cold fraction γ. All these characteristics have been observed previously, e.g. by Hilsch[18], Skye et al.[25] and Bramo and Pourmahmoud[27]. Interestingly, the present simulation underpredicts the experimental cold separation ΔT_c in the same way as the numerical results from [25]. It is unclear whether the present underlying model and that of [25] both lack some physical feature. As there were considerable discrepancies between measured and calculated pressure values and a vague distinction between absolute and gauge pressures in [25], the possibility of a systematic error in the experimental measurements of [25] cannot be ruled out.

The left plot in Figure 4.5 shows the tangential (swirl) velocity profile at different axial locations
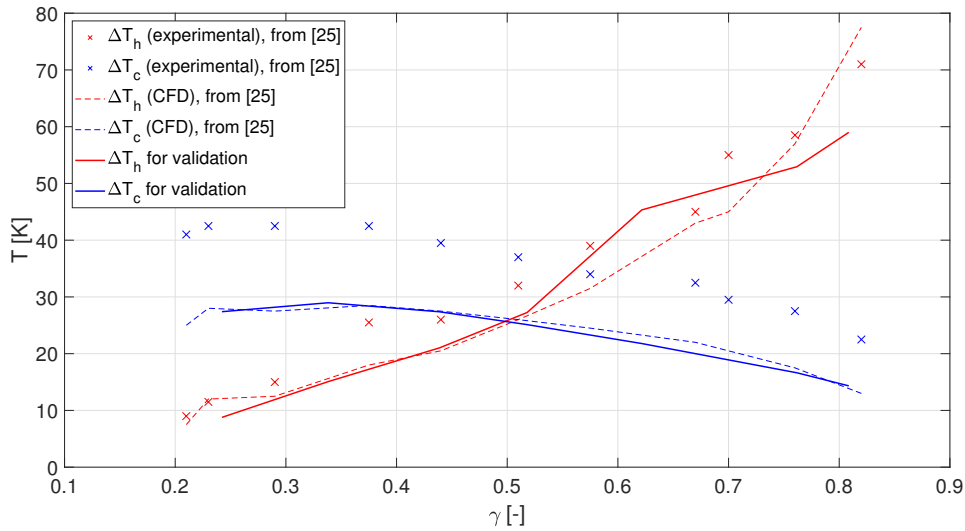

Figure 4.4: Separation of total temperature ΔT at different cold fractions γ plotted against the experimental and numerical results of [25]

of the vortex tube at $\gamma = 0.6$. The profiles qualitatively match those of Behera et al.[28], although in Figure 4.5 all velocities are zero at the wall due to the no-slip condition, in contrast to the plots of [28], where it is believed that the wall node values of the velocity have not been included in the plots. The right plot in Figure 4.5 shows the axial velocity profile at different axial locations of the vortex tube. Also, the profiles of Behera et al.[28] are qualitatively reproduced here. Interestingly, the region of negative axial velocities at the radial center of the vortex tube extends throughout the entire length. This suggests, that an increase in length could further enhance the performance in terms of temperature separation, as e.g. observed by Aljuwayhel et al.[20], the optimal length of a vortex tube is found where the cold recirculation area ends (i.e. where all axial velocities are positive). Furthermore, it can be observed, that the axial velocity of the hot stream, moving
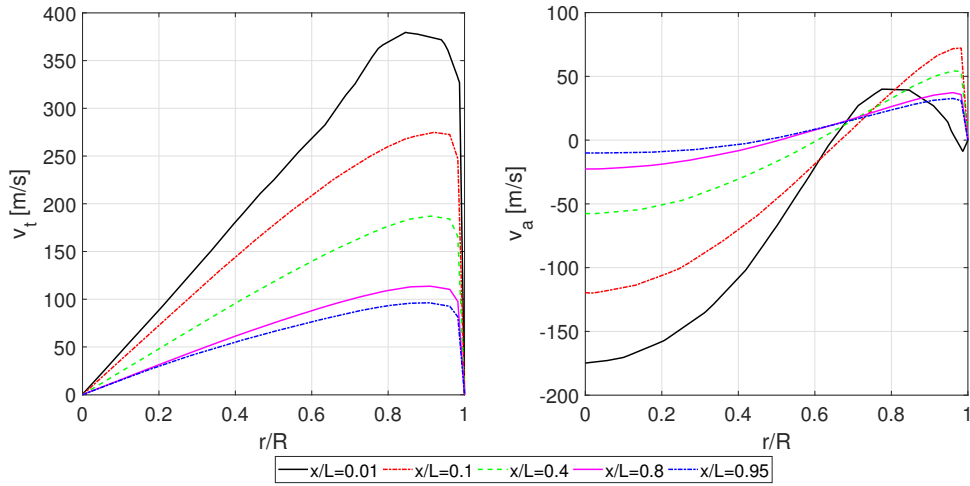
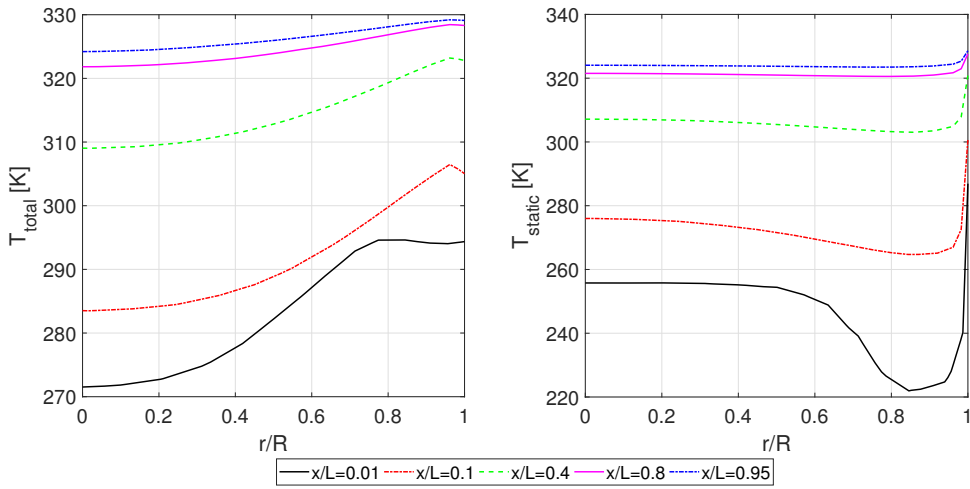Figure 4.5: Tangential (left) and axial (right) velocity profiles at different x/L-locations (air)

Figure 4.6: Total (left) and static (right) temperature profiles at different x/L-locations (air)

towards the hot end at the outer radius, is far smaller than that of the cold stream, at the inner radius. The tangential velocities behave vice versa, with the tangential velocities of the hot stream, at the outer radius, being far greater than that of the cold stream at the inner radius. Another interesting observation is, that a small portion of the fluid entering the vortex tube does not undergo the main flow pattern of travelling towards the hot end with great tangential velocity and then travelling back with great axial velocity close to the center. Instead, it seems to directly leave the vortex tube via the cold exit. This corresponds to the negative axial velocity close to $r/R = 1$ at $x/L = 0.01$. Therefore, this fraction of fluid is not undergoing the usual process of temperature separation but seems to be simply lowering its temperature through isenthalpic expansion. The profiles of total and static temperature at the same axial locations at $\gamma = 0.6$ are given in Figure 4.6, again matching those of [28]. Interestingly, at $x/L = 0.95$, there still exists a small radial gradient in total temperature, which suggests that a further increase in tube length could further enhance temperature separation and might be linked to the observations made in the plots of axial velocity (Figure 4.5), where the recirculation region is not yet at its end before the hot end of the vortex tube, manifesting itself in the negative axial velocity at $r/R = 0$ at the hot end. Another interesting characteristic is, that, although there exists a clear axial gradient in static temperature, the radial gradient in static temperature is even negative for most locations. Therefore, most of the radial increase in total temperature is due to the high tangential velocities.

Figure 4.7 and Figure 4.8 show the distribution of total temperature and density throughout the
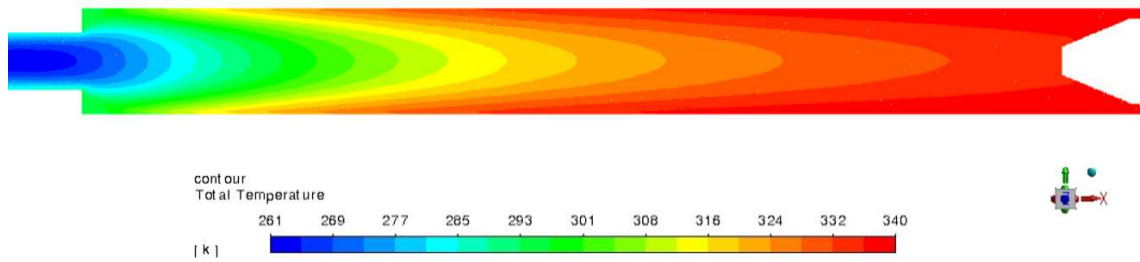

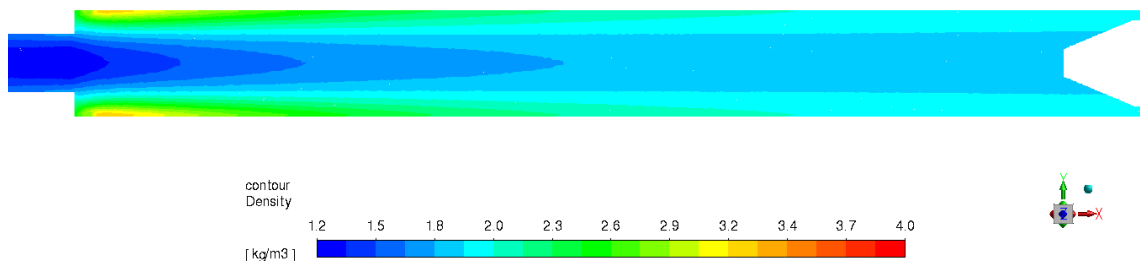Figure 4.7: Contour plot of total temperature throughout the vortex tube ($\gamma = 0.6$, air)

Figure 4.8: Contour plot of density throughout the vortex tube ($\gamma = 0.6$, air)

vortex tube, respectively. In Figure 4.8, near the hot end, two distinct zones of different density can be seen. This difference in density is most likely not due to a difference in static temperature, as there is almost no radial gradient in static temperature present at the hot end (cf. Figure 4.6), but most likely due to a gradient in pressure, which stems from the static pressure at the hot exit being slightly higher than that at the cold exit.

4.5 Flow Patterns in Water

A simulation of the same vortex tube geometry as in chapter 4.4, with water as working fluid is conducted. The same mathematical model and solver settings are used as in the case with air, except that the water is modeled as incompressible fluid, with a constant density. The inlet pressure is set to 50 MPa, resulting in an overall temperature separation of around 10 K, where both the hot and cold exit temperatures are found to be above the inlet temperature. This is identical to the experimental results of Balmer [22]. No detailed information on boundary conditions or geometric specifications used in the experiments of [22] was available, but the commercial vortex tube used by Balmer[22] was similar in size to that used by Skye et al.[25] and in the present simulation. Figure 4.9 shows the tangential and axial velocity profiles and Figure 4.10 shows the total and static temperature profiles of a simulation at $\gamma = 0.54$. The tangential velocity profiles of water exhibit a similar pattern to those of air (Figure 4.5). The axial velocity profiles differ, as, in contrast to the case with air, the maximum axial velocity is located at $x/L = 0.1$, in contrast to $x/L = 0.01$ in the case with air. Therefore, the cold stream at the inner radius seems to be decelerating before leaving through the cold exit. Like in the case with air, the region of negative axial velocity extends throughout the entire vortex tube, suggesting a possible enhancement in temperature separation could be achieved by increasing the tube length. Additionally, the axial velocity close to the outer radius of the vortex tube features a sharper peak. A fundamental difference between the profiles of axial velocity of air and of water is that with water, there is no region of negative axial velocity at the cold end near the outer radius around $r/R = 1$. Therefore, no fraction of the fluid leaves the vortex tube directly from the nozzles through the cold end. The static temperature profiles of the water and air case show a similar behaviour, but the total temperature profiles of water exhibit less change in temperature over the radius than that of air. Also, the total temperature close to the cold end $(x/L = 0.01)$ has its maximum at $r/R = 0.8$ and then decreases towards the outer radius, which was not observed with air. One interesting observation made during the present simulation is, that when excluding the viscous dissipation term, Φ, from the energy equation, Eq. (4.2), no temperature separation occurs throughout the entire vortex tube. Therefore, the only underlying physical process needed to mathematically model and reproduce the experiments of [22] is viscous dissipation. When excluding the same term from the energy equation in the case of air a smaller but still significant temperature separation is observable. This leads to the question whether the Ranque-Hilsch effect is the reason for the observations made by Balmer[22].

Regardless of the physical processes behind temperature separation, it can be concluded that the temperature separations produced by a vortex tube when operated with a liquid are too small and require a too high pressure difference to be exploited in heat pump applications.
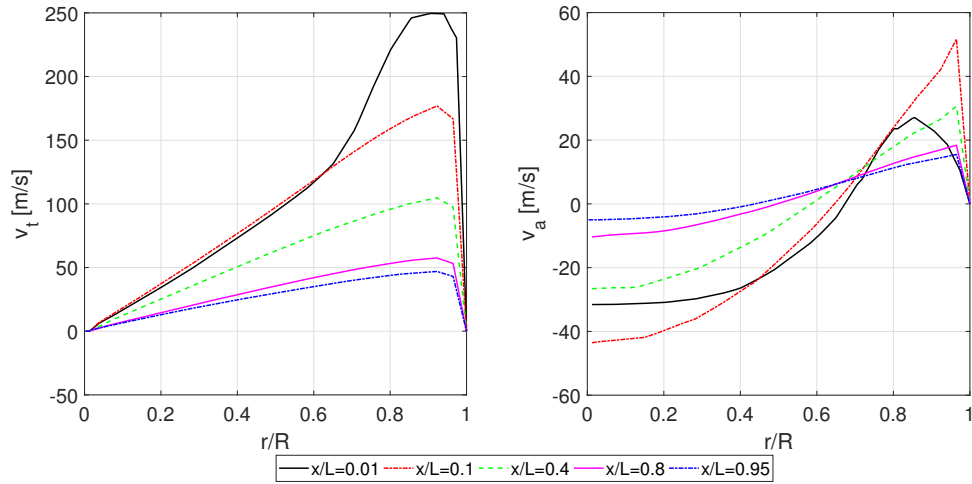
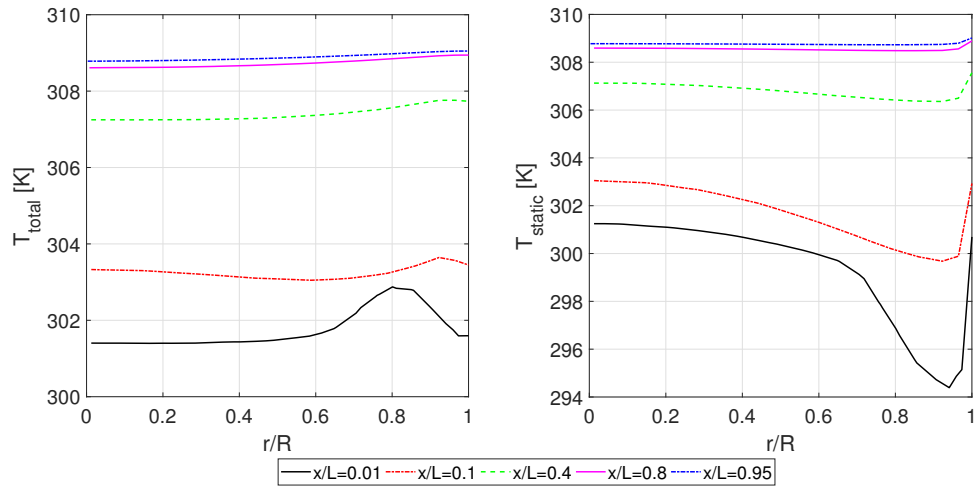Figure 4.9: Tangential (left) and axial (right) velocity profiles at different x/L-locations (water)

Figure 4.10: Total (left) and static (right) temperature profiles at different x/L-locations (water)

4.6 Flow Patterns in the Refrigerant

The same geometry as in chapters 4.4 and 4.5 is again used for simulations where the working fluid is a gaseous refrigerant. Figure 4.11 again shows the tangential and axial velocity profiles obtained with the refrigerant R1336MZZ(Z) as working fluid. Figure 4.12 shows the temperature profiles of the same working fluid. It is interesting that not only the magnitude of tangential velocities is significantly lower than that of air (Figure 4.5), but also the radial gradient of tangential velocities is smaller. Considering the plots of axial velocities, it can be seen that there is no negative axial velocity at the outer radius ($r/R = 1$) close to the cold exit. Therefore, the fraction of fluid going from the nozzles directly to the cold exit and potentially lowering its temperature only through isenthalpic expansion, which was observed with air but not with water, is not present with R1336MZZ(Z) as refrigerant. This is an unexpected observation, as the refrigerant is in a fully gaseous state. Also, in contrast to both the patterns of air and water, the axial velocity near the cold exit ($x/L = 0.01$) stays relatively higher towards the outer radius ($r/R = 1$). Concerning the patterns of temperature in Figure 4.12, there is a clear radial separation of total temperature that is not obtained with an incompressible working fluid (Figure 4.10). It is observed that the radial separation of total temperature closest to the inlet (at $x/L = 0.01$) is relatively larger than that of air. Also, the total temperature at $x/L = 0.01$ is partly higher than that closer to the hot exit at $x/L = 0.1$, which is not observed for air or water. The maximum in tangential velocity, and correspondingly in total temperature, at the outer radius close to the cold exit ($x/L = 0.01$) is extending further towards the inner radius than with air or water.

As the assumption of adiabatic walls does not hold in reality, the influence of heat transfer over the

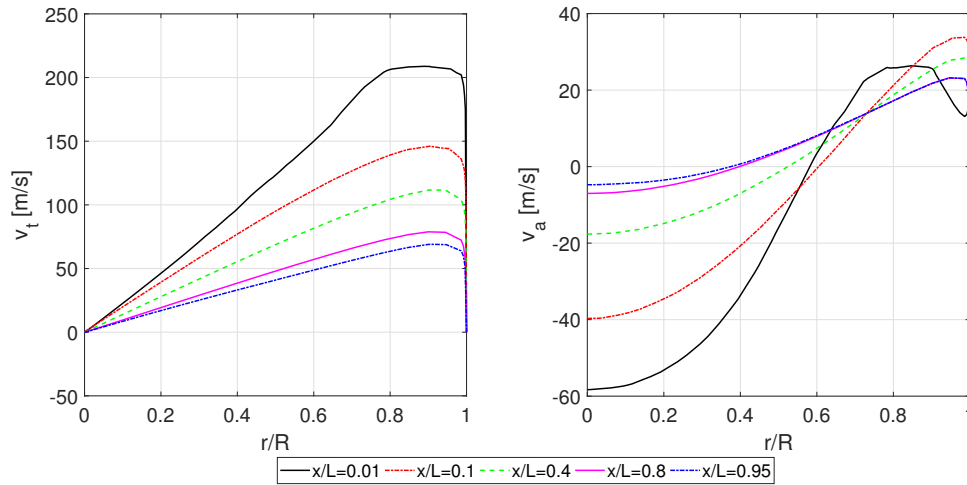Figure 4.11: Tangential (left) and axial (right) velocity profiles at different x/L-locations (R1336MZZ(Z))

tube wall is also investigated. For these simulations, convective heat transfer on the outside of the wall is included via a heat transfer coefficient α, and heat conduction over the wall is calculated assuming the wall to be made out of 2 mm aluminum, which might not be a realistic assumption,
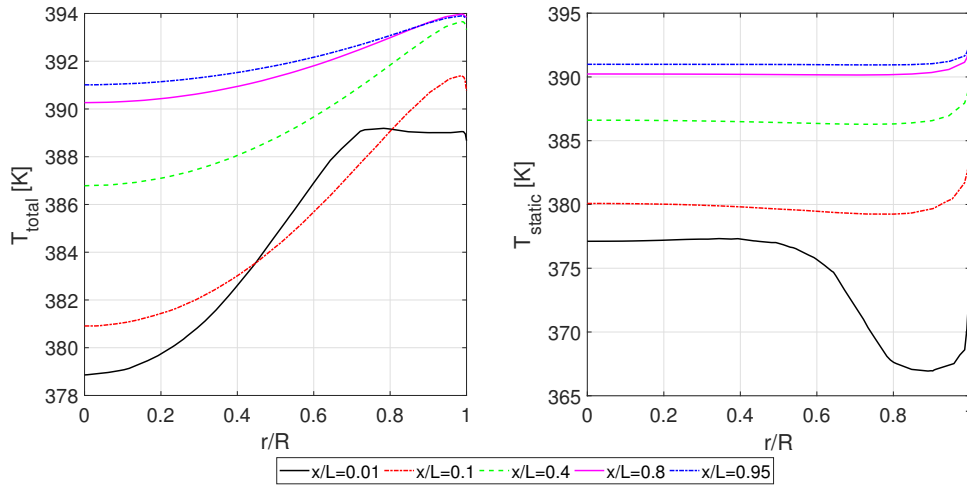
Figure 4.12: Total (left) and static (right) temperature profiles at different x/L-locations (R1336MZZ(Z))

but the aim is merely to investigate the influence of non-adiabatic walls on the flow characteristics inside a vortex tube, not to make quantitative predictions. The results of two simulations with different heat transfer coefficients, where $\alpha_1 < \alpha_2$, are presented here. Figure 4.13 shows the total and static temperature profiles, Figure 4.14 shows the tangential and axial velocity profiles and Figure 4.15 shows the total and static pressure profiles. As expected the inclusion of heat transfer over the tube wall has a great influence on the temperature distribution inside the vortex tube, but the flow patterns in terms of velocity and pressure are not significantly influenced. Therefore, the coupling between flow patterns in terms of velocity and pressure and the temperature separation is assumed to be one-way, as the flow patterns in terms of velocity and pressure have a great influence on the temperature separation, but not vice versa. Another interesting observation is, that the difference in both total and static temperature (Figure 4.13) for increasing heat flux at the wall is greater at the center of the tube than at the outer radius close to the wall, although the heat flux is occurring over the wall at $r/R = 1$. Also, the difference increases over the tube length with x/L, which is logical, as while the fluid travels towards the hot outlet in a swirling pattern close to the wall, the further downstream, the greater the total amount of heat lost over the wall. As, under real conditions, the walls of a vortex tube are not adiabatic, proper insulation is essential to exploit the full potential of the Ranque-Hilsch effect. Another option is to use the outside of the vortex tube wall for heating a colder stream inside the heat pump, and therefore utilize the radial temperature distribution inside the vortex tube. However, this would come at the cost of less temperature difference between the fluid at the hot and cold outlet.

Figure 4.13: Total (left) and static (right) temperature profiles at different x/L-locations (R1336MZZ(Z)) with convective heatflux, $\alpha_1 < \alpha_2$
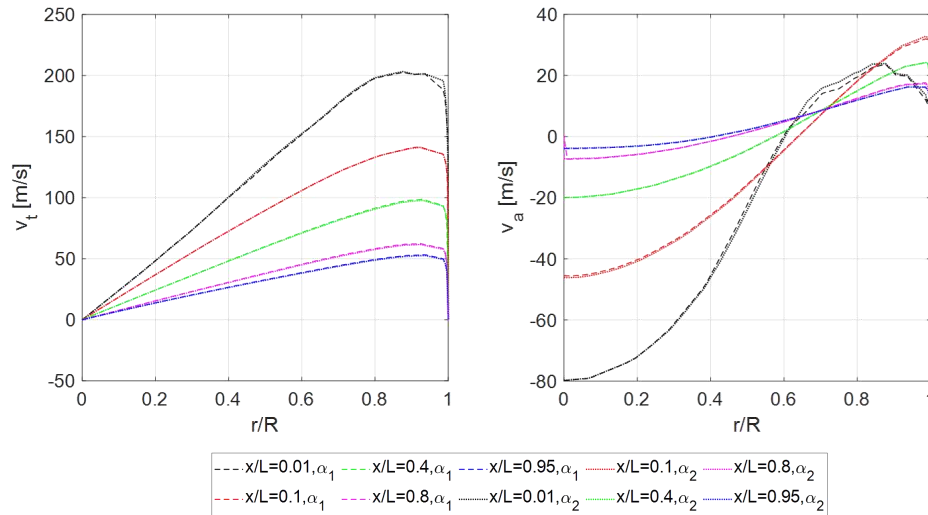
Figure 4.14: Tangential (left) and axial (right) velocity profiles at different x/L-locations (R1336MZZ(Z)) with convective heatflux, $\alpha_1 < \alpha_2$
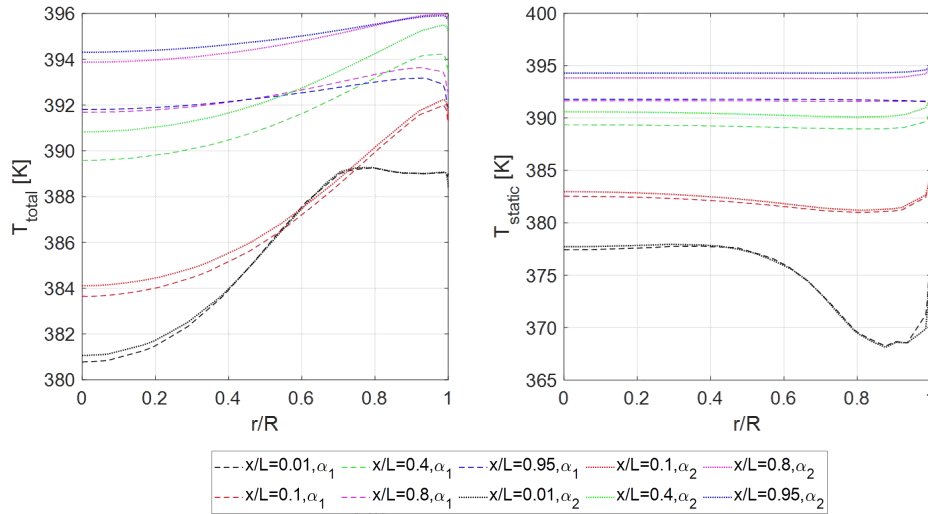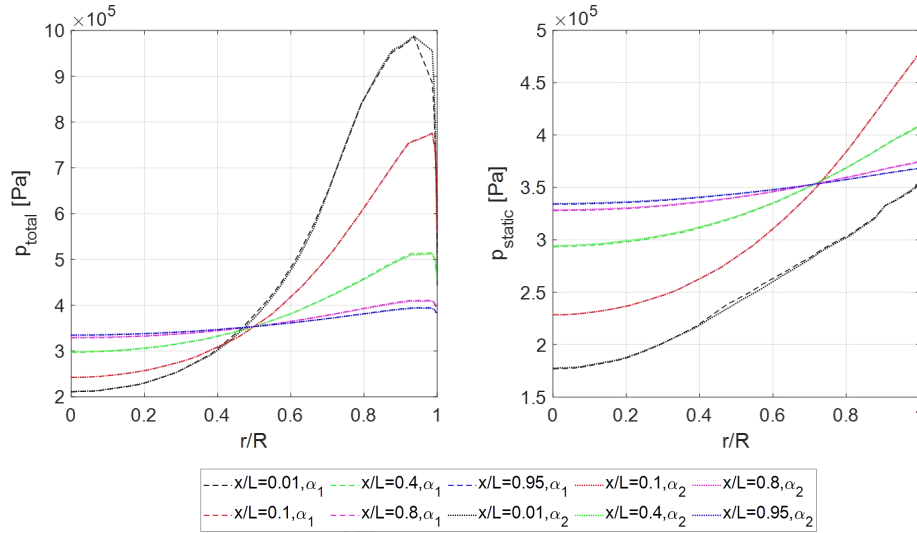
Figure 4.15: Total (left) and static (right) pressure profiles at different x/L-locations (R1336MZZ(Z)) with convective heatflux, $\alpha_1 < \alpha_2$

4.7 Parameter Study: R1336MZZ(Z)

Figure 4.16 shows the results of simulations using two different vortex tube geometries in terms of length-to-diameter ratio (L/D). The working fluid is the synthetic refrigerant R1336MZZ(Z). The inlet pressure and cold outlet pressure is, for all simulations, set at $p_i = 10$ bar and $p_{o,c} = 1.978$ bar, respectively, the hot outlet pressure, $p_{o,h}$, is varied to adjust the cold fraction. It is notable that a change in L/D does not show a significant change in terms of temperature separation. As shown above, the recirculation region extends throughout the entire vortex tube (as seen in the plots of axial velocity), which suggests that an increase in tube length could further enhance temperature separation. Therefore the outcome of this parameter study is unexpected. While the pressure ratio $\Pi_p = p_i/p_{o,c}$ is comparable to that used when obtaining the results with air as a working fluid presented in Figure 4.4, the temperature separation with R1336MZZ(Z) is significantly lower.

The results of the simulations provided in Figure 4.16 are used in chapter 4.9 as a model of the vortex tube within one-dimensional heat pump cycle simulations.

Figure 4.16: Separation of total temperature ΔT at different cold fractions γ for two different vortex tube geometries (R1336MZZ(Z))

4.8 Cycle Layout

One example for integrating a vortex tube as expansion device in a heat pump cycle is the Maurer model[29, 30]. A schematic layout of such a cycle can be seen in Figure 4.17. This proposed cycle features a vortex tube with three outlets, where the additional outlet is supposed to carry liquid that is separated and collected during the expansion process. It is noted that no evidence of a vortex t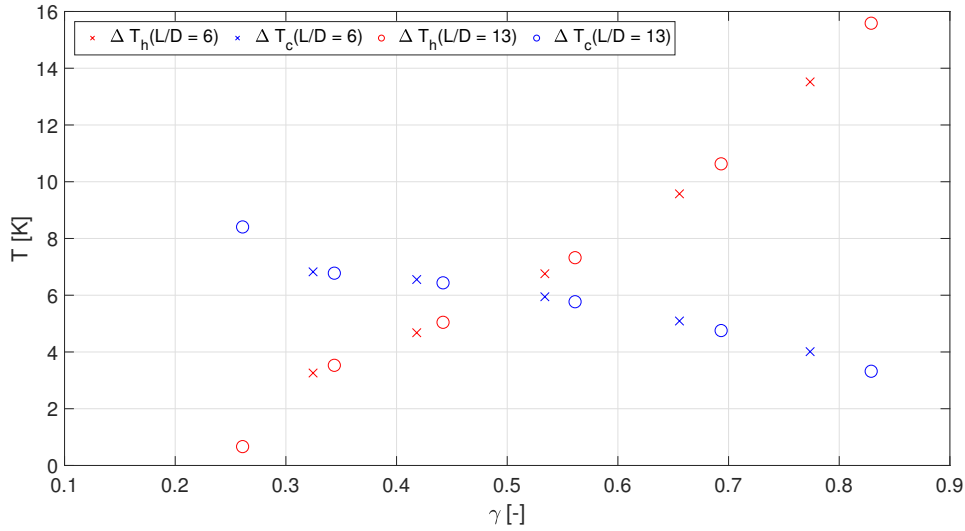ube built and tested in that way could be found, and this is a purely hypothetical design. The idea of this cycle is, that the fully condensed (and possibly subcooled) refrigerant at state **3** is expanded inside a vortex tube, yielding a superheated state at the hot outlet (**4c**) where the thus provided heat can be utilized in an additional heat exchanger. The streams exiting through the cold outlets, carrying fully evaporated gaseous fluid (**4a**) and separated, fully condensed liquid (**4b**) are merged and fed to the evaporator. However, it is unclear whether the proposed modified vortex tube for the expansion of a liquid can be technically realized. According to Zhu[31] and Mohiuddin and Elbel[32], temperature separation in a vortex tube disappears when two-phase flow is present. Taking into account the findings of Balmer[22], Collins and Lovelace[23] , Mohiuddin and Elbel[32] and Zhu[31], it seems to be unreasonable to design a heat pump cycle featuring the expansion of fully condensed refrigerant into two phase state inside a vortex tube.

To fully exploit the potential of vortex tube temperature separation, a cycle proposed by Mohiuddin and Elbel[32], and further investigated by Zhu[31], can be used to ensure the fluid inside the vortex tube is always in a single-phase, gaseous state. The layout and theoretical log(p)-H diagram of such a cycle can be seen in Figure 4.18. From state **1** to state **3**, this cycle is identical to a conventional heat pump cycle. Then, the fully condensed (or subcooled) refrigerant at state **3** is expanded to an intermediate pressure level, p_{int}, which is between that of condenser and evaporator, inside a throttle valve. The thus developed two-phase fluid is then separated into liquid (**5a**) and vapor (**5b**), with the vapor being expanded to evaporator pressure level in a conventional vortex tube.

The hot exit gas (**6c**) can be utilized for further heating applications, given that demand for heat at the corresponding temperature level exists. The liquid (**5a**) is then expanded in a throttle valve (**6a** to **7a**) and evaporated (**8a**). As the hot exit pressure of a vortex tube lies slightly above the cold exit pressure, further expansion (**7c** to **8c**) is needed. When using a vortex tube as expansion
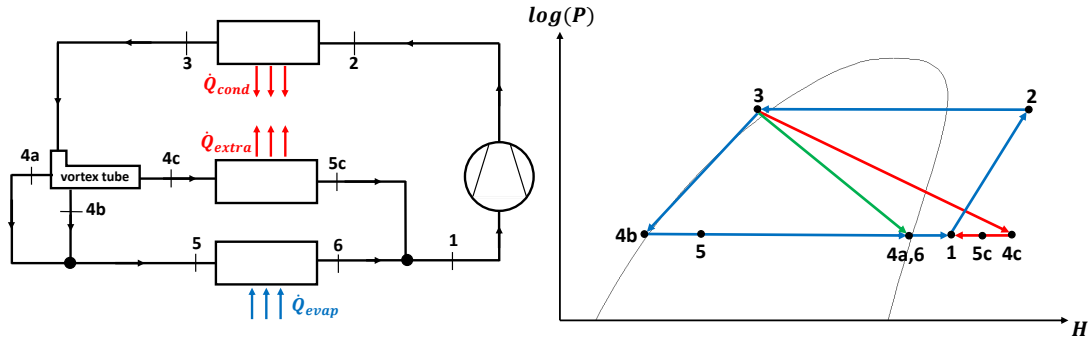
Figure 4.17: Maurer model: Schematic cycle layout and theoretical log(p)-H diagram (based on [30])
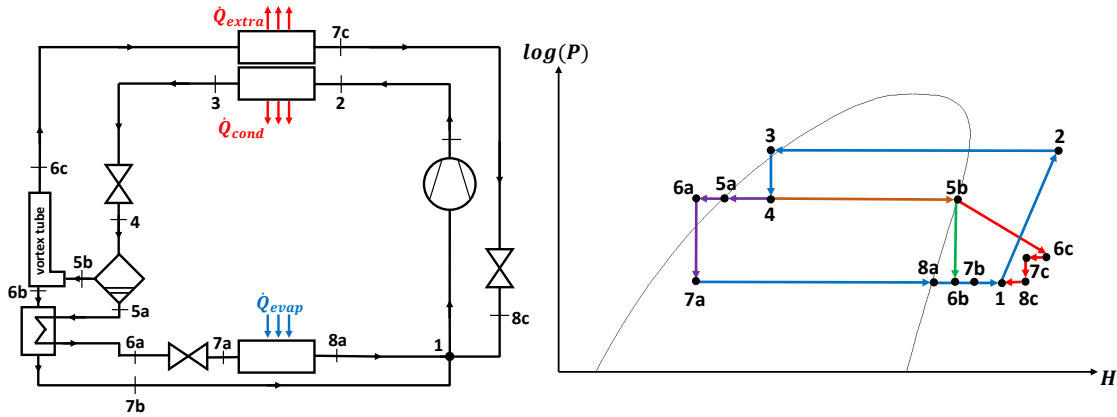
Figure 4.18: Intermediate expansion cycle: Schematic cycle layout and theoretical log(p)-H diagram (based on [32])

device in an intermediate expansion cycle (shown in Figure 4.18), an additional pressure level, p_{int}, between condenser pressure and evaporator pressure is needed, in contrast to a conventional heat pump cycle. It is not immediately obvious where the optimum value of p_{int} lies, as with increasing p_{int} the temperature separation ΔT inside the vortex tube increases, but at the same time the

fraction of fluid expanded through the vortex tube decreases.

$$p_{int} \uparrow \Rightarrow \ \Delta T \uparrow \tag{4.6}$$

$$p_{int} \uparrow \Rightarrow \ \dot{m}_{VT} \downarrow \tag{4.7}$$

If $p_{int} = p_{condenser}$, there is no gas phase to be separated and expanded through the vortex tube, and if $p_{int} = p_{evaporator}$, the maximum possible amount of gas phase is going through the vortex tube, but $\Delta p = 0$ over the vortex tube. Therefore, an optimum value of p_{int} must exist. It makes therefore sense to maximize some product of temperature and mass flow rate. An ideal candidate for maximisation seems to be the enthalpy difference (to be precise, the difference of enthalpy flow rate, as the specific enthalpy difference is multiplied by the mass flow rate).

$$\Delta \dot{H} = c_p \dot{m} \Delta T \ \rightarrow \ \max \tag{4.8}$$

The temperature separation inside the vortex tube, ΔT, is generally unknown. Performing CFD simulations for different pressure levels, mass flow rates and working fluids comes at high computational cost. However, only an estimate of the relative change of ΔT with respect to pressure is needed, to determine the maximum of Eq. (4.8), and not an absolute value of ΔT. Therefore, the analytical formula derived by Ahlborn and Gordon[19] can be used. It reads

$$\Pi_T = \frac{T_h}{T_c} \approx 1 + \frac{(\kappa - 1)\zeta(\gamma + 1)}{\kappa} \tag{4.9}$$

where κ is the heat capacity ratio, γ is the cold fraction and

$$\zeta \approx \frac{p_i - p_c}{p_i + 2p_c} \tag{4.10}$$

Obviously, the value of T_h/T_c given by Eq. (4.9) is not necessarily correct, but its change with respect to the pressure ratio p_i/p_c is assumed to show a similar behaviour as that of a real vortex tube. Expansion from **3** to **4**, is assumed to be isenthalpic. The corresponding vapor quality, χ, is then used to determine the mass flow rate, $\dot{m}$, that enters the vortex tube. The fact that at a cold fraction $\gamma = 0.5$, $\Delta T_h = \Delta T_c$ is used to obtain

$$T_h - T_i = T_i - T_c \tag{4.11}$$

$$T_h = \frac{2T_i}{1 + 1/\Pi_T} \tag{4.12}$$

For every intermediate pressure level p_i, corresponding values of c_p and vapor quality χ (and thus resulting mass flow rate $\dot{m}$) can be obtained for the respective fluid. The temperature ratio Π_T is obtained from Eq. (4.9) and then, $\Delta T = T_h - T_c$ is obtained from Eq. 4.12). These values are then used to calculate the enthalpy difference $\Delta \dot{H}$ according to Eq. (4.8). In Figure 4.19 $\Delta \dot{H}$ is plotted for two cases. Case A is using the refrigerant R290, with condenser and evaporator pressure levels being [$p_{cond.} = 19.5$ bar, $p_{evap.} = 3.808$ bar]. Case B is using the refrigerant R600 with condenser and evaporator pressure levels being [$p_{cond.} = 26.63$ bar, $p_{evap.} = 6.864$ bar]. While for case A, the optimum of p_{int} is found approximately at the mean of condenser and evaporator pressure, this is not the case for case B.

When it comes to high temperature applications, such as steam generation, a heat boost cycle,
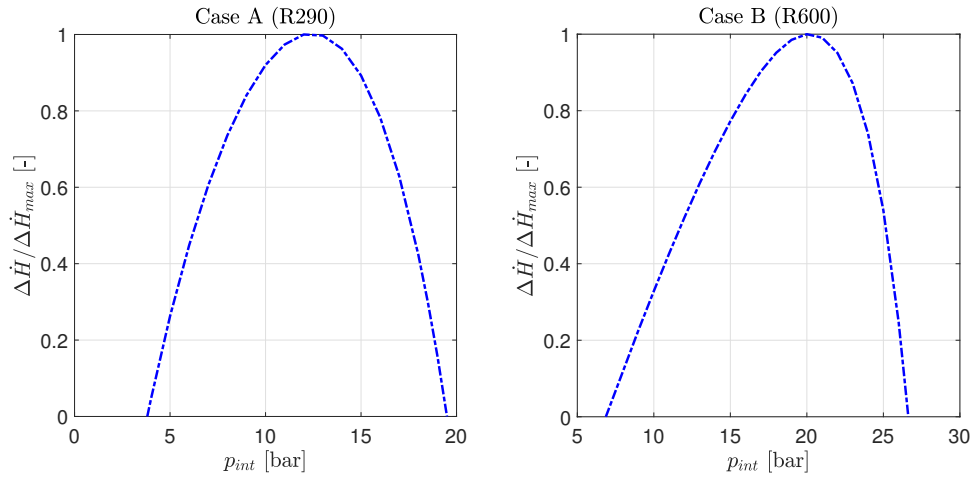
Figure 4.19: Normalized enthalpy flow rate difference, cf. Eq.(4.8), over intermediate pressure p_{int} for two cases

shown in Figure 4.20, can be used. Such a cycle was previously proposed by Mohiuddin and Elbel[32]. In contrast to a classical heat pump cycle, the fully condensed fluid is pumped to a high pressure, where waste heat is used to evaporate the fluid. Then, the fully evaporated fluid is expanded through a vortex tube, using the hot side for steam generation. The main disadvantage is that the amount of hot exit gas available for steam generation decreases with increasing hot exit temperature. Therefore, the higher the needed temperature lift, the less refrigerant mass flow can be utilized for heating purposes. Additionally, the compression process takes place in the liquid state, making this design fundamentally different from a heat pump. Another problem arises with the fact, that the temperature separation achieved in vortex tubes with refrigerants as working fluids is, as mentioned above, found to be significantly lower than that of common operating fluids such as air. Therefore, the difference in temperature levels of the waste heat source and the sink is limited, again reducing applicability of this layout. For these reasons, the heat boost cycle is not further investigated in this study.

43
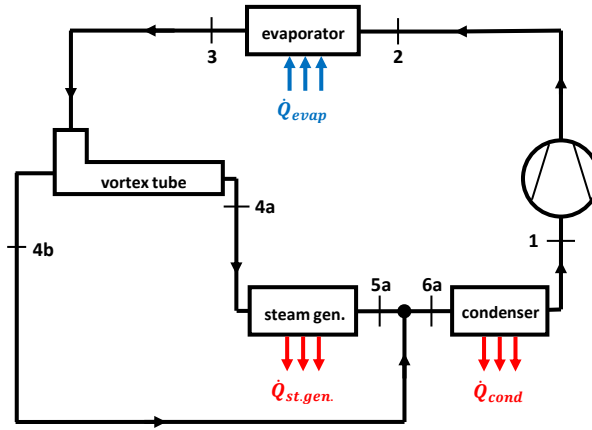
Figure 4.20: Heat boost cycle for steam generation with vortex tube as expansion device

4.9 One-Dimensional Heat Pump Cycle Simulation

To analyse the effects of vortex tube expansion in terms of COP-improvement, the intermediate expansion cycle (Figure 4.18) was modeled one-dimensionally using the software DYMOLA. The vortex tube was modeled as a lookup-table, where for a given refrigerant, the results of CFD simulations were provided in the form $[p_{in}, p_c, p_h, T_{in}, \gamma, T_c, T_h]$, with pressure levels and inlet temperature being set by the rest of the simulation, and thus yielding corresponding values for cold fraction and outlet temperatures for use in the one-dimensional simulation. The simulation was one-dimensional as it was transiently simulating different operating points (therefore time being the one dimension). However, transient effects of the vortex tube characteristics were not investigated in the CFD simulations and therefore the vortex tube characteristics were simply obtained from linear interpolation in the look-up table.

The application of an intermediate expansion heat pump cycle requires a sufficiently high pressure difference between evaporator and condenser in order for the vapor fraction separated after intermediate expansion being high enough to yield a reasonable amount of working fluid for vortex tube expansion. Therefore this cycle seems to be especially interesting for high temperature applications such as steam generation. One case where an intermediate expansion heat pump cycle was shown to significantly outperform a conventional heat pump cycle was found. In this simulation, a waste heat source of water at 70° C was utilized to supply heat for steam generation at 160° C using the synthetic refrigerant R1336MZZ(Z). The COP of the intermediate expansion cycle increased by 19% to 1.67 over that of the conventional cycle with a COP of 1.41. The additional heat provided at the hot end of the vortex tube was found not to be sufficiently high for utilization and was therefore not included in the COP calculation. The log(P)-h diagram of both the intermediate expansion and conventional cycle are given in Figure 4.21. The state points **1-4** in the left diagram of Figure 4.21 correspond to the state points of a conventional heat pump cycle (cf. Figure 1.1): vapor compression from **1** to **2**, condensation from **2** to **3**, isenthalpic expansion from **3** to **4** and evaporation from **4** to **1**. The state point numbers in the right diagram of Figure 4.21 correspond

to those of an intermediate expansion cycle given in Figure 4.18. As the heat provided at the hot outlet of the vortex tube was not used for COP calculations due to a lack of use for heat at this temperature, the COP improvement stems mainly from the increased heat being received in the evaporator (state **7a** to **8a**). However, this is an advantage which can only be used if the heat source used for evaporation is available to that extent. As the advantage of vortex tube expansion seems to be mainly in increasing evaporator heat flow, this configuration might be more interesting for refrigeration applications. Additionally, it shall be noted that the temperature separation achieved through vortex tube expansion of refrigerants at heat pump pressure levels was found to be low compared to that achieved with air or CO_2. The refrigerants tested were R290 (propane), R600 (butane), R1234ZE and R1336MZZ(Z). Most combinations of refrigerant and operating conditions tested did not show a significant improvement over a standard heat pump. The results of these simulations are not presented in detail here, as the focus of this work lies on the numerical analysis of the fluid flow characteristics within the vortex tube, and the one-dimensional analysis presented in this chapter should merely give context and elaborate the objective of the CFD simulations.
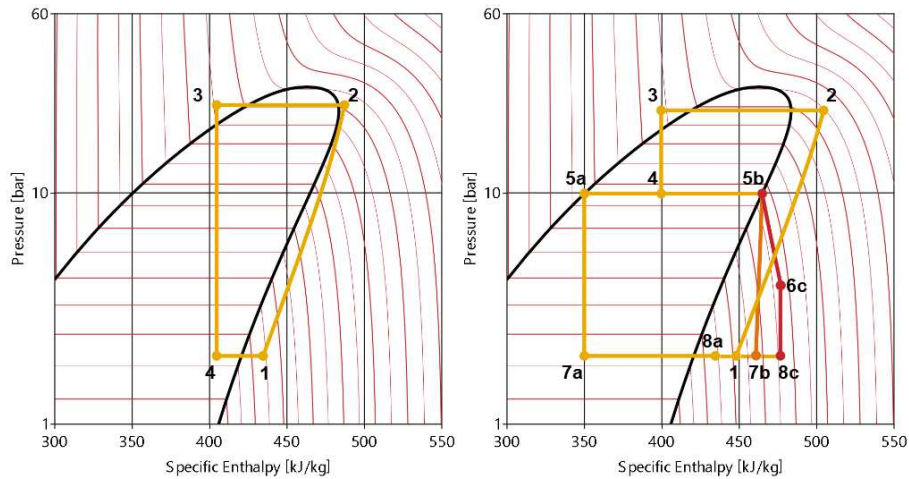
Figure 4.21: Log(p)-H diagrams of conventional heat pump cycle (left) and intermediate expansion cycle (right) for an industrial steam generation case using R1336MZZ(Z)

4.10 Conclusion

- The operation of a vortex tube with the working fluid being in liquid or two-phase state is not favorable. The Ranque-Hilsch effect, i.e. temperature separation, cannot be obtained with two-phase fluids if the vapor quality is not sufficiently high. Temperature separation can in principle be obtained for a liquid working fluid, but the required pressure difference makes this process irrelevant for technical exploitation.

- The numerical analysis conducted in this work suggests that the driving mechanism behind liquid temperature separation might not be what is commonly known as the Ranque-Hilsch effect, with different physical processes being responsible for the temperature separation of liquids and gases, respectively.

- The results of the conducted CFD simulations show that the temperature separation obtained with refrigerants is significantly lower than that of air.

- Using the results of three-dimensional CFD simulations of a vortex tube at different operating conditions, its characteristics were integrated in the cycle simulation of a modified heat pump cycle. One case of an industrial high-temperature heat pump for steam generation where a heat pump cycle featuring vortex tube expansion outperforms a conventional heat pump was presented. The COP was predicted to increase by 19%.

- The approach that was used in this study - CFD simulation of the vortex tube followed by a one-dimensional simulation of the entire heat pump cycle - can be used to further evaluate different combinations of refrigerants, evaporator and condenser pressure levels and intermediate pressure levels, as well as different heat pump configurations. In this way, promising cases for a detailed experimental investigations can be identified.

5 Ejector

In chapter 5.1, an overview on the working principle of an ejector, different types and some numerical studies of ejectors is provided. The underlying flow regime of the ejector to be simulated is very complex, involving a flashing process, where a liquid is expanded and therefore evaporates and accelerates to supersonic speed, entraining and mixing with a secondary fluid. To be able to simulate the flow processes inside the ejector without the need for a highly complex multiphase model that needs careful fine-tuning using a broad range of experimental measurements, a simple homogeneous equilibrium model is derived and implemented. Although the model neglects some important physical features of the flow, such as non-equilibrium thermodynamics, knowing the limitations, still some interesting investigations can be made, within reasonable amounts of computational time. This model is derived and presented in detail in chapter 5.2. To ensure the general capability of the model to correctly simulate transonic flows, a benchmark case is simulated, which is presented in chapter 5.3. In chapter 5.4, the numerical methods used to solve the underlying equations are outlined. As numerical methods for such high-speed flows are quite unstable, a solution strategy to obtain a solution is developed and outlined in detail in chapter 5.5. The model is then used to simulate two different ejector geometries. The first geometry was used within a high temperature heat pump and experimental measurements exist. The second one is an arbitrary variation in geometry from the first one. The two geometries, simulated using the same boundary conditions, are then compared. These results are presented in chapter 5.6.

5.1 Theoretical Background

An ejector is an expansion and mixing device with two inlets and one outlet. A schematic drawing of an ejector is given in Figure 5.1. A high-pressure fluid enters through the primary inlet, is accelerated and entrains a low-pressure fluid entering through the secondary inlet. After a mixing process and static pressure recovery in a diffuser, the fluid leaves the ejector at a pressure that lies between the two inlet pressures. An ejector can be categorized by three criteria, i.e. the nozzle position, the nozzle design and the number of phases present. The nozzle can be located either inside the suction chamber, yielding a constant pressure mixing ejector (CPM), or inside the mixing zone of constant area, yielding a constant area mixing ejector (CAM). It shall be noted that CPM ejectors have been shown to outperform CAM ejectors[33]. Regarding the nozzle design, ejectors featuring a convergent nozzle are categorized as subsonic ejectors, as the flow velocity inside the ejector cannot exceed the speed of sound. Ejectors that feature a convergent-divergent nozzle are categorized as supersonic ejectors, as this design allows for supersonic conditions to be achieved[34, 35]. Applying this classification framework, the schematic ejector depicted in Figure 5.1 is a supersonic CPM ejector. Regarding the number of phases present throughout the ejector, several possible configurations exist. If the fluid at both inlets and the outlet is in a liquid state, the ejector is classified as liquid jet ejector. Analogously, an ejector where the fluid at both inlets and at the outlet is in a vapor state is called vapor jet ejector. An ejector where vapor is entering through the primary inlet, and both the secondary inlet flow and the outlet flow are liquid is called condensing ejector. Lastly, an ejector with liquid entering through the primary inlet, vapor entering through the secondary inlet and two-phase flow exiting through the outlet is called two-phase ejector, which is also the type of ejector to be used within a heat pump. When replacing the expansion valve of a heat pump cycle with an ejector, the expansion process is used to convert the potential energy of the high pressure fluid into kinetic energy as it is accelerated. This kinetic energy

47
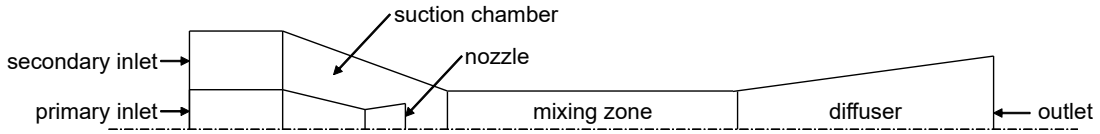
Figure 5.1: Schematic drawing of an ejector

is then used to lift the pressure level of the fluid stream coming from the evaporator. Therefore compressor work is saved and thus the COP of the cycle is increased by reducing the amount of electrical energy needed[36]. A way to integrate an ejector into a heat pump cycle is shown in Figure 5.2. As can be seen, the vapor entering the compressor from the separator at state **1** lies at a higher pressure level than that of the evaporator, therefore reducing the necessary compressor work. The low-pressure vapor leaving the evaporator (**10**) enters the ejector through the secondary inlet (**5**) and is entrained by the high-pressure stream coming from the condenser and entering the ejector through the primary nozzle (**4**). After pressure recovery inside the diffuser, the mixed two-phase refrigerant leaves the ejector at a higher pressure level (**7**) and is separated into vapor (**1**) and liquid (**8**) phases.
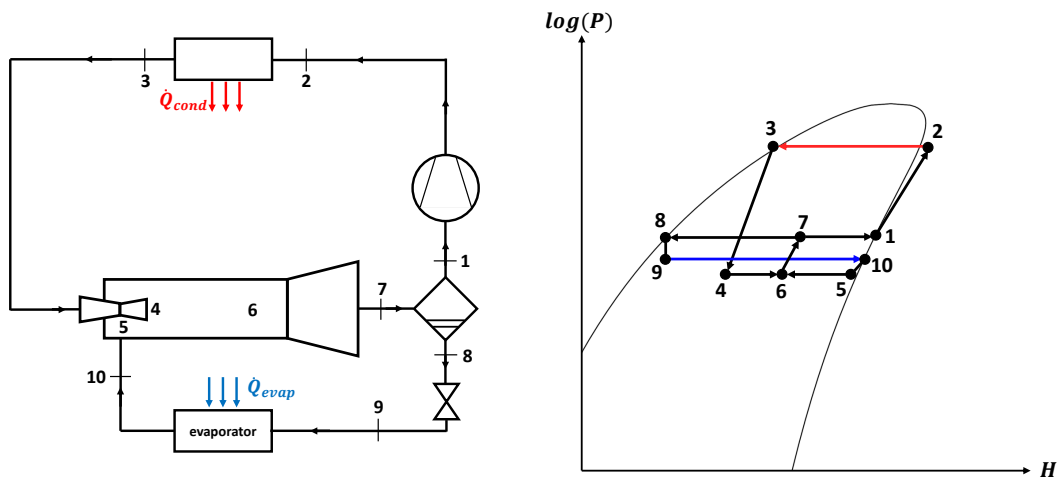
Figure 5.2: Heat pump with ejector: Schematic cycle layout and theoretical log(p)-H diagram

48

Two key parameters of an ejector are its entrainment ratio, η, i.e. the ratio of secondary to primary inlet mass flow rate, defined as

$$\eta = \frac{\dot{m}_{in,sec}}{\dot{m}_{in,prim}} \tag{5.1}$$

and the suction pressure ratio, i.e. the ratio of outlet pressure to secondary inlet pressure, defined as

$$\Pi_S = \frac{p_{out}}{p_{in,sec}} \tag{5.2}$$

One issue concerning ejector performance is that for a given ejector geometry, there exists only a small bandwidth of operating conditions that is leading to optimum efficiency, or vice versa for given operating conditions, an optimum geometric design exists[33, 37, 38]. Therefore, the shape of an ejector should be optimized based on the expected operating conditions. Obviously, this implies poor ejector performance when e.g. operating the system on partial load. Recently, efforts have been made to design ejectors where the geometry can be varied to adapt to variable operating conditions, e.g. by a movable spindle within the primary nozzle that allows for adjusting the primary nozzle area ratio[33]. Varga et al.[37] numerically analyzed a (single-phase) vapor jet ejector for refrigerating applications working with isobutane to show that a movable spindle in the primary nozzle can be used to effectively cover a broad range of operating conditions.

Most experimental and numerical studies on supersonic two-phase ejectors were performed using CO_2 as working fluid. Banasiak and Hafner[38] developed a one-dimensional numerical model of a CO_2 ejector by identifying the dominant physical processes of each subsection of the ejector. Thermodynamic metastability effects were included and the model was calibrated and validated using experimental data for transcritical CO_2 operating conditions. The model is capable of predicting global quantities such as the entrainment ratio, but cannot give detailed information on the flow patterns inside the ejector and cannot be used for other fluids as fine-tuning using experimental data is necessary. Smolka et al.[39] developed a Homogeneous Equilibrium Model (HEM) to perform CFD simulations of a two-phase transcritical CO_2 ejector with a commercial CFD code without having to employ a full multiphase model, as through the assumption of a homogeneous equilibrium, the governing equations can be used in their single-phase formulation. Bodys et al.[40] expanded the model of [39] to account for thermodynamic metastability effects, which was realized through solving an additional equation for the vapor quality which includes a relaxation factor to be experimentally tuned. Through this addition to the homogeneous model, the prediction of CO_2 ejectors with subcritical inlet conditions was improved. Yazdani et al.[41] used a mixture model to simulate the two-phase flow of CO_2 in an ejector. The mass transfer between the phases was modeled including both boiling and cavitation phenomena. Also, a slip velocity between the phases was included in the model. The analysis did not show a better accuracy in predicting key performance parameters of an ejector than simpler models like that of [40]. Biferi et al.[42] used the HEM of [39] to simulate a supersonic ejector with R134 as working fluid. The simplification of constant material properties except for those of density and speed of sound was made without drawbacks in accuracy. Also, a comparison with results from a commercially available non-equilibrium model and experimental data was drawn.

5.2   Mathematical Modeling

5.2.1   Multiphase Flow

As inside a multiphase ejector both the liquid and vapor phase of the refrigeran are present at the same time, the modeling of this multiphase flow has to be considered. Generally, multiphase flows can be characterized by the types of phases present, e.g. liquid-solid, solid-solid, gas-solid, gas-liquid, etc. Obviously, there can be more than two phases present. Additionally to the number of phases and their respective states of matter, the phases can be either dispersed or continuous. This classification is not always easy, as small gas bubbles in a liquid can be characterised as being dispersed, but the larger a bubble becomes, the more it can also be seen as continuous phase. Another important characteristic of a multiphase system is its coupling. Considering a continuous and a dispersed phase, in a system where the continuous phase is unaffected by the dispersed phase, the coupling is classified as one-way. Two-way coupling occurs when the continuous phase is also affected by the dispersed phase. Four-way coupling is present when, additionally, the particles of the dispersed phase interact with each other. An important measure for judging the coupling of two phases is the Stokes number of a system, defined as the ratio of the dispersed and continuous phases' timescales. Considering a multiphase system, another important factor is whether the involved phases are inert, like e.g. water and air, or if mass transfer is occurring between the phases, like e.g. water and steam during boiling.
Catering to the specific processes involved in the various types of multiphase flows outlined above, different multiphase models have evolved over time, of which the most commonly used ones are mentioned briefly below[7, 43].

The Euler-Lagrange Model

Here, the continuous phase is modeled as a continuum, in the same way as a single phase problem, using the Navier-Stokes equations, continuity equations, energy equation, and so forth in their single-phase formulation. The dispersed phase is modeled as a finite number of particles that follow the flow of the continuous phase and can interact with the continuous phase by exchanging momentum, mass and energy.

The Euler-Euler Model

This model treats both phases as continuous phases, solving the Navier-Stokes equations, continuity equation, energy equation and so on for both phases individually. Computationally this model is much more costly than the Euler-Lagrange approach, and the system of equations needs to be closed, which needs the introduction of additional models, mostly using empirical data.

The Mixture Model

Within this model, the assumption is made that interaction of both phases is strong and therefore the momentum equations are solved for the mixture of the phases, with material properties being determined for the mixture as a whole. If necessary, a slip velocity between both phases can be accounted for. This model is computationally less expensive than a full Euler-Euler model.

The Volume-of-Fluid Model

This model is similar to the Euler-Euler models, but additionally, the phase interface is being tracked, making it suitable for segregated multiphase flows with a distinct interface, such as flows involving large bubbles.

5.2.2 Homogeneous Equilibrium Model

The homogeneous equilibrium model (HEM) is a simple formulation of a mixture model. In the HEM approach, the fluid is modeled as an ideally homogeneous mixture of the liquid and vapor phase, with both phases in thermodynamic equilibrium. Therefore

$$T_1 = T_2 = T \tag{5.3}$$

$$v_1 = v_2 = v \tag{5.4}$$

$$p_1 = p_2 = p \tag{5.5}$$

with index 1 and 2 denoting the liquid and vapor phase, respectively. As a consequence, the governing equations can be written in single-phase formulation, therefore the continuity equation and Navier-Stokes equation are used in the form of Eq. (2.42) and Eq. (2.43), respectively. Omitting the derivatives with respect to time for a steady-state case and employing the Boussinesq assumption, the continuity and Navier-Stokes equations read

$$\frac{\partial \overline{\rho} \widetilde{v}_i}{\partial x_i} = 0 \tag{5.6}$$

$$\frac{\partial (\overline{\rho} \widetilde{v}_i \widetilde{v}_j)}{\partial x_j} = -\frac{\partial (\overline{p} + 2\overline{\rho} k/3)}{\partial x_i} + \frac{\partial}{\partial x_j} \left[(\mu + \mu_t) \left(\frac{\partial \widetilde{v}_i}{\partial x_j} + \frac{\partial \widetilde{v}_j}{\partial x_i} - \frac{2}{3} \delta_{ij} \frac{\partial \widetilde{v}_k}{\partial x_k} \right) \right] \tag{5.7}$$

The assumption of a thermodynamic equilibrium means that heat transfer occurs immediately and thus phase changes occur instantaneously. Therefore, metastability effects cannot be accounted for with this model. The other extreme case, where no phase change occurs at all would lead to the homogeneous frozen model. Real-world two-phase flows usually exhibit a behaviour somewhere in between[43]. Smolka et al.[39] used a homogeneous equilibrium model for the simulation of the transcritical two-phase flow of CO_2 in an ejector. The authors derived an enthalpy-based energy equation to then obtain all fluid properties as functions of pressure and enthalpy. This is necessary for two-phase flows, as phase change is an isothermal process and therefore the standard, temperature-based formulation of the energy equation is not suitable for calculations of such flows. The enthalpy-based energy equation is derived following the method of [39] as follows.

Derivation of an Enthalpy-Based Energy Equation

A steady-state temperature-based formulation of the energy equation for instantaneous (i.e. non-decomposed and non-averaged) variables reads

$$\frac{\partial}{\partial x_j} \left[\rho v_j \left(h + \frac{v_i v_i}{2} \right) \right] = \frac{\partial}{\partial x_j} \left(\lambda \frac{\partial T}{\partial x_j} + \tau_{ij} v_i \right) \tag{5.8}$$

Using

$$\left. \frac{\partial h}{\partial p} \right|_T dp + \left. \frac{\partial h}{\partial T} \right|_p dT = dh \tag{5.9}$$

51

to express temperature, T, in Eq. (5.8) leads to

$$\frac{\partial}{\partial x_j}\left(\lambda\frac{\partial T}{\partial x_j}\right) = \frac{\partial}{\partial x_j}\left(\frac{\lambda}{\left.\frac{\partial h}{\partial T}\right|_p}\frac{\partial h}{\partial x_j}\right) - \frac{\partial}{\partial x_j}\left(\frac{\lambda\left.\frac{\partial h}{\partial p}\right|_T}{\left.\frac{\partial h}{\partial T}\right|_p}\frac{\partial p}{\partial x_j}\right) \tag{5.10}$$

Introducing a diffusivity Γ as

$$\Gamma = \frac{\lambda}{\left.\frac{\partial h}{\partial T}\right|_p} = \frac{\lambda}{c_p} \tag{5.11}$$

Eq. (5.10) can be written as

$$\frac{\partial}{\partial x_j}\left(\lambda\frac{\partial T}{\partial x_j}\right) = \frac{\partial}{\partial x_j}\left(\Gamma\frac{\partial h}{\partial x_j}\right) - \frac{\partial}{\partial x_j}\left(\Gamma\left.\frac{\partial h}{\partial p}\right|_T\frac{\partial p}{\partial x_j}\right) \tag{5.12}$$

The second term on the right hand side of Eq. (5.12) containing the pressure gradient is omitted as diffusive heat transport is of little importance in transonic flow and additionally, the dependence of enthalpy on pressure is far smaller than that of temperature[39]. Therefore, Eq. (5.8) is rewritten as

$$\frac{\partial}{\partial x_j}\left[\rho v_j\left(h + \frac{v_i v_i}{2}\right)\right] = \frac{\partial}{\partial x_j}\left[\left(\Gamma\frac{\partial h}{\partial x_j}\right) + \tau_{ij} v_i\right] \tag{5.13}$$

All variables in Eq. (5.13) are now Favre-decomposed according to Eq. (2.40) and Reynolds-averaged according to Eq. (2.12).

$$\begin{aligned}\frac{\partial}{\partial x_j}&\left[\overline{\rho\left(\widetilde{v}_j + v_j''\right)\left(\widetilde{h} + h'' + \frac{(\widetilde{v}_i + v_i'')(\widetilde{v}_i + v_i'')}{2}\right)}\right] = \\ &\frac{\partial}{\partial x_j}\left[\Gamma\frac{\partial}{x_j}\overline{\left(\widetilde{h} + h''\right)}\right] + \frac{\partial}{\partial x_j}\left[\overline{\left(\widetilde{\tau}_{ij} + \tau_{ij}''\right)\left(\widetilde{v}_i + v_i''\right)}\right]\end{aligned} \tag{5.14}$$

To further simplify Eq. (5.14), the following identity is used.

$$\overline{\rho\phi''} = 0 \tag{5.15}$$

Eq. (5.15) can be derived using Eqs. (2.40) and (2.41). Starting from Eq. (2.40) the fluctuation of ϕ with respect to the Favre average can be expressed as

$$\phi'' = \phi - \widetilde{\phi} \tag{5.16}$$

$$\phi'' = \phi - \frac{\overline{\rho\phi}}{\overline{\rho}} \tag{5.17}$$

multiplying both sides of Eq. (5.17) with ρ and taking the Reynolds average yields

$$\overline{\rho\phi''} = \overline{\rho\phi} - \frac{\overline{\rho\overline{\rho\phi}}}{\overline{\rho}} = \overline{\rho\phi} - \overline{\rho\phi} = 0 \tag{5.18}$$

Using Eq. (5.15), the left-hand side of Eq. (5.14) is simplified to

$$\frac{\partial}{\partial x_j}\left(\overline{\rho\widetilde{v}_j\widetilde{h}} + \overline{\widetilde{v}_j\rho\frac{\widetilde{v}_i\widetilde{v}_i}{2}} + \overline{\widetilde{v}_j\rho\frac{v_i''v_i''}{2}} + \overline{\rho v_j''h''} + \overline{v_j''\rho\frac{v_i''v_i''}{2}} + \overline{v_j''\rho v_i''\widetilde{v}_i}\right) \tag{5.19}$$

The definition of the turbulent kinetic energy (here for fluctuations of velocity with respect to Favre-averaging)

$$k = \frac{\overline{v_i'' v_i''}}{2} \tag{5.20}$$

is used to express the third term of Eq. (5.19). The fifth term in Eq. (5.19) which contains triple correlations of velocity fluctuations is neglected. Furthermore, a model for the fourth term containing the correlation of fluctuations of velocity and enthalpy is introduced based on the assumption of a gradient-diffusion mechanism.

$$\overline{\rho v_j'' h''} = -\Gamma_t \frac{\partial \widetilde{h}}{\partial x_j} \tag{5.21}$$

where

$$\Gamma_t = \frac{\mu_t}{\sigma_t} \tag{5.22}$$

with σ_t denoting the turbulent Prandtl number. Finally, the left-hand side of Eq. (5.14) reads

$$\frac{\partial}{\partial x_j} \left(\overline{\rho} \widetilde{v}_j \widetilde{h} + \overline{\rho} \widetilde{v}_j \frac{\widetilde{v}_i \widetilde{v}_i}{2} + \overline{\rho} \widetilde{v}_j k - \Gamma_t \frac{\partial \widetilde{h}}{\partial x_j} + \overline{\rho} \widetilde{v}_i \overline{v_i'' v_j''} \right) \tag{5.23}$$

where the last term in Eq. (5.23) notably contains the Reynolds stress tensor. The right-hand side of Eq. (5.14) is now simplified by neglecting the term containing h''. As the viscous stress tensor, τ_{ij}, contains the density, ρ, - cf. Eq. (2.5) - Eq. (5.15) can again be used to omit the products of fluctuations and averaged quantities containing τ_{ij}. Now, the right-hand side of Eq. (5.14) reads

$$\frac{\partial}{\partial x_j} \left(\Gamma \frac{\partial \widetilde{h}}{\partial x_j} \right) + \frac{\partial}{\partial x_j} \left(\widetilde{\tau}_{ij} \widetilde{v}_i + \overline{\tau_{ij}'' v_i''} \right) \tag{5.24}$$

The last term of Eq. (5.24), which features stress-velocity correlations, is neglected as this phenomenon decreases for high-Reynolds number turbulence[11]. Putting the left-hand side, Eq.(5.23), and the right-hand side, Eq. (5.24), together gives

$$\frac{\partial}{\partial x_j} \left(\overline{\rho} \widetilde{v}_j \widetilde{h} + \overline{\rho} \widetilde{v}_j \frac{\widetilde{v}_i \widetilde{v}_i}{2} + \overline{\rho} \widetilde{v}_j k - \Gamma_t \frac{\partial \widetilde{h}}{\partial x_j} + \overline{\rho} \widetilde{v}_i \overline{v_i'' v_j''} \right) = \frac{\partial}{\partial x_j} \left(\Gamma \frac{\partial \widetilde{h}}{\partial x_j} \right) + \frac{\partial \left(\widetilde{\tau}_{ij} \widetilde{v}_i \right)}{\partial x_j} \tag{5.25}$$

The continuity equation and the product rule can be used in Eq. (5.25) to show that

$$\frac{\partial}{\partial x_j} \left(\overline{\rho} \widetilde{v}_j k \right) = \left(\overline{\rho} \widetilde{v}_j \right) \frac{\partial k}{\partial x_j} + k \frac{\partial \left(\overline{\rho} \widetilde{v}_j \right)}{\partial x_j} = \left(\overline{\rho} \widetilde{v}_j \right) \frac{\partial k}{\partial x_j} \tag{5.26}$$

Now, an equation for the conservation of mechanical energy is formulated in the following way.

$$\frac{\partial}{\partial x_j} \left(\overline{\rho} \widetilde{v}_j \frac{\widetilde{v}_i \widetilde{v}_i}{2} \right) = -\widetilde{v}_j \frac{\partial \overline{p}}{\partial x_j} + \widetilde{v}_i \frac{\partial (\widetilde{\tau}_{ij} - \overline{\rho v_i'' v_j''})}{\partial x_j} \tag{5.27}$$

The last term of Eq. (5.27) features the partial derivative of the sum of viscous and Reynolds stresses. Eq. (5.27) is now subtracted from Eq. (5.25). This leads, after rearranging the terms, to

the following equation for conservation of thermal energy.

$$\frac{\partial}{\partial x_j}\left(\overline{\rho}\widetilde{v}_j\widetilde{h}\right) = \frac{\partial}{\partial x_j}\left[(\Gamma + \Gamma_t)\frac{\partial\widetilde{h}}{\partial x_j}\right] + \widetilde{v}_j\frac{\partial\overline{p}}{\partial x_j} - \overline{\rho}\widetilde{v}_j\frac{\partial k}{\partial x_j}$$
$$+ \frac{\partial\widetilde{v}_i}{\partial x_j}\left(\widetilde{\tau}_{ij} - \overline{\rho v_i'' v_j''}\right) \tag{5.28}$$

Using the Boussinesq assumption, Eq. (2.44), to model the Reynolds stress tensor in Eq. (5.28) yields the enthalpy-based energy equation in its final form.

$$\frac{\partial}{\partial x_j}\left(\overline{\rho}\widetilde{v}_j\widetilde{h}\right) = \frac{\partial}{\partial x_j}\left[(\Gamma + \Gamma_t)\frac{\partial\widetilde{h}}{\partial x_j}\right] + \widetilde{v}_j\frac{\partial\overline{p}}{\partial x_j} - \overline{\rho}\widetilde{v}_j\frac{\partial k}{\partial x_j}$$
$$+ (\mu + \mu_t)\left[\left(\frac{\partial\widetilde{v}_i}{\partial x_j} + \frac{\partial\widetilde{v}_i}{\partial x_j}\right)\frac{\partial\widetilde{v}_i}{\partial x_j} - \frac{2}{3}\left(\frac{\partial\widetilde{v}_k}{\partial x_k}\right)^2\right] - \frac{2}{3}\overline{\rho}k\frac{\partial\widetilde{v}_j}{\partial x_j} \tag{5.29}$$

As ANSYS FLUENT does not offer the capability of employing the HEM approach, the model is implemented via the means of user-defined functions (UDF). A UDF is C-based code, with some FLUENT-specific libraries, which can be used to implement solutions that are not included in the FLUENT code. The enthalpy-based energy equation, Eq. (5.29), is implemented in ANSYS FLUENT via the means of a user-defined scalar transport equation (UDS), which is a generic transport equation that in steady-state formulation reads[10]

$$\frac{\partial(\overline{\rho}\widetilde{v}_j\phi)}{\partial x_j} = \frac{\partial}{x_j}\left(\Gamma\frac{\partial\phi}{\partial x_j}\right) + \sum_n S_n \tag{5.30}$$

where in Eq. (5.30) Γ is the diffusivity of the scalar ϕ and S_n are source terms. Eq. (5.29) can be brought into UDS form in the following way.

$$\frac{\partial}{\partial x_j}\left(\overline{\rho}\widetilde{v}_j\widetilde{h}\right) = \frac{\partial}{\partial x_j}\left(\Gamma_{eff}\frac{\partial\widetilde{h}}{\partial x_j}\right) + S_1 + S_2 + S_3 \tag{5.31}$$

$$\Gamma_{eff} = \Gamma + \Gamma_t = \frac{\lambda}{c_p} + \frac{\mu_t}{\sigma_t} \tag{5.32}$$

$$S_1 = \widetilde{v}_j\frac{\partial\overline{p}}{\partial x_j} \tag{5.33}$$

$$S_2 = (\mu + \mu_t)\left[\left(\frac{\partial\widetilde{v}_i}{\partial x_j} + \frac{\partial\widetilde{v}_i}{\partial x_j}\right)\frac{\partial\widetilde{v}_i}{\partial x_j} - \frac{2}{3}\left(\frac{\partial\widetilde{v}_k}{\partial x_k}\right)^2\right] - \frac{2}{3}\overline{\rho}k\frac{\partial\widetilde{v}_j}{\partial x_j} \tag{5.34}$$

$$S_3 = -\overline{\rho}\widetilde{v}_j\frac{\partial k}{\partial x_j} \tag{5.35}$$

Physically, S_1 represents mechanical energy, S_2 represents viscous dissipation and S_3 represents dissipation of turbulent kinetic energy.

Material Properties

The material properties of the working fluid are obtained from the COOLPROP library[44]. For that purpose, the pressure-enthalpy space of interest is discretized into a finite number of equally spaced

pressure- and enthalpy points by creating a pressure vector p_i and an enthalpy vector h_j. Now, using the COOLPROP library, for every combination of $[p, h]$, two-dimensional property arrays, e.g. ρ_{ij} for density, are filled with the corresponding values. This is done regardless of the fluid being in subcooled, superheated, two-phase or supercritical state. During the simulation procedure, every time a fluid property needs to be calculated, a bilinear interpolation is performed to obtain material properties for any combination of pressure and enthalpy handled to the UDF by the solver. The dependence of material properties on pressure and enthalpy is generally nonlinear and therefore an error is introduced. This error can be minimized by increasing the number of pressure and enthalpy points, which comes at additional computational cost. Also, the point spacing can be altered to provide a denser grid of points in the area where the solution is expected. However, during this work it was noticed that once a sufficiently dense grid is used, further refinement does not provide more accuracy. Using a too dense grid of pressure and enthalpy points was also observed to reduce numerical stability. The optimum in terms of accuracy versus computational costs and numerical instabilities was found to lie around approximately 1 pressure point per 1 bar.

Within this work, all material properties are incorporated in the computational scheme in this manner. However, to reduce computational costs, only density, ρ, and speed of sound, c, could be incorporated as look-up tables. Other quantities such as viscosity, μ, thermal conductivity, λ, and heat capacity, c_p, would then assumed as being constant. This approach was also taken by [45]. Then, after obtaining a converged solution with constant material properties, the simulation can be re-run with all material properties being pressure- and enthalpy dependent. Especially for computationally more expensive simulations, e.g. three-dimensional problems or transient simulations, this method can provide a way of decreasing computational times.

As the enthalpy-based energy equation used within the HEM does not explicitly feature temperature, after each iteration in the calculation process, a loop over all computational cells is performed to calculate the static temperature and the vapor quality of the respective cell. Both values are again incorporated in the form of two-dimensional look-up tables using pressure and enthalpy as variables.

The COOLPROP library does not offer values for the speed of sound within the two-phase region, as the speed of sound is generally not defined for two-phase flow. Interestingly, while the speed of sound for a liquid is generally higher than that of a gas, the speed of sound for a homogeneous two-phase mixture lies below that of the liquid and the vapor phase[46]. Numerous formulations for the speed of sound of a two-phase mixture exist. The one chosen for this model is used e.g. in [45] and [41] and is a simple and robust formulation with no jump discontinuity at saturation lines. It reads

$$c = \sqrt{\left[\rho\left(\frac{\alpha_2}{\rho_2 c_2^2} + \frac{1 - \alpha_2}{\rho_1 c_1^2}\right)\right]^{-1}} \tag{5.36}$$

where index 1 and 2 denote the saturated liquid and saturated vapor state, respectively and $\alpha_2 = V_2/V$ is the volume fraction of the vapor phase. The vapor quality χ is defined as $\chi = m_2/m$ and furthermore, χ and α_2 are related through $\chi\rho = \alpha_2\rho_2$. Figure 5.3 shows the speed of sound of two-phase butane calculated using Eq. (5.36), plotted depending on χ and α_2, respectively. As explained above, material properties such as density are obtained from look-up tables with pressure and enthalpy as variables. The data points stored in these look-up tables are plotted in Figure 5.4 for density and speed of sound. The values are calculated using bilinear interpolation, for which a formula is derived below.
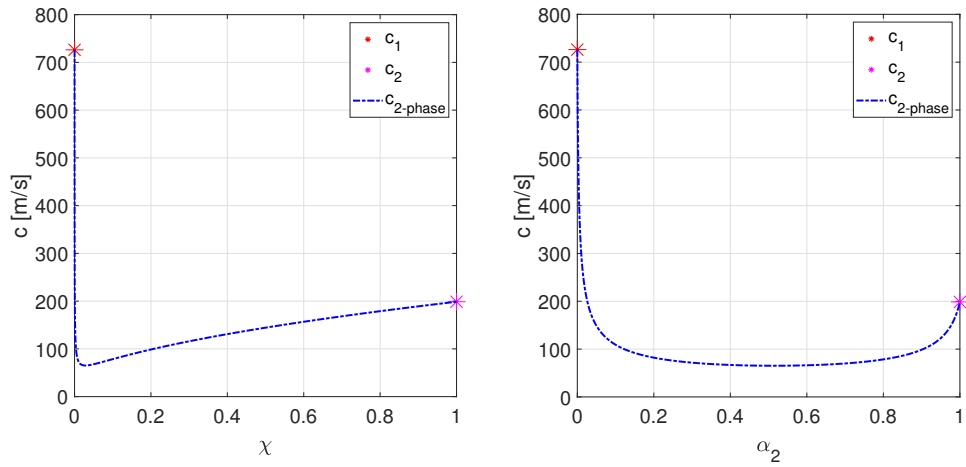
55

Figure 5.3: Speed of sound for a homogeneous two-phase mixture of liquid and vapor butane at $p = 5$ bar using Eq. (5.36)
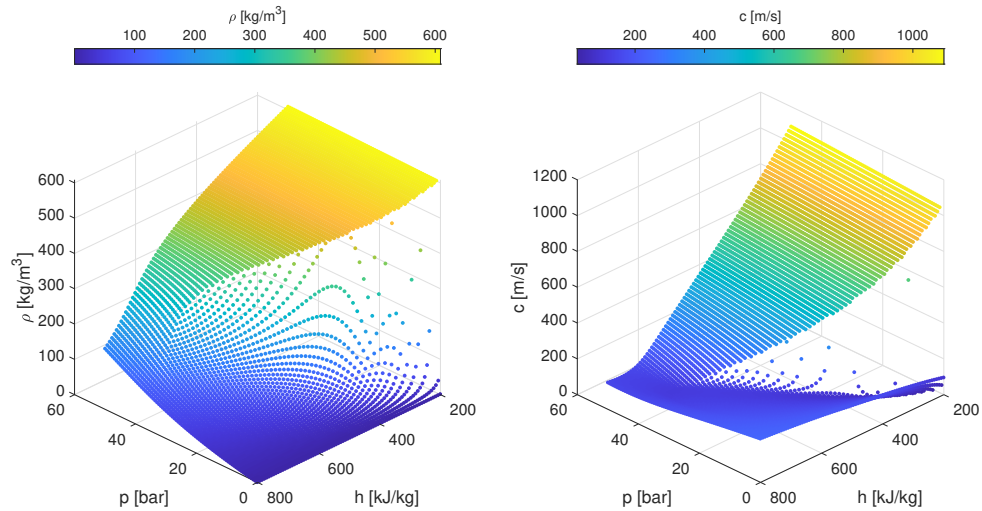

Figure 5.4: Point clouds of look-up tables for density, ρ (left) and speed of sound, c (right)

Bilinear Interpolation

It is assumed that a function $f(x, y)$ is approximated as varying locally linearly both with respect to x and y, which means that $f(x, y)$ is approximated through a first-order Taylor series expansion. Given values $[f(x_1, y_1), f(x_1, y_2), f(x_2, y_1), f(x_2, y_2)]$ are known, first linear interpolation along x is performed at a fixed value of $y = y_1$, yielding

$$
\begin{aligned}
f(x, y_1) &= f(x_1, y_1) + \frac{x - x_1}{x_2 - x_1} \left(f(x_2, y_1) - f(x_1, y_1) \right) \\
&= \frac{x_2 - x}{x_2 - x_1} f(x_1, y_1) + \frac{x - x_1}{x_2 - x_1} f(x_2, y_1)
\end{aligned}
\tag{5.37}
$$

and analogously at a fixed value of $y = y_2$, yielding

$$
f(x, y_2) = \frac{x_2 - x}{x_2 - x_1} f(x_1, y_2) + \frac{x - x_1}{x_2 - x_1} f(x_2, y_2)
\tag{5.38}
$$

Combining Eqs. (5.37) and (5.38) and performing linear interpolation along y gives

$$
\begin{aligned}
f(x, y) = \frac{y_2 - y}{y_2 - y_1} &\left[\frac{x_2 - x}{x_2 - x_1} f(x_1, y_1) + \frac{x - x_1}{x_2 - x_1} f(x_2, y_1) \right] + \\
\frac{y - y_1}{y_2 - y_1} &\left[\frac{x_2 - x}{x_2 - x_1} f(x_1, y_2) + \frac{x - x_1}{x_2 - x_1} f(x_2, y_2) \right]
\end{aligned}
\tag{5.39}
$$

which is simplified to

$$
f(x, y) =
$$
$$
\frac{1}{(x_2 - x_1)(y_2 - y_1)} \Big[f(x_1, y_1)(y_2 - y)(x_2 - x) + f(x_2, y_1)(y_2 - y)(x - x_1) +
$$
$$
f(x_1, y_2)(y - y_1)(x_2 - x) + f(x_2, y_2)(y - y_1)(x - x_1) \Big]
\tag{5.40}
$$

Eq. (5.40) is used to obtain material properties from the look-up tables (cf. Figure 5.4), where, for the example of density, $f(x, y) = \rho(p, h)$.

5.2.3 Turbulence Modeling

The commonly used k-ε models are based on Eqs. (2.47) and (2.51) which are written again here for the sake of convenience.

$$
\frac{\partial (\overline{\rho} k)}{\partial t} + \frac{\partial (\overline{\rho} \widetilde{v}_j k)}{\partial x_j} = \frac{\partial}{\partial x_j} \left[\left(\mu + \frac{\mu_t}{\sigma_k} \right) \frac{\partial k}{\partial x_j} \right] + P^k - \overline{\rho} \varepsilon
\tag{5.41}
$$

$$
\frac{\partial (\overline{\rho} \varepsilon)}{\partial t} + \frac{\partial (\overline{\rho} \widetilde{v}_j \varepsilon)}{\partial x_j} = \frac{\partial}{\partial x_j} \left[\left(\mu + \frac{\mu_t}{\sigma_\varepsilon} \right) \frac{\partial \varepsilon}{\partial x_j} \right] + \frac{\varepsilon}{k} C_{\varepsilon 1} P^k - \frac{\varepsilon^2}{k} C_{\varepsilon 2} \overline{\rho}
\tag{5.42}
$$

Besides the k-ε models there is another widely used class of two-equation turbulence models: the k-ω models. Instead of solving a transport equation for ε, a transport equation for the specific dissipation, ω is solved. Physically, ω is a specific dissipation, as in terms of dimensions,

$$
\omega \propto \varepsilon / k
\tag{5.43}
$$

Therefore, ω can be seen as the inverse of the timescale of dissipation[7]. Instead of deriving an equation for ω from scratch, Eq. (5.43) can be used to obtain an equation from the k-ε model by introducing a constant β^*.

$$\omega = \frac{\varepsilon}{\beta^* \, k} \tag{5.44}$$

Usually, this constant is set to $\beta^* = C_\mu$, cf. Eq. (2.31). Using Eq. (5.44), an equation for ω can be obtained in the following way[8].

$$\begin{aligned}
\frac{d\omega}{dt} &= \frac{d}{dt}\left(\frac{\varepsilon}{\beta^* \, k}\right) = \frac{1}{\beta^* \, k}\frac{d\varepsilon}{dt} + \frac{\varepsilon}{\beta^*}\frac{d(1/k)}{dt} \\
&= \frac{1}{\beta^* \, k}\frac{d\varepsilon}{dt} - \frac{\varepsilon}{\beta^* \, k^2}\frac{dk}{dt} = \frac{1}{\beta^* \, k}\frac{d\varepsilon}{dt} - \frac{\omega}{k}\frac{dk}{dt}
\end{aligned} \tag{5.45}$$

Using Eqs. (5.41) and (5.42), Eq. (5.45) can be used to derive an equation for ω. This is done by adding the respective terms (i.e. production, dissipation, turbulent diffusion and viscous diffusion) of the k- and ε-equations using the scheme laid out in Eq. (5.45). The ω-equation reads

$$\frac{\partial(\overline{\rho}\omega)}{\partial t} + \frac{\partial(\overline{\rho}\widetilde{v}_j\omega)}{\partial x_j} = \frac{\partial}{\partial x_j}\left[\left(\mu + \frac{\mu_t}{\sigma_\varepsilon}\right)\frac{\partial\omega}{\partial x_j}\right] + \alpha\frac{\omega}{k}P^k - \beta\overline{\rho}\omega^2 + \frac{2}{k}\left(\mu + \frac{\mu_t}{\sigma_\varepsilon}\right)\frac{\partial k}{\partial x_i}\frac{\partial\omega}{\partial x_i} \tag{5.46}$$

where $\alpha = C_{\varepsilon 1} - 1 = 0.44$ and $\beta = (C_{\varepsilon 2} - 1)\beta^* = 0.0828$.

The k-ω model performs better than the k-ε model at low Reynolds numbers when turbulence is relatively low. This is because in the k-ε model, the term in the ε-equation involving ε^2/k can cause numerical instability. When turbulence is low, e.g. in the vicinity of a wall, both $k \to 0$ and $\varepsilon \to 0$. If both k and ε do not approach zero at the correct rate, which can hardly be ensured, this term involving ε^2/k can easily take unphysical values. In the k-ω model, when $k \to 0$, the diffusion term approaches zero, but the production term is not affected, as the term ω/k in the production term cancels out when expanding P^k[9]. The k-ω model therefore correctly models wall-bounded flows within the viscous sub-layer. Therefore, wall functions can be used to decrease the required cell density near walls, but are not needed to correctly model wall-bounded flows. If omitting wall functions when using the k-ω model, this comes at the cost of having to use a dense computational grid near walls, with the first cell at the wall being placed at $y^+ < 5$. Another advantage of the k-ω model over the k-ε model is that it can handle adverse pressure gradients in wall-bounded flows, and therefore boundary layer separations better[7, 8]. However, the k-ω model comes with the disadvantage of being dependent on the value of ω in the free-stream. To combine the advantages of both models, the k-ω SST (Shear Stress Transport) model uses the k-ω model in vicinity of walls and the k-ε in the free-stream, with a smooth transition in between models. This is achieved by using the fact that, through Eq. (5.44), Eq. (5.46) can be used as an equation for ε, if the coefficients in Eq. (5.46) are changed to the values of the k-ε model. This is done by a function F_1 that smoothly varies from $F_1 = 1$ in vicinity of the wall and $F_1 = 0$ in the region of the outer boundary layer, from where on the k-ε model is used. Therefore, coefficients (here for the example of β) are calculated as

$$\beta_{SST} = F_1\beta_{k-\omega} + (1 - F_1)\beta_{k-\varepsilon} \tag{5.47}$$

$$F_1 = \tanh(\zeta^4) \tag{5.48}$$

$$\zeta = \min\left[\max\left(\frac{\sqrt{k}}{\beta^* \, \omega y}, \frac{500\nu}{y^2\omega}\right), \frac{4\sigma_{\omega 2}k}{CD_\omega y^2}\right] \tag{5.49}$$

58

Additionally, as the cross-diffusion term, which is the last term on the right-hand side of Eq. (5.46) is not present in the K-ε equation, it is in the SST model multiplied with $(1 - F_1)$[8].

The k-ω SST model is used for the ejector simulations within this work. It was noticed that both the standard and realizable k-ε model showed to lead to convergence problems in some simulations by over-predicting the production of turbulence at the shear layer between the low-pressure and high-pressure stream in the ejector at the location where the jet from the primary nozzle is decelerated to a subsonic level.

5.3 Validation of HEM Approach: ERCOFTAC UFR 4-19 Test Case

For validation of the enthaply-based energy equation and the subroutines implemented via UDFs, a compressible single-phase flow benchmark case is used. For this purpose, the ERCOFTAC UFR 4-19 case[47] is simulated once using the built-in energy equation and ideal gas law offered in FLUENT and once using the enthalpy-based energy equation and real-fluid material property lookup tables implemented via UDFs (denotes as HEM). Throughout this chapter, results obtained with the built-in energy equation and ideal gas law of FLUENT are marked with "Fluent", and results obtained using the enthalpy-based energy equation and UDF-subroutines are marked with "HEM".

The UFR 4-19 test case is a converging-diverging plane diffuser for which experimental data is available for two transonic cases, of which the "weak shock" case is chosen here. A single-phase flow case is chosen for this test run because the aim is to validate the enthalpy-based energy equation and UDF-subroutines themselves (as opposed to the general question if a certain two-phase flow can be modeled as being in homogeneous equilibrium). The boundary conditions of the UFR 4-19 case are listed in Table 5.1. For both the simulations using the built-in capabilities of FLUENT and the HEM, the standard k-ε turbulence model with scalable wall functions and compressibilty correction (cf. chapter 4.2) is used. Cell-based least squares discretization is used for gradient calculations and second order (upwind, except for pressure) schemes are used for discretization of all transport equations. The pressure-based coupled solver of ANSYS FLUENT is used.

The maximum Mach number was experimentally measured to be $Ma = 1.27$ for the given case[47].

Inlet total pressure (Pa)	135000
Outlet static pressure (Pa)	110661
Inlet total temperature (K)	277.78
inlet k (m^{2}s^{-2})	$1.74 \cdot 10^{-3}$
inlet ε (m^{2}s^{-3})	198

Table 5.1: Boundary conditions for ERCOFTAC UFR 4-19 weak shock case [47]

In Figure 5.5, the evolution of the Mach number along the line at a constant value of $y = h_{throat}/2$, which is the center of the section of minimum cross-sectional area, is plotted. The maximum Mach number is correctly predicted by both simulations. A small discrepancy can be seen between both simulations at the shock location. Figures 5.6 and 5.7 show a contour plot of the Mach number obtained using the built-in capabilities of FLUENT and the HEM implemented via UDFs, respectively. Here, both simulations provide almost identical results. Figure 5.8 shows the profiles of velocity at four distinct locations downstream the throat, which is the location of minimum cross-sectional area. Here, $x/h_{throat} = 0$ corresponds to the location of the throat, cf. Figure 5.6 for a sketch of the diffuser geometry. Experimental measurements are denoted as "Exp". While both the simulations capture the location of maximum velocity correctly, there is a deviation from
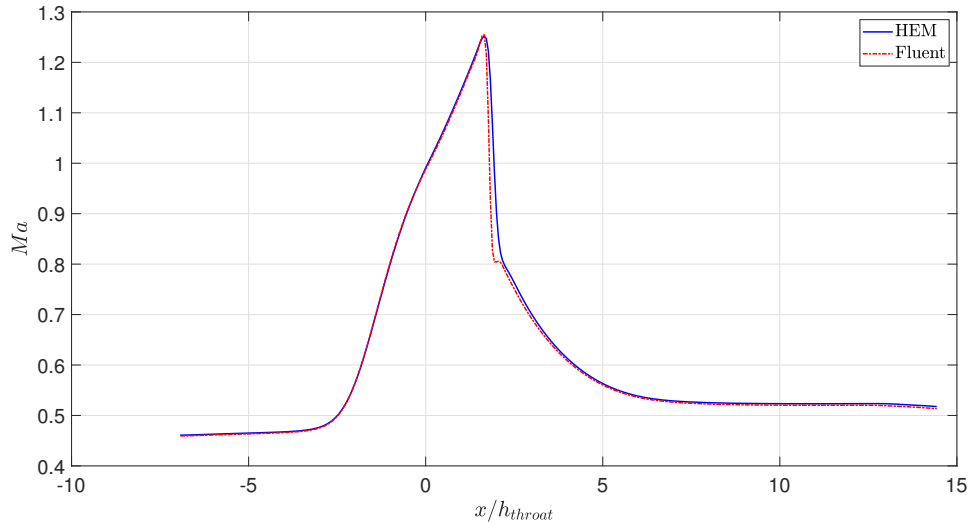
Figure 5.5: Comparison of Mach number, Ma, along line $y = h_{throat}/2$
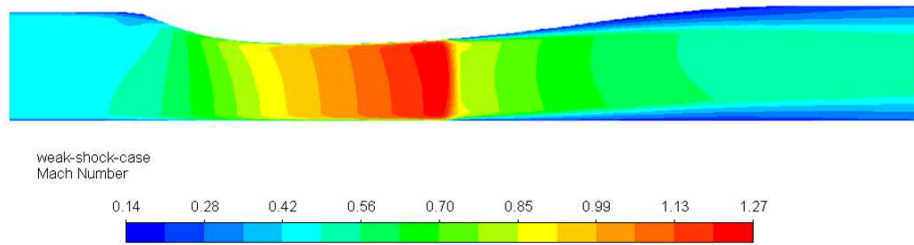

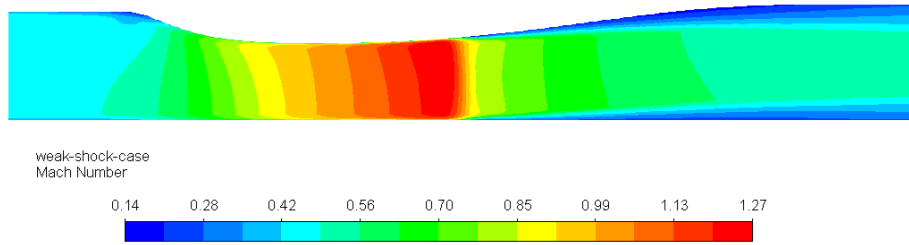Figure 5.6: Contour plot of Mach number (Fluent built-in ideal gas law)

Figure 5.7: Contour plot of Mach number (HEM)

experimental values near the walls. Interestingly, the HEM simulation provides better agreement with experimental values than the FLUENT built-in routines. In Figure 5.9, $p_s/p_{t,in}$, which is the ratio of static pressure along the wall to total inlet pressure, is plotted at the bottom and top wall, respectively. Again, experimental measurements from [47] are provided for comparison. Generally, the agreement between both simulations and experimental values is good. Both simulations tend to show similar deviations from the experimental values, therefore the accuracy of both the HEM simulation and the FLUENT built-in simulation is comparable.

The comparison of the two simulations with experimental data leads to the conclusion that the subroutines implemented via UDFs are comparable in accuracy to built-in methods of FLUENT for the simulation of a compressible single-phase flow problem. This validation is important, as it allows to rule out severe errors within the UDF C-code or the enthalpy-based energy equation. However, as mentioned above, this simulation does not provide any information on whether the assumption of a homogeneous equilibrium is valid for a certain type of flow regime.
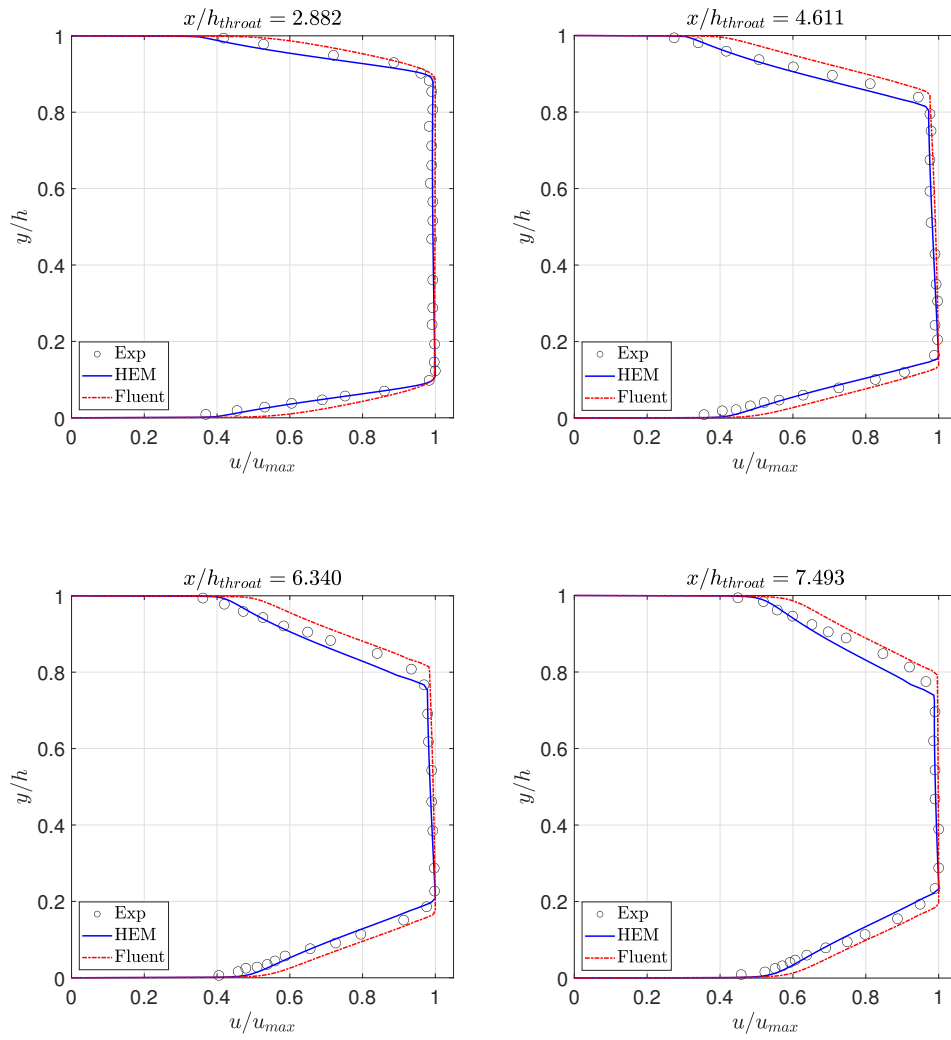
Figure 5.8: Velocity profiles at different axial positions downstream the throat
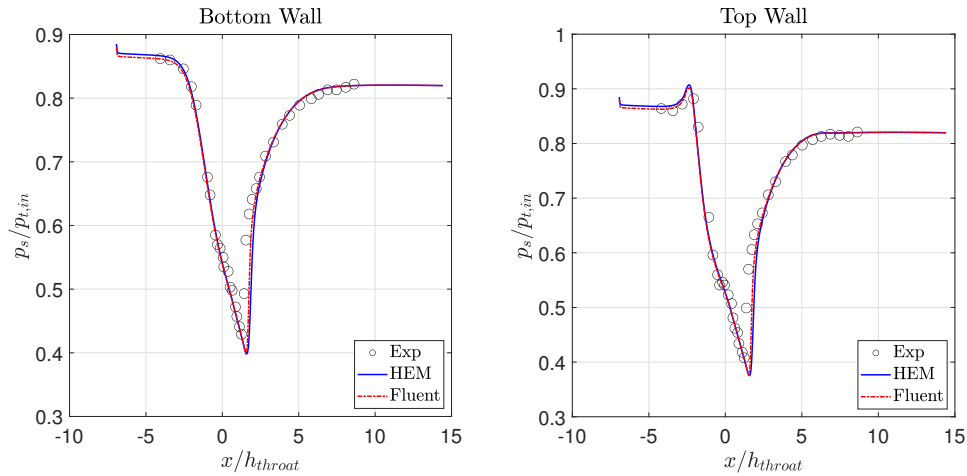
Figure 5.9: Ratio of static pressure along top and bottom wall to total inlet pressure

5.4 Numerical Methods

The pressure-based coupled solver of the commercial CFD code ANSYS FLUENT is used to solve the governing equations. Therefore, during each iteration, the momentum equations and the pressure equation are solved in a coupled manner. Then, fixing the newly calculated values for the velocity components and pressure, the turbulence equations are solved. In the last step, keeping all other values constant, the UDS (energy equation) is solved and the material properties are updated by calling the UDF that contains the C-code to perform a bilinear interpolation to obtain material properties as functions of pressure and enthalpy. All variables are discretized using first-order upwind schemes, except for pressure, where a second order pressure interpolation scheme is chosen. Second-order schemes are known to be more accurate and less diffusive, however they are not used due to high numerical instability. The drawback in accuracy of a first-order scheme over a second order scheme (given they are both of the same type, e.g. upwind schemes) can be compensated by using a denser computational grid. For the two-dimensional simulations performed in this work it was noticed that an increase in cell density comes at less computational cost than the needed measures to bring a simulation using second-order upwind schemes to convergence. Once a final, converged solution is obtained using first-order upwind schemes, the simulation is continued using a second-order upwind scheme for the discretization of velocity components only, as this helped resolve shock waves more accurately. Figure 5.10 shows the profiles of static pressure and Mach number along the axis of the ejector for a converged solution using the first-order upwind scheme and second-order upwind scheme, respectively for the face value calculation of velocity components. The solution employing the second-order scheme is obtained using a fully converged first-order scheme solution as a starting guess. As expected, the first-order scheme is more dissipative than the second-order scheme and therefore smears out the shocks. The deviation of the two solutions is only observable within the supersonic region of the ejector, where shocks occur. Further upstream

63

and downstream the difference is insignificant. Therefore, only the region from the primary nozzle throat to the beginning of the diffuser is depicted in Figure 5.10. Global quantities of interest, e.g. the entrainment ratio or mass flow rates, were not observed to be affected by the choice of either a first-order or a second-order scheme.

All gradients are calculated using the least-squares cell-based method. All simulations are performed in steady-state and using strong explicit relaxation and also implicit relaxation.

A solution is, for the simulations in this work, classified as converged once the scaled residuals of
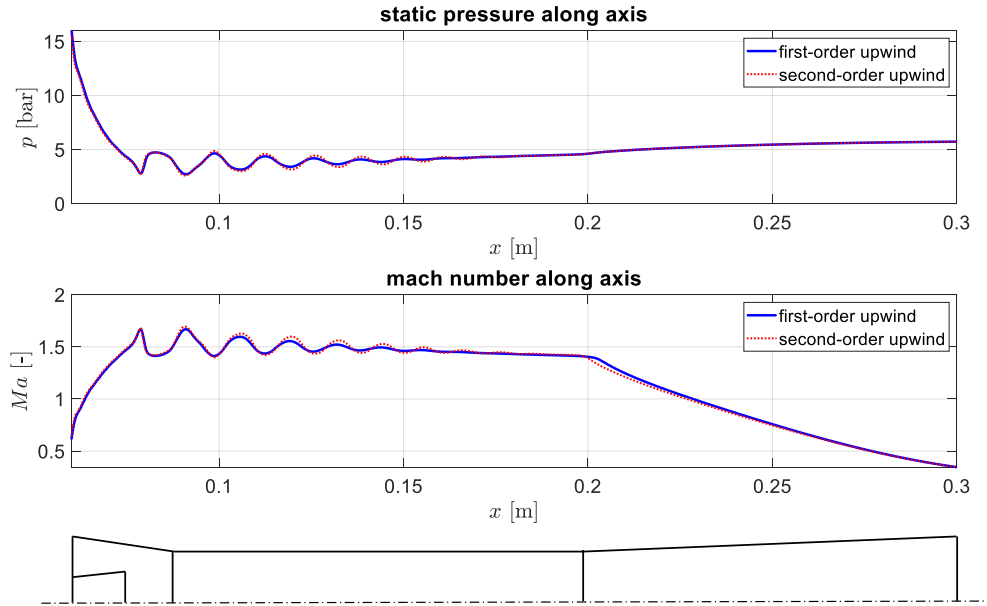

Figure 5.10: Profiles of static pressure and Mach number along ejector axis using first-order upwind and second-order upwind scheme for velocity, respectively

all equations have dropped by at least four orders of magnitude, the error in absolute global mass balance is below a value of $1 \cdot 10^{-5}$ and not changing with iterations and the entrainment ratio is at a constant value that is not changing with iterations (within a boundary of 0.001%). Also, the average and maximum velocity measured at two specific axial locations (outlet of primary nozzle and end of mixing zone) are not changing with iterations (within a boundary of 0.0001 in terms of Mach number). If all these criteria are fulfilled, a solution is, within this work, said to have converged.

5.5 Solution Strategy

Numerical schemes for solving the set of equations are very unstable for compressible flows, especially when shock waves occur. This is due to the fact that across a shock, mathematically there is a discontinuity in quantities such as pressure and velocity, and therefore, also in material properties such as density[48]. Simple refinement of the computational grid near shocks is often not working as

64

a remedy, as the shock location tends to be moving in space and time, and would require iterative refinements of the grid throughout the solution procedure, potentially even up to a local grid density that is several orders of magnitude denser than the original grid. In the case of two-phase flow this problem is even greater as, for a fluid in the two-phase region, a sudden change in pressure can cause changes in density of up to two orders of magnitude. A common solution, which was presented in [48], is to incorporate an artificial nonlinear viscosity that increases at discontinuities to relaxate the changes of quantities at shocks. Unfortunately, the software used in this work does not provide a way to incorporate such an artificial viscosity directly in the momentum equations. Therefore, a solution strategy was developed to avoid the divergence of the solution as soon as shocks establish. For this purpose, two computational grids, a coarse one and a fine one, were created to spatially discretize the ejector geometry. Both grids are two-dimensional, modeling the ejector as axisymmetric. Both grids are conformal, consisting of hexahedral cells only, with maximum skewness well below 0.5 and refinements at the walls. The cells are stretched in axial direction (increasing their aspect ratio) in regions such as the mixing chamber and the diffuser, as there exists a clear direction of convective transport and therefore, the number of needed cells can be significantly reduced. Inside the primary nozzle and where the primary and secondary exit meet, the aspect ratio is kept near unity. The coarse mesh consists of roughly 30 000 - 50 000 cells (depending on the geometry of the specific simulation). An example for a coarse grid is partly pictured in Figure 5.11a. The fine mesh is made up of roughly 150 000 - 200 000 cells (again, depending on the geometry used in a specific simulation). An example for a fine grid is partly pictured in Figure 5.11b.

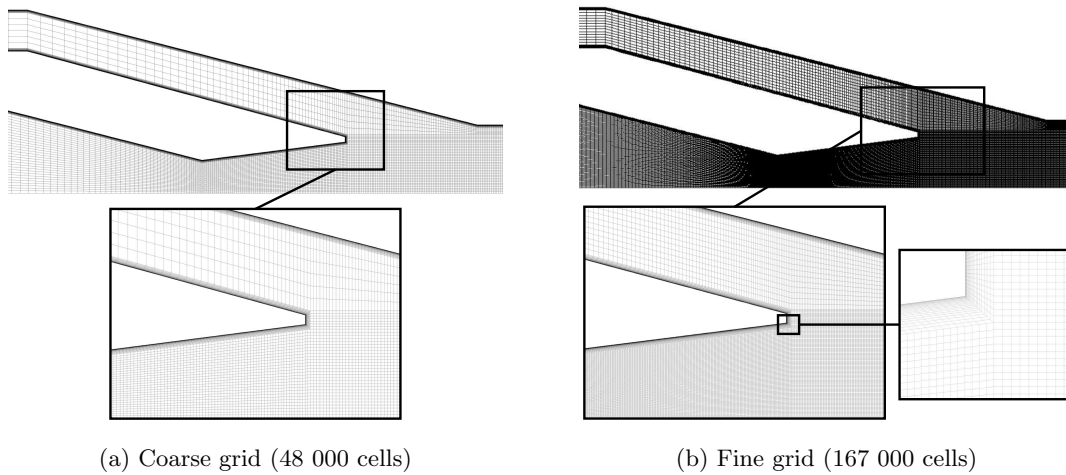(a) Coarse grid (48 000 cells) (b) Fine grid (167 000 cells)

Figure 5.11: Segment of a coarse and a fine computational grid for the ejector

The solution process consists of the following steps:

- Starting with the coarse mesh and with a closed secondary inlet the solution is initialized with the following values in the whole domain: Small, non-zero axial velocity; zero radial velocity; inlet enthalpy.

- The hybrid initialization method of FLUENT is used to obtain an initial guess for the pressure field. This method uses Laplace's equation to calculate the pressure distribution of an

incompressible, vorticity-free, laminar flow depending on the behaviour of the cross-sectional area throughout the domain[10].

- A converged solution for laminar and isenthalpic conditions is obtained. To achieve this, under-relaxation factors of all equations are kept below 0.2 and the density is temporarily frozen (by decreasing the corresponding explicit under-relaxation factor to an arbitrarily small value) when the first shock structures form in the pressure field.

- The energy equation is included in the calculation to obtain a converged, non-isenthalpic, laminar solution.

- The secondary inlet is opened and the calculation is again conducted until convergence is reached.

- The solution is interpolated onto the fine mesh to serve as an initial guess. The pressure and enthalpy solution, as well as the density are frozen and a solution for the velocity field is obtained. Then, pressure, enthalpy and density are, in that order, also included in the solution process until the laminar solution is converged on the fine mesh.

- The turbulence model is activated and to initialize the turbulent quantities, the solution of the laminar flow field is frozen while only turbulence equations are brought to convergence.

- All equations are further calculated to convergence.

- Depending on the specific simulation, it may be necessary to further refine the mesh at regions of high pressure- and velocity gradients to obtain a fully converged and grid-independent solution.

The need of the complex solution strategy outlined above, in which the user needs to take action depending on the behaviour of the solution at numerous times makes it difficult to automate the solution procedure in order to run e.g. a parameter study of geometric variations. Once a converged solution on the fine mesh is achieved, slight variations in operating conditions, such as a variation in the subcooling conditions at the primary inlet, can be performed in an automated manner without user intervention. However, once a different geometry is to be used for the calculations, the errors introduced when interpolating a previous solution onto a new mesh with a different geometry are too large to serve as initial guess and the whole solution strategy outline above needs to be re-run.

5.6   Results

5.6.1   Baseline Geometry

The baseline geometry and boundary conditions are taken from Schlemminger et al. [49], where experimental data for a supersonic, two-phase, CPM ejector operated with butane in a high temperature heat pump is available. The boundary conditions from [49], which are used for the simulation, are listed in Table 5.2. As can be seen, the refrigerant entering the ejector through the primary nozzle is subcooled. However, in [49] it was assumed that a vapor mass fraction of $\chi \approx 2.7\%$ was present at the primary inlet despite the temperature corresponding to a subcooled state. Therefore, a two-phase state corresponding to $\chi = 0.03$ was used as boundary condition for the value of enthalpy at the primary inlet. As temperature is not used as a variable in the solver because of the

66

energy equation being enthalpy-based, the temperature is merely a value that can be used for post-processing purposes but does not need to be specified in terms of boundary or initial conditions. Figure 5.12 shows the variation of static pressure along the ejector axis and wall plotted against

Primary inlet total pressure (bar)	21.39
Primary inlet subcooling ΔT (K)	3.59
Secondary inlet total pressure (bar)	4.30
Secondary inlet superheating ΔT (K)	8.06
Outlet static pressure (bar)	5.845

Table 5.2: Boundary conditions for butane ejector within high temperature heat pump [49]

experimental data from [49]. The pressure measurements were taken from drilled holes in the ejector wall, therefore measuring the static pressure at the wall. A deviation of the calculated pressure from experimental measurements is noticeable within the mixing zone where shock waves occur. Unfortunately, no information was available on the accuracy of the experimental measurements. Potential errors in measurements due to condensation at the drilled hole for the pressure measurement, as well as thermal effects can therefore not be quantified. The mass flow rate and entrainment ratio were, in the experiment, measured as $\dot{m}_{prim} = 0.127$ kg/s and $\eta = 0.46$, respectively[49]. The simulation over-predicts the mass flow rate by $\approx 30-45\%$ and the entrainment ratio by $\approx 20-50\%$, depending on the value of inlet vapor quality. (cf. Figure 5.13). The unsatisfactory prediction of mass flow rates by the HEM was also concluded by Bodys et al.[40] for subcritical inlet conditions (for CO_2 as working fluid). In the case of [40], the extension of the underlying model to incorporate non-equilibrium effects led to an agreement between experimental and simulated mass flow rates of less than 10%. As the inlet conditions of [49] are subcritical, the HEM of this work was therefore also extended by introducing a conservation equation for vapor quality, which features a so-called accommodation coefficient by which an arbitrary degree of relaxation of the equilibrium assumption can be incorporated. However, this coefficient depends on pressure and enthalpy and needs to be experimentally tuned not only to fit the properties of the working fluid, but also the underlying flow regime. In [40] the calibration of the accommodation coefficient was done by taking experimental measurements from a wide range of ejector geometries and operating conditions. Using a single experimental measurement to fine-tune this constant for butane under the operating conditions studied here would introduce a lot of uncertainty into the simulations, and as no experimental setup was available to reliably fit the accommodation constant, the non-equilibrium model was not used for simulations within this work. However, if a systematic set of experiments with a butane ejector should be available in the future, the underlying model could easily be modified to incorporate non-equilibrium effects.

In Figure 5.13, the influence of vapor quality at the primary inlet on the primary mass flow rate and the entrainment ratio is shown. As can be seen, error in mass flow rate prediction decreases for an increasing vapor quality. On the other hand, the error in entrainment ratio prediction increases proportionally. This suggests that the effect of a variation in primary inlet vapor quality mostly affects the primary inlet mass flow rate through the resulting change in density, but does not affect the physical process of entrainment to the same extent, leaving the absolute value of entrained secondary mass flow less affected. Therefore it seems plausible that the error in computed mass flow rates and entrainment ratios stems not only from a mismatch in experimental and computational inlet density but also from thermodynamic non-equilibrium effects not taken into account within

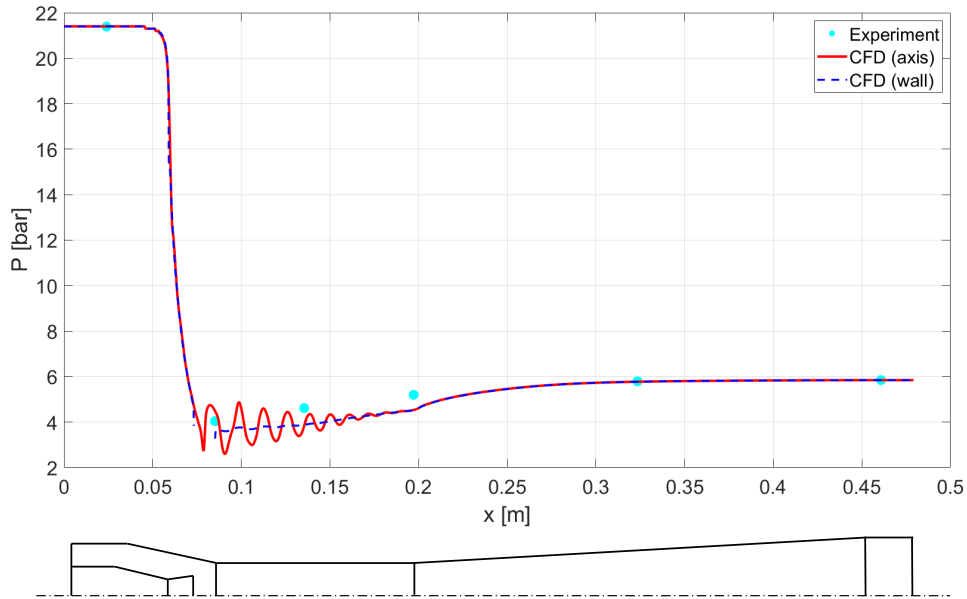the HEM approach, as suggested by Bodys et al.[40]. In Figure 5.14, the Mach number along the

Figure 5.12: Profiles of static pressure, p, along ejector axis and wall and experimental pressure measurements from [49]

ejector axis is plotted. Figure 5.15 shows the evolution of vapor quality, χ, along the ejector axis. In Figure 5.16 a contour plot of the Mach number is pictured, where typical diamond-shape shock patterns are formed within the supersonic jet leaving the primary nozzle. The flow reaches subsonic conditions at the end of the mixing zone, which is favourable as then no undesirable shocks form within the diffuser. In Figure 5.17 a contour plot of the vapor quality within the ejector is given. Immediately at the outlet of the primary nozzle, there is a sharp interface between the primary and secondary stream. Then, throughout the mixing zone, the two streams mix and the interface becomes more diffuse, with an almost homogeneous distribution of vapor quality entering the diffuser, as is desirable. In Figure 5.18 the distribution of static temperature throughout the ejector is depicted. Especially in the primary nozzle and beginning of the mixing chamber, the temperature gradients are relatively high. Information on the local distribution of temperature is important when it comes to ejector design. A possible way to reduce production costs drastically while allowing for more complex geometric designs could be to produce an inner layer of the needed high surface quality out of plastic, with an outer shell of low surface quality metal to provide the needed strength to withstand the pressure load. For such hypothetical designs involving plastic parts, knowledge of the temperature distribution within the ejector is essential. While high performance plastics that withstand the temperatures seen in Figure 5.18 are available, their detailed behaviour under the pressure load and local temperature gradients obtained from a CFD simulation could be analyzed by the means of finite element analysis.
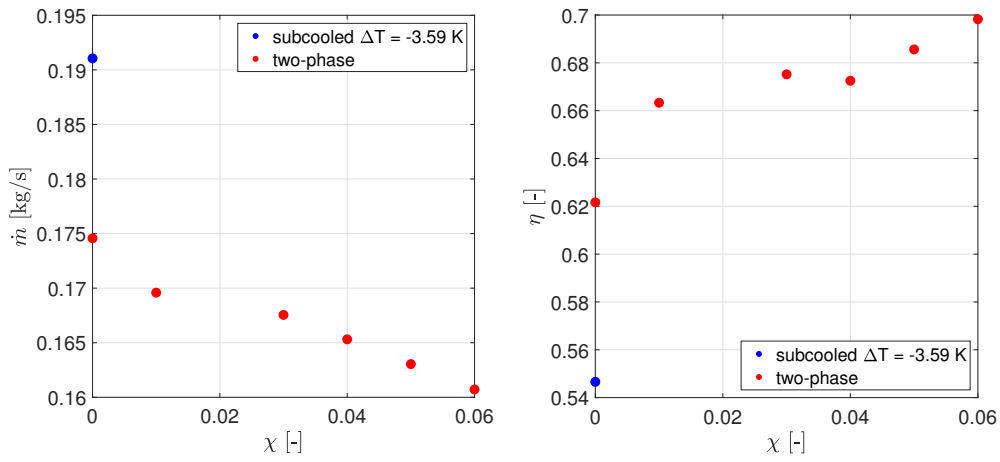
Figure 5.13: Primary inlet mass flow rate, $\dot{m}$, (left) and entrainment ratio, η, (right) for subcooled primary inlet condition and different levels of primary inlet vapor quality χ
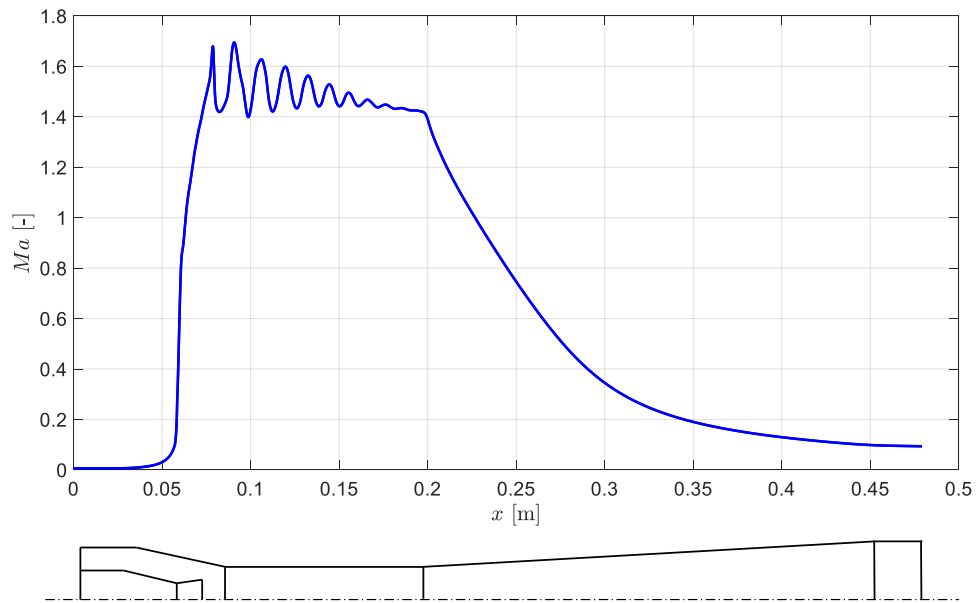

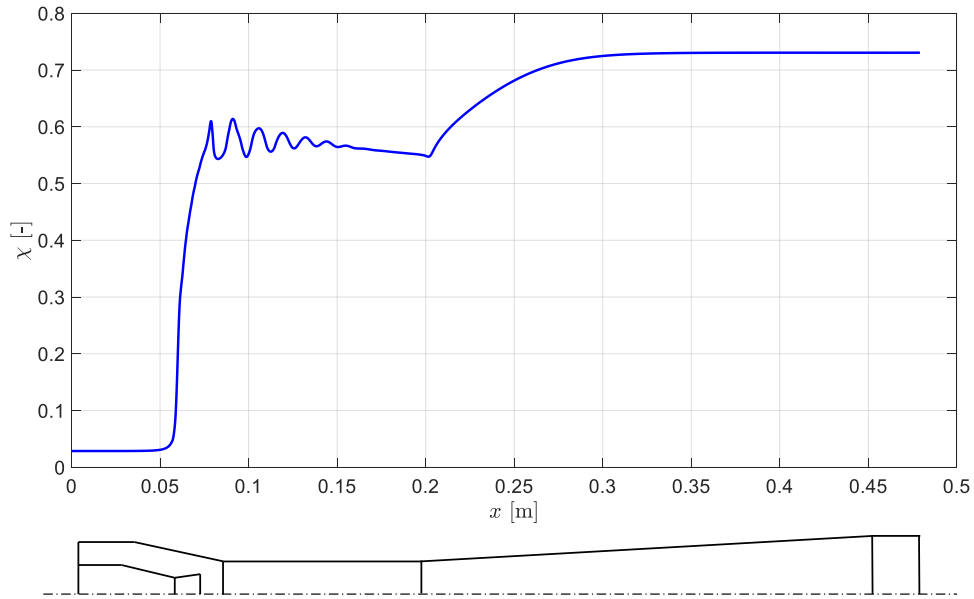Figure 5.14: Profile of Mach number along ejector axis

69

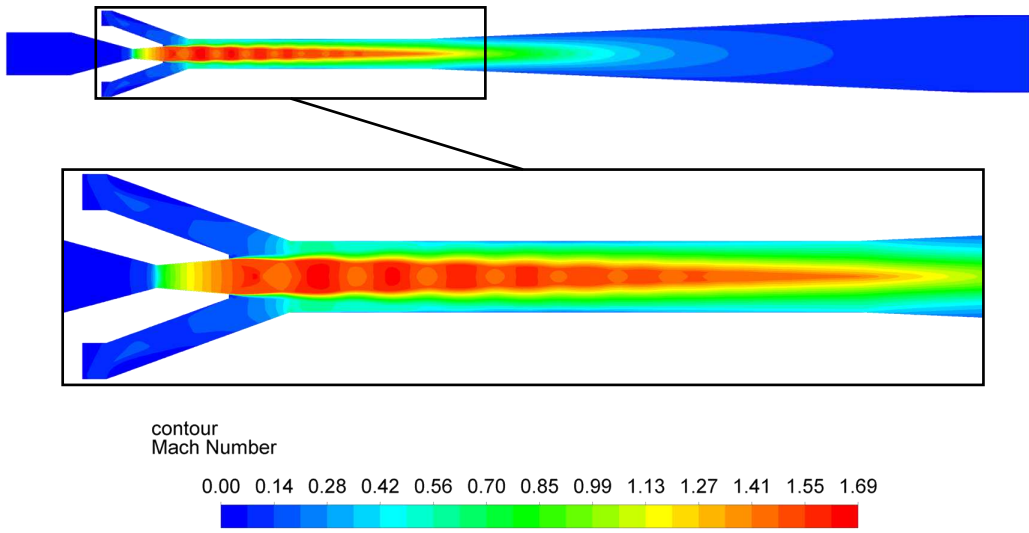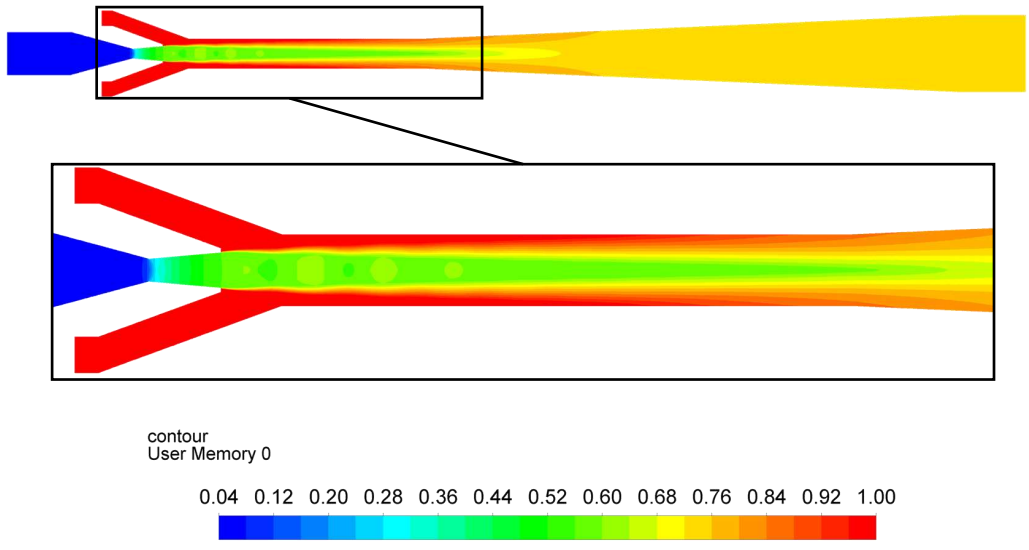Figure 5.15: Profile of vapor quality along ejector axis

contour
Mach Number

0.00 0.14 0.28 0.42 0.56 0.70 0.85 0.99 1.13 1.27 1.41 1.55 1.69

Figure 5.16: Contour plot of Mach number within ejector

contour
User Memory 0

0.04 0.12 0.20 0.28 0.36 0.44 0.52 0.60 0.68 0.76 0.84 0.92 1.00

Figure 5.17: Contour plot of vapor quality within ejector

contour
Static Temperature

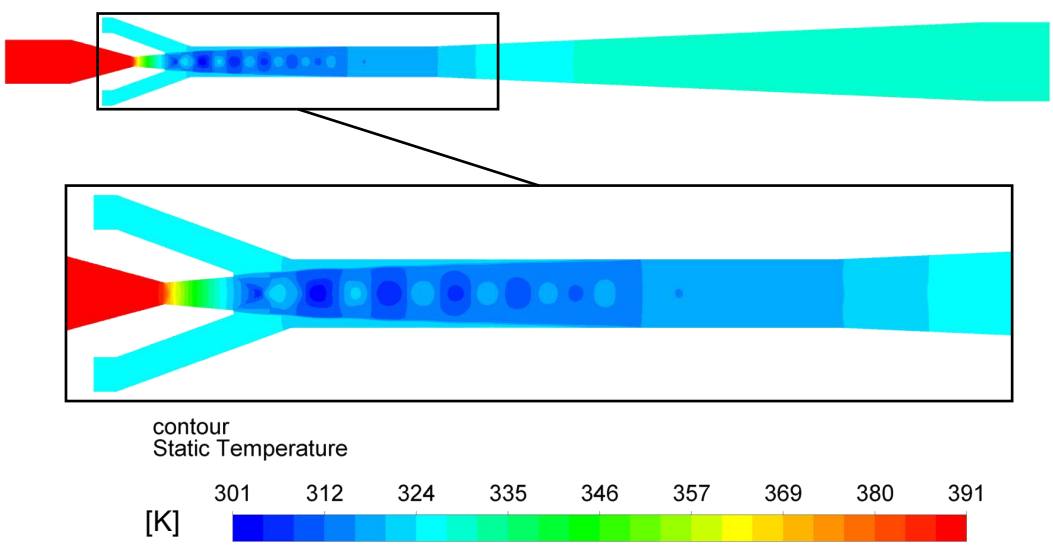301 312 324 335 346 357 369 380 391

[K]

Figure 5.18: Contour plot of static temperature within ejector

5.6.2 Influence of Geometrical Variation

An arbitrary variation in primary and secondary nozzle geometry, while keeping the mixing zone and diffuser geometry, as well as the boundary conditions identical to those specified in Table 5.2, is investigated here. In particular, the primary nozzle throat and exit diameter are increased while keeping the converging and diverging angle constant, and the secondary nozzle cross-sectional area is decreased. In Figure 5.19 a contour plot of the Mach number is shown. Opposed to the baseline geometry case discussed above, a higher maximum Mach number is reached and the flow stays supersonic until reaching the beginning of the diffuser, where a shock occurs. The consequence of this - for the given operating conditions poorly designed - ejector geometry is a boundary layer separation and recirculation region at the beginning of the diffuser, as can be seen in the Figure 5.20, where a plot of velocity vectors is shown. In the detail view, which is located at the beginning of the diffuser, a clear recirculation can be seen. To eliminate the possibility of this recirculation occurring due to an over-prediction of production of turbulent kinetic energy because of the large gradients of velocity by the turbulence model, the simulation was also re-run using the realizable k-ε, which also predicted a recirculation. More sophisticated turbulence models such as Reynolds Stress models, which do not use the Boussinesq assumption, could provide more reliable results concerning the boundary layer separation and recirculation. However, determining correct values for the boundary conditions of Reynolds stress components is not trivial and getting a converged solution using a Reynolds Stress model is significantly more difficult compared to eddy-viscosity models. Therefore, this was not further investigated. However, as long as two simulations use the same model, drawing a qualitative comparison is still valid. In Figure 5.21, the static pressure and Mach number along the ejector axis are plotted. As can be seen, there are two axial locations where shocks occur, and the flow reaches subsonic conditions only after the second shock which occurs within the beginning of the diffuser. While the inlet mass flow is, potentially mostly due to the increase in primary nozzle diameters, increased to $\dot{m}_{prim} = 0.44$ kg/s, the entrainment ratio not only decreases relatively to $\eta = 0.082$, but also in absolute values. This could stem from less drag in the shear layer between the primary and secondary flow, as the primary flow remains supersonic over a larger part of the ejector than in the baseline geometry. Therefore, mixing decreases and the two streams only mix within the diffuser, where the boundary layer separation occurs, and an increase in turbulence enhances mixing. This is also visible in the contour plot of vapor quality shown in Figure 5.22.

Even though the HEM used to perform the CFD simulations presented here is not capable of capturing important non-equilibrium processes within the ejector and therefore yields unsatisfactory global values for mass flow rates and entrainment ratio, nevertheless interesting qualitative conclusions on the suitability of an ejector geometry can be drawn. The HEM seems to be especially interesting for drawing relative comparisons between different ejector designs, when absolute performance parameters are not of interest. As shown here, the modified geometry analyzed above leads to unfavourable behaviour and poor performance compared to the baseline geometry.
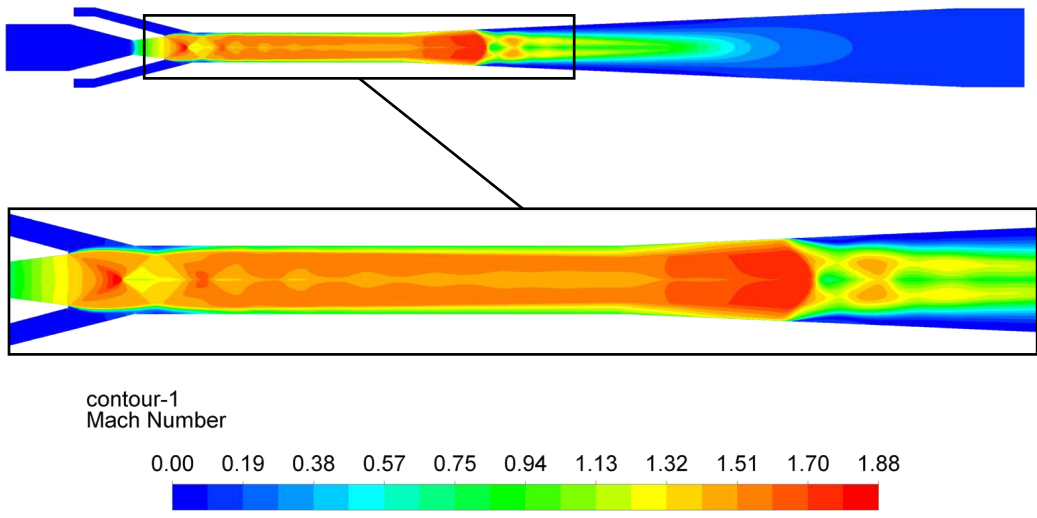
contour-1
Mach Number

0.00 0.19 0.38 0.57 0.75 0.94 1.13 1.32 1.51 1.70 1.88

Figure 5.19: Contour plot of Mach number within ejector; modified geometry

vector-1
Velocity Magnitude

[m/s]

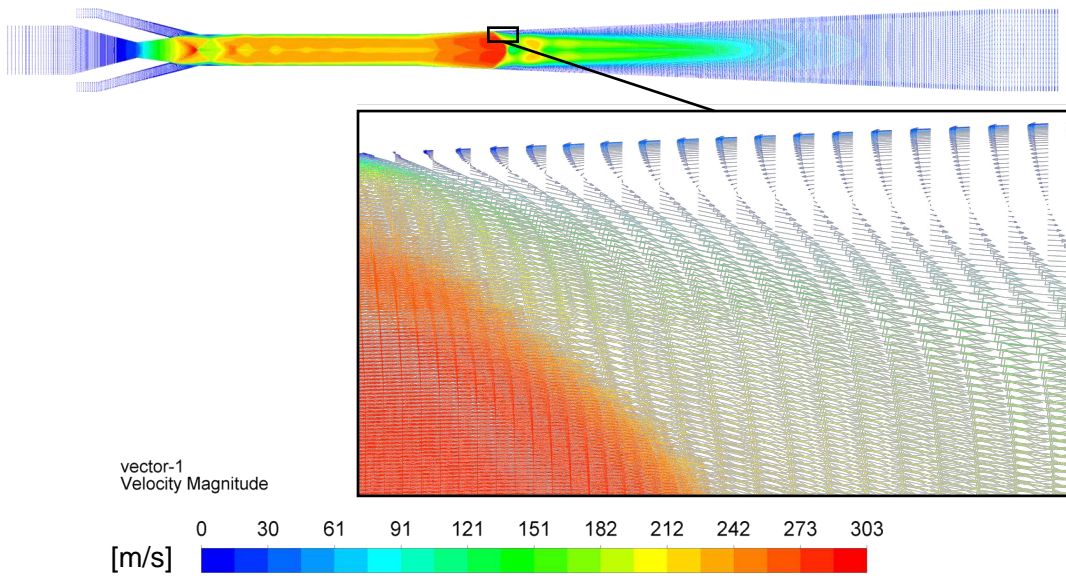0   30   61   91   121   151   182   212   242   273   303

Figure 5.20: Vectors of velocity within ejector, coloured by velocity magnitude; modified geometry
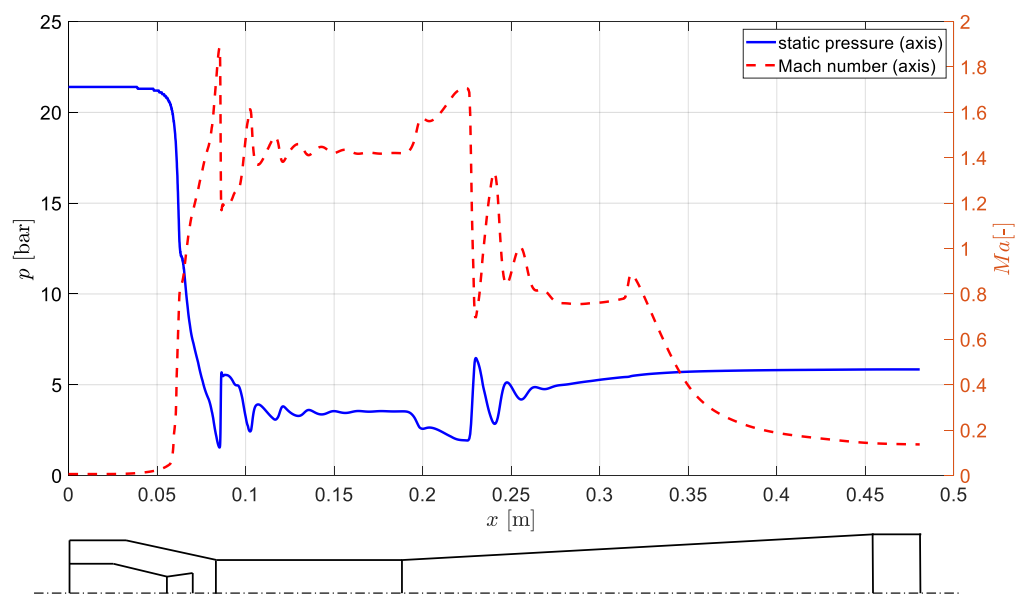
73

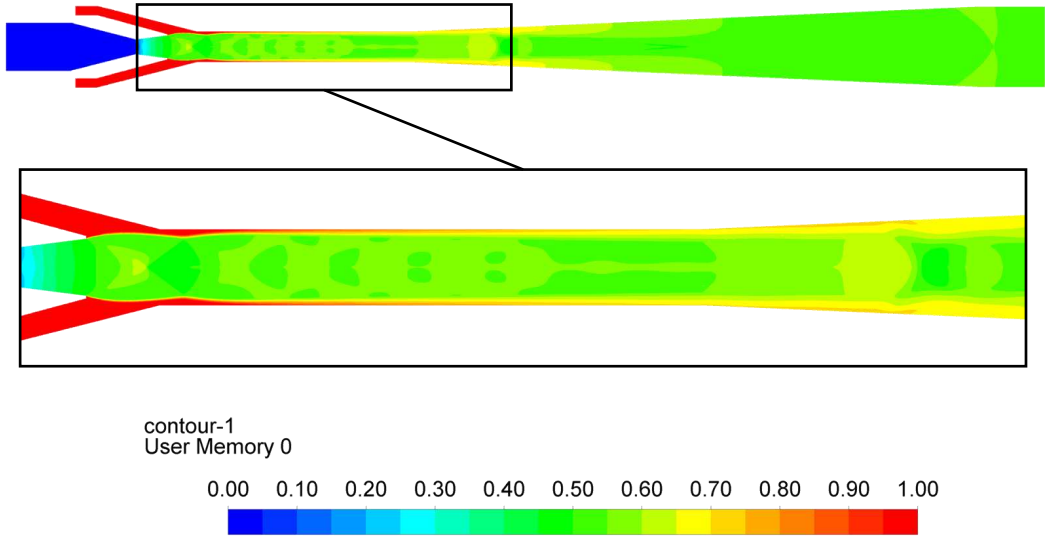Figure 5.21: Profiles of static pressure and Mach number along ejector axis; modified geometry

Figure 5.22: Contour plot of vapor quality within ejector; modified geometry

5.7 Conclusion

- Although ejectors are widely used in various applications, their use in heat pumps is yet a field of research. Therefore, most studies of two-phase supersonic ejectors concern refrigeration applications and mostly regard CO_2 ejectors.

- A homogeneous equilibrium model originally developed for modeling a transcritical CO_2 ejector was implemented in a commercial CFD code and used for simulations of a subcritical two-phase butane ejector.

- It is observed that for subcritical inlet conditions, as usually found in heat pumps, the assumption of a thermodynamic equilibrium leads to a deviation of predicted mass flow rates and entrainment ratios from experimental measurements.

- More physically accurate models, which include non-equilibrium phenomena, need careful fine-tuning to correctly model the underlying working fluid and flow regime. Therefore, without access to sufficient experimental data for model calibration, the advantage of such more sophisticated mathematical models is questionable.

- The HEM approach, where calibration is not necessary, can be used for a qualitative assessment and especially comparative study of e.g. ejector geometries.

- As global parameters predicted by the HEM deviate significantly from experiments, calculating potential COP improvements from the results of a standalone CFD study is at this stage not sufficiently reliable.

- The simulation approach presented within this work can be used to iteratively determine a suitable ejector geometry on the base of qualitative and relative performance criteria. Especially early in the development process, when many iterations are needed to determine a suitable geometry, the relatively higher computational speed of the HEM approach over non-equilibrium models and full multiphase models is useful. A geometry optimised in this way can then be used to manufacture a prototype which is needed for experimental analysis and the development of more complex computational models.

6 Conclusion and Outlook

Both the vortex tube and the ejector were numerically analysed with respect to their use as expansion device in high-temperature heat pumps with the aim of recovering a part of the expansion work.

The characteristics of a vortex tube were systematically analysed using different refrigerants and geometries under various operating conditions. The temperature separation achieved when operating a vortex tube with a refrigerant was found to be significantly lower than that obtained with air, which is a common working fluid for vortex tubes. Also, the fact that vortex tubes need to be operated with a gas in order to provide a temperature separation makes a significantly different heat pump cycle design necessary. Therefore, only a fraction of the available pressure difference between evaporator and condenser can be used for vortex tube expansion, and it is shown that an optimum of the thus needed intermediate pressure level (the inlet pressure of the vortex tube) needs to be determined based on the working fluid and the condenser and evaporator pressure levels. Therefore, the applicability of vortex tubes to heat pumps is very limited. Nevertheless, one application for industrial steam generation was found where the use of a vortex tube as expansion device significantly increased the COP over a conventional heat pump. A reasonable next step would be to automate the process of geometry- and grid-generation, CFD simulation setup, calculation and extraction of parameters to be used in a 1D cycle simulation, and in this way systematically test a great number of refrigerants, operating conditions and geometries to identify promising combinations for a potential experimental investigation.

For the ejector, a homogeneous equilibrium model was implemented in Ansys Fluent to allow for computationally affordable calculations without the need of experimental fine-tuning of more sophisticated models, which is difficult, given that currently heat pumps featuring an ejector are still a topic of research and not commercially available. Although the mathematical model is not capable of capturing metastability effects, and therefore mass flow rate predictions are unsatisfactory, the model can still be used to make interesting qualitative observations and for geometric shape optimization. Also, besides the limitations of the HEM approach, comparisons between different ejectors can be drawn. Concerning future work, a wider range of experimental data for ejectors operated under heat pump conditions is needed to calibrate more reliable numerical models. This is needed as the main quantities of interest for heat pump cycle simulations, the mass flow rates and entrainment ratio, are found to be strongly affected by non-equilibrium thermodynamics.

References

[1] United Nations Climate Change. *The Paris Agreement*. URL: https://unfccc.int/process-and-meetings/the-paris-agreement/the-paris-agreement. (accessed: 08.04.2020).

[2] European commission. *EU climate action*. URL: https://ec.europa.eu/clima/citizens/eu_en. (accessed: 26.08.2019).

[3] Statistik Austria. *Gesamtenergiebilanz Österreich 2017*. URL: http://statistik.gv.at/web_de/statistiken/energie_umwelt_innovation_mobilitaet/energie_und_umwelt/energie/energiebilanzen/022710.html. (accessed: 26.08.2019).

[4] S. Wolf et al. *Analyse des Potenzials von Industriewärmepumpen in Deutschland*. Forschungsbericht. Universität Stuttgart, 2014.

[5] M. Hartl et al. *Österreichische Technologie-Roadmap für Wärmepumpen, Berichte aus Energie- und Umweltforschung*. Tech. rep. bmvit, 2016.

[6] Statistik Austria. *Nutzenergieanalyse Österreich 2017*. URL: http://www.statistik.at/web_de/statistiken/energie_umwelt_innovation_mobilitaet/energie_und_umwelt/energie/nutzenergieanalyse/index.html. (accessed: 24.08.2019).

[7] B. Andersson et al. *Computational fluid dynamics for engineers*. Cambridge University Press, 2018.

[8] L. Davidson. *Fluid Mechanics, Turbulent Flow and Turbulence Modeling*. Chalmers University of Technology, 2015.

[9] L. Davidson. *An Introduction to Turbulence Models*. Chalmers University of Technology, 2015.

[10] Ansys Inc. *Fluent Theory Guide 19*. Canonsburg, USA, 2019.

[11] S. Sarkar and L. Balakrishnan. *Application of a Reynolds Stress Turbulence Model to the Compressible Shear Layer*. ICASE Report. NASA, 1990.

[12] T. B. Gatski and J.-P. Bonnet. *Compressibility, Turbulence and High Speed Flow*. Academic Press, 2013.

[13] H. Kuhlmann. *Strömungsmechanik: Eine kompakte Einführung für Physiker und Ingenieure*. Pearson Deutschland GmbH, 2014.

[14] P.A. Durbin. "On the k-3 stagnation point anomaly". In: *International Journal of Heat and Fluid Flow* 17.1 (1996), pp. 89–90.

[15] E. Sozer, C. Brehm, and C.C. Kiris. "Gradient Calculation Methods on Arbitrary Polyhedral Unstructured Meshes for Cell-Centered CFD Solvers". In: *52nd Aerospace Sciences Meeting*. 2014.

[16] C. Zenz, M. Lauermann, and M. Popovac. "Numerical analysis of the vortex tube characteristics used within a high temperature heat pump". In: *Proceedings of the 13th IEA Heat Pump Conference, Jeju Korea*. 2020. Accepted for publication.

[17] G.J. Ranque. "Experiences sur la Detente Girataire avec Productions Simultahees d'un Echappement d'Air chaud at d'Air froid". In: *Journal de Physique et le Radium* 4 (1933).

[18] R. Hilsch. "Die Expansion von Gasen im Zentrifugalfeld als Kälteprozess". In: *Zeitschrift für Naturforschung A* 1.4 (1946), pp. 208–214.

[19]   B.K. Ahlborn and J.M. Gordon. "The vortex tube as a classic thermodynamic refrigeration cycle". In: *Journal of Applied Physics* 88.6 (2000), pp. 3645–3653.

[20]   N.F. Aljuwayhel, G.F. Nellis, and S.A. Klein. "Parametric and internal study of the vortex tube using a CFD model". In: *International Journal of Refrigeration* 28.3 (2005), pp. 442–450.

[21]   A.J. Reynolds. "Energy flows in a vortex tube". In: *Zeitschrift für angewandte Mathematik und Physik ZAMP* 12.4 (1961), pp. 343–357.

[22]   R.T. Balmer. "Pressure-driven Ranque-Hilsch temperature separation in liquids". In: *Journal of fluids Engineering* 110.2 (1988), pp. 161–164.

[23]   R.L. Collins and R.B. Lovelace. "Experimental study of two-phase propane expanded through the Ranque-Hilsch tube". In: *Journal of Heat Transfer* 101.2 (1979), pp. 300–305.

[24]   W. Fröhlingsdorf and H. Unger. "Numerical investigations of the compressible flow and the energy separation in the Ranque–Hilsch vortex tube". In: *International Journal of Heat and Mass Transfer* 42.3 (1999), pp. 415–422.

[25]   H.M. Skye, G.F. Nellis, and S.A. Klein. "Comparison of CFD analysis to empirical data in a commercial vortex tube". In: *International Journal of Refrigeration* 29.1 (2006), pp. 71–80.

[26]   T. Dutta, K.P. Sinhamahapatra, and S.S. Bandyopdhyay. "Comparison of different turbulence models in predicting the temperature separation in a Ranque–Hilsch vortex tube". In: *International Journal of Refrigeration* 33.4 (2010), pp. 783–792.

[27]   A.R. Bramo and N. Pourmahmoud. "Computational Fluid Dynamics Simulation of Length to Diameter Ratio Effects on the Energy Separation in a Vortex Tube". In: *Thermal Science* 15.3 (2011).

[28]   U. Behera et al. "Numerical investigations on flow behaviour and energy separation in Ranque–Hilsch vortex tube". In: *International Journal of Heat and Mass Transfer* 51.25 (2008), pp. 6077–6089.

[29]   T. Maurer. *Patent DE19748083.7, Entspannungseinrichtung.* 1999.

[30]   J. Sarkar. "Use of vortex tube as expansion device in isobutane based refrigeration system". In: *Proceedings of ICRDME.* Tangori, Mohali (Punjab), India, Jan. 2008.

[31]   J. Zhu. "Experimental Investigation of Vortex Tube and Vortex Nozzle for Applications in Air-Conditioning, Refrigeration and Heat Pump Systems". MSc. Thesis. Graduate College of the University of Illinois at Urbana-Champaign, 2015.

[32]   M. Mohiuddin and S. Elbel. "A Fresh Look At Vortex Tubes Used As Expansion Device In Vapor Compression Systems". In: *Proceedings of the International Refrigeration and Air Conditioning Conference.* 2014.

[33]   G. Grazzini, A. Milazzo, and F. Mazzelli. *Ejectors for Efficient Refrigeration. Design, Applications and Computational Fluid Dynamics.* Springer, 2018.

[34]   G. Besagni, R. Mereu, and F. Inzoli. "Ejector refrigeration: A comprehensive review". In: *Renewable and Sustainable Energy Reviews* 53 (2016), pp. 373–407.

[35]   K. Chunnanond and S. Aphornratana. "Ejectors: applications in refrigeration technology". In: *Renewable and Sustainable Energy Reviews* 8 (2004), pp. 129–155.

[36] S. Elbel and N. Lawrence. "Review of recent developments in advanced ejector technology". In: *International Journal of Refrigeration* 62 (2016), pp. 1–18.

[37] S. Varga, A.C. Oliveira, and B. Diaconu. "Influence of geometrical factors on steam ejector performance – A numerical assessment". In: *International Journal of Refrigeration* 32 (2009), pp. 1694–1701.

[38] K. Banasiak and A. Hafner. "1D Computational model of a two-phase R744 ejector for expansion work recovery". In: *International Journal of Thermal Sciences* 50 (2011), pp. 2235–2247.

[39] J. Smolka et al. "A computational model of a transcritical R744 ejector based on a homogeneous real fluid approach". In: *Applied Mathematical Modelling* 37 (2013), pp. 1208–1224.

[40] J. Bodys et al. "Non-equilibrium approach for the simulation of CO2 expansion in two-phase ejector driven by subcritical motive pressure". In: *International Journal of Refrigeration* 114 (2020), pp. 32–46.

[41] M. Yazdani, A.A. Alahyari, and T.D. Radcliff. "Numerical modeling of two-phase supersonic ejectors for work-recovery applications". In: *International Journal of Heat and Mass Transfer* 55 (2012), pp. 5744–5753.

[42] G. Biferi et al. "CFD modelling of the condensation inside a supersonic ejector working with R134a". In: *Energy Procedia* 101 (2016), pp. 1232–1239.

[43] C. E. Brennen. *Fundamentals of Multiphase Flow*. Cambridge University Press, 2005.

[44] I.H. Bell et al. "Pure and Pseudo-pure Fluid Thermophysical Property Evaluation and the Open-Source Thermophysical Property Library CoolProp". In: *Industrial & Engineering Chemistry Research* 53.6 (2014), pp. 2498–2508.

[45] F. Giacomelli et al. "CFD modeling of the supersonic condensation inside a steam ejector". In: *Energy Procedia* 101 (2016), pp. 1224–1231.

[46] H. Oertl jr., ed. *Prandtl - Führer durch die Strömungslehre*. Springer Vieweg, 2017.

[47] Z. Vlahostergios and K. Yakinthos. *ERCOFTAC: Converging-diverging transonic diffuser*. URL: https://kbwiki.ercoftac.org/w/index.php?title=Abstr:UFR_4-19. (accessed: 24.01.2020).

[48] J. Von Neumann and R.D. Richtmyer. "A Method for the Numerical Calculation of Hydrodynamic Shocks". In: *Journal of Applied Physics* 21 (1950), pp. 232–237.

[49] C. Schlemminger et al. "Hochtemperatur Wärmepumpe mit Ejektor". In: *Deutsche Kälte- und Klimatagung 2019, Ulm*. DKV - Deutscher Kälte- und Klimatechnischer Verein, 2020.